Towards The Matter Compiler

Looking Ahead to Computer-Controlled Molecular Assembly

Submitted by

Calvin Ray Davidson

to the University of Sussex as a thesis for the degree of
Doctor of Philosophy in Chemistry in the School of Life Sciences

September 2011

Acknowledgements

I would like to acknowledge all the help and guidance that I have received over the years spent researching this project. I am particularly grateful to both the Engineering and Physical Sciences Research Council, without whose funding none of this would have been possible, and to EDF Energy Nuclear Generation for additional support. The Chemistry and Biochemistry department at Sussex, and indeed Sussex University as an institution should also be singled out for praise.

My thanks also go out to all members, past, present and future, of the Theoretical Chemistry and Computational Materials group, especially Gemma and Irene for early guidance, and Jens, James, Glen and Jean-Jo for general camaraderie.

I'd also like to thank the extended family that is the *AIMpro* community. The individuals that deserve credit are too numerous to name specifically but there are some who stand head and shoulders above the rest, namely:

Bob Jones, Patrick Briddon and Mark Rayson for creating, developing and refining the remarkably efficient *AIMpro* density functional theory code, continually advancing the state of the art well ahead of the pack.

Jon Goss for his ability to spot and correct problems in complex *AIMpro* dat files, and particularly for his propensity to do so via email on very short notice.

Jerry Hagon, the unsung hero behind *AIMview* and the *AIMproDX* libraries that support it. Without the ability to visualise the output from *AIMpro*, much of this project would be meaningless.

Christopher Latham for his knowledge of the peculiarities of open source software, such as the Linux operating system and the L$^{A}T_{E}$X typesetting language.

Chris Ewels, Greg van Lier and Nicole Grobert, and all the delegates who attend the annual NanoteC conference. The enthusiasm I see there has served as an inspiration to me throughout my research.

And finally, my heartfelt thanks go to my long-suffering supervisor, Prof. Malcolm Heggie: polymath, bon vivant and song-mangler extraordinaire! His infectious, boundless enthusiasm for his subject and his willingness to engage with the whole group on a more personal level has been nothing short of magnificent.

Abstract

This thesis addresses the concept of atomically precise manufacturing and aims to examine some likely aspects of the necessary infrastructure and knowledge that will be required from a theoretical standpoint.

By way of introduction, I trace the history of Science Fiction's influence on scientific research and examine some examples that have specifically inspired the thinking behind nanoscience and nanotechnology. More serious speculation, both in favour of and arguing against the possibility of bottom-up manufacturing is also discussed. I look at two schools of thought; directed assembly, typified by the ambition to assemble molecular structures piece by piece and self assembly, where networks of molecules form into arrays on substrates, imparting novel properties.

Various methodologies and tools available to the nanotechnologist are examined. Density functional theory, as employed in the *AIMpro* code, and Molecular Mechanics are discussed, particularly in respect of their strengths and weaknesses for use in simulating the kind of nanoscale processes appropriate to nanomanufacturing. The theoretical basis behind scanning tunneling microscopes is also examined, with particular attention paid to their potential for upscaling in the future.

Some components found within scanning tunneling microscopes are simulated using Density Functional Theory. Models of pure tungsten tips are studied at various levels of complexity in order to decide upon a reasonable compromise between accuracy and ease of computation. The nature of the interlayer interaction in few layer graphenes is examined and pristine and defected graphitic surfaces, are studied with a view towards their use as nano-workbenches. Their images as produced in scanning tunneling microscopes are simulated. Density Functional Theory is applied to organic molecules self-assembling on metallic substrates. Specifically, tetracene on a clean copper surface and on an oxygen-terminated copper surface is studied.

Finally, I discuss the significance of the results of each section, taken individually and as a whole, and try to put it into perspective regarding the practicality of actually employing this paradigm realistically in the near future.

Contents

Abbreviations

Abbreviation	Meaning
AFM	atomic force microscope
DFT	density functional theory
GGA	generalised gradient approximation
HOMO	highest occupied molecular orbital
ICISS	impact collision ion scattering spectroscopy
LDA	local density approximation
LEED	low energy electron diffraction
LUMO	lowest unoccupied molecular orbital
MM	molecular mechanics
MO	molecular orbital
MP	Monkhorst-Pack
SF	science fiction
SOMO	singly occupied molecular orbital
SPM	scanning probe microscope
STM	scanning tunneling microscope
XRD	X-ray diffraction

Chapter 1

The Matter Compiler as a Concept

As an introduction to this thesis, I'd like to begin with a thought experiment. Let's build a time machine and travel back some fifty years into the past. If we approach a photographer of the day and inform them that, fifty years into their future, they will be able to run the equivalent of an entire photographic studio, and more besides, using equipment occupying about as much space as a typewriter, they'll likely be utterly amazed. And yet, returning to the present day, with nothing more than a digital camera, a notebook computer loaded with the relevant software and a reasonable quality inkjet printer, this kind of capability is taken for granted and is available at a very reasonable price in the high street. Now let's step back into our time machine to move forwards fifty years and take a look at what's sitting on a desk in the future.

The equivalent of the notebook there is likely to be significantly more powerful, equipped with improved input and output devices and a far cry from anything we'd recognise as a desktop computer, but that's not what I'd like us to consider. It's the replacement for the printer that I'd like to take a speculative look at. What we might see is a device capable of producing anything that the computer operator can design, including seamless, three dimensional objects composed of different materials as required and assembling them from feedstock chemicals one atom or functional group at a time. If you think that that sounds more like something out of a science fiction tale than a suitable subject for serious scientific research, you may have a point but let's have a look at the relationship between science and science fiction (SF).

1.1 Journeys from Fiction to Science

Many people regard SF to be little more than modern day fairy stories but is this analysis fair? Were the genre to be comprised solely of the blockbuster, rocketship and raygun movies and television series that have become so popular in recent decades, that conclusion might seem appropriate. SF is much more than that, though. Indeed, many would argue, with quite reasonable justification, that the type of space-based action stories epitomised by the likes of the "Star Wars" series are not really SF at all, but merely fantasy stories set in a ultra-modern setting. No, SF is a literary genre and, as its name implies, requires a healthy dose of genuine science mixed with its fictional content in order to exist.

Once this is understood, it should come as no surprise that many scientists claim to have been inspired to study science by the SF that they read as young adults and it should also come as no surprise that many SF authors come to the genre with a healthy background in science, technology or engineering. Over sixty years ago, the post-war scene was dominated by the writers who became known as the "Big Three" of SF: Robert Heinlein, Isaac Asimov and Arthur C Clarke.

Robert Heinlein had worked on wireless communication technology for the US Navy in the 1930s, a field undergoing rapid development at the time, and had moved into aeronautical engineering during World War 2. Upon being invalided out of the Navy and undergoing an extensive period of hospitalisation, he developed the waterbed, describing it in such detail that his writings were sufficient for the US Patent Office to deny a patent application nearly twenty years later on the grounds of prior art [1]. His SF was always well grounded in the science of the day and his contribution to technology is evident in the name given to remote manipulators, "Waldoes", named after the eponymous protagonist of one of his many stories [2].

Isaac Asimov was a prodigious writer, best known for the likes of the Foundation Trilogy and his robot stories, collected in "I, Robot" and "The Rest of the Robots" [3][4]. What is not so generally known is that that he had received a PhD in Biochemistry in 1948 and that he was equally prodigious in many other fields of writing. As well as writing extensively on everything from History to Shakespeare to the Bible, he co-authored a biochemistry textbook and wrote several popular science books for the layman, explaining the intricacies of everything from electro-magnetism to evolution in a clear, concise and engaging manner [5][6][7]. The science in his fiction writing was always as rigorous as you would expect from someone with such a background.

Arthur C Clarke earned a degree in Mathematics and Physics in the immediate post-war years after rising rapidly through the ranks of the Royal Air Force while developing radar systems during the second world war. He is an example of a writer who was not only able to integrate science seamlessly into his stories, but also able to research and articulate his speculation in a more formal manner. Early on, in letters and articles published in Wireless World in 1945, he predicted multi-stage launch vehicles and a global communication network based based on geo-stationary satellites [8][9]. Later in his career, in his 1979 novel "The Fountains of Paradise" he postulated an orbital tower as a replacement for launch vehicles, even going so far as to predict the necessity of a form of "mono-dimensional carbon" for its construction [10]. As "The Space Elevator", this is an idea that has since gained significant traction within the scientific community, especially since the discovery of novel carbon nanomaterials and their phenomenal potential would seem to make this a theoretical, if somewhat ambitious, possibility.

So it would seem that there is an established history of influence flowing both ways between science and SF. As well as science providing background information vital to the development of SF narratives, in return, SF feeds back into the scientific community, inspiring many young people to take up a career in science and sometimes providing potential directions for their research to take. With this in mind, it is probably worthwhile taking a look at some of the fiction dealing with a nanotechnological based future.

The possibility of working at the sub-micrometer level has long been a recurring and tantalising theme in SF. As noted above, there was Robert Heinlein's 1942 "Waldo" with its micro-manipulators; in 1954, Philip K Dick was examining the ideas of self-replication in "Autofac" and, in 1956 Arthur C Clarke wrote the short story "The Next Tenants" describing tiny machines operating, if not at the nano-scale, at least at the micro-scale [11][12]. A nanomanufacturing procedure was described by Robert Silverberg in 1969 as an aside in his 1969 novella "How It Was When the Past Went Away" whereby an audio system was constructed comprising "thousands of loudspeakers per inch" [13].

As science has advanced since that time, so has SF. Even the name given to the project that seeded this DPhil thesis, "The Matter Compiler" can be traced back, either by coincidence or design, to a pivotal piece of fictional technology described in Neal Stephenson's seminal, 1994 nanotechnology-based work, "The Diamond Age" [14]. In it, he described a world suffused with nanotechnology from the bespoke systems commissioned by the rich ruling classes right down to the "feeds" being piped into every building, much as gas and electricity are today. A Matter Compiler sits in every home, ubiquitously connected to these feeds and providing the masses with many of their basic commodities.

Given the way that interest within the SF community so often stimulates scientific interest, and vice versa, it was inevitable that the subject would soon receive more serious treatment.

1.2 A Brief History of Nanoscience

Although mankind as far back as the ancient Greeks may have had the concept of an indivisible unit of matter (the word "atom" having been derived from the Greek word "atomos", meaning "uncuttable"), Michael Faraday should probably be credited with the origination of the scientific concepts that would evolve into what we now know as nanotechnology. It was he who first who revealed that matter at the micrometer scale displays markedly different properties to those of the bulk [15]. A decade later, James Clerk Maxwell, in his kinetic theory of gases, formulated the concept of "finite being" wherein large quantities of tiny particles moving at high velocities are able to exert pressure due to their cumulative potential energy [16]. With the advent of colloid science, Wolfgang Ostwald put forward the idea of 'neglected dimensions" and a gradual transition between molecular and colloidal states [17]. Faraday's work that launched the application of colloidal gold in fields such as optics, catalysis and biology, revisited and extended over a century later by John M Thomas, estimated that gold "sols" contain particles of 3-30 nm in diameter [18]. These particles would certainly be recognised today as "nano-particles".

The first observations and size measurements of nano-particles are generally ascribed to Richard Zsigmondy who conducted detailed studies of gold sols and other materials with sizes down to 10 nm and less [19]. The colloidal metal suspensions and their small metal particles later attracted great interest because of their behaviour in solution, falling somewhere between pure solutions and emulsions. There have been many studies of periodic colloidal structures and the principles of molecular self-assembly. The study of these materials, from clusters of a few metal atoms up to metal colloids with thousands of atoms has grown into an independent interdisciplinary scientific area in its own right. By the middle of the twentieth century, new concepts from a sporadic accumulation of knowledge were beginning to lead towards nano-science as a separate discipline and the explorations were becoming more systematic.

The potential for technology at extremely miniature scale to revolutionise manufacturing was probably first envisaged by Richard Feynmann in his speech, "There's Plenty of Room at the Bottom" [20]. In one section of his talk, Feynmann discussed the possibility of a set of mechanical hands, similar in principle to those used for handling hazardous items remotely, but at a quarter scale. By using these "slave" hands to build miniature copies of themselves iteratively, he saw a way of working at the sub-microscopic level and thus, although his vision was rather crude by today's standards, he had effectively anticipated much of today's nano-scale ambition. The term "nanotechnology" was first coined by Taniguchi in 1974 to imply the understanding and manipulation of materials at scales of up to 100 nm [21]. As the century drew to a close, the technological significance of nano-scale phenomena became increasingly appreciated and nascent ideas for molecular manufacturing were being enthusiastically developed [22][23][24].

1.3 A Vision of Nanoengineering

K Eric Drexler's 1986 book, "Engines of Creation" deserves to be singled out here for its breathtaking vision but some qualification is required [25]. In it he examined the trend for miniaturisation that had been widespread in science and technology since the fifties and discussed the inevitability of its extrapolation to the nanoscale. Although he comprehensively addressed the potential for huge changes across many scientific disciplines and areas of society, the book was roundly criticised in some quarters for what was seen as its lack of technical details. Drexler addressed some of this criticism in 1992 with "Nanosystems: Molecular Machinery, Manufacturing, and Computation" but, although he showcased the ability to design components at the nanoscale, he offered very little advice regarding any real-world route towards practical application of his ideas [26]. As a result, many traditional chemists, most publicly the late

Richard Smalley, have remained extremely sceptical of the practicability of atomically precise assembly within the real world [27]. This highlights one of the main objections to nanomanufacturing, in that the complexity of upscaling what can be achieved on a molecule-by-molecule basis to a level that becomes usable in the real world is so enormous as to be practically unachievable.

However, Drexler's nanomanufacturing ambition is not the only scenario where bottom-up assembly is attractive. The high-tech areas of modern industry have a voracious appetite for the exotic new compounds that are constantly being identified and synthesised by modern science. The properties of these new materials are dictated by many factors including their molecular structures; the number of atoms and the type, order and topology of bonds. Many of these properties can be calculated with ever increasing accuracy by theoretical chemists and extrapolated to predict the properties of compounds and materials that are beyond our current capabilities to produce. Liquid and gas phase methods of production have historically served mankind well but they have their limitations when attempting to synthesise some of these theorised materials. In recent years, however, researchers have been steadily working at ever smaller scales and with ever greater precision towards completely innovative approaches.

At the time of writing, the range of actual structures being used in experiments designed to lead towards nano-manufacturing is very limited but the knowledge base is building. The ability to fabricate a complex user-defined product at the molecular level in a single operation is fairly obviously unrealistic but the same effect may be achievable as a succession of relatively simple steps that are in total accordance with physical laws. These steps may be based on different approaches, with promising work being undertaken researching the self-assembly of atoms and molecules on metallic surfaces and atomically-precise "machine phase" chemistry, where the reactants are physically introduced to each other using a scanning probe microscope

(SPM).

This approach to matter compilation offers intriguing possibilities. An SPM tool-tip, specifically designed to hold a reactant moiety in a particular orientation, together with a work-piece surface holding a second reactant may allow reactions involving transition states that would be impossible to achieve by any traditional approach to synthesis. Any plan to develop such a method of matter compilation for arbitrary user-defined structures will require a comprehensive understanding of many problems and challenges, some of which may only be revealed in the light of future research in this field. Although there are considerable obstacles to overcome, it shows the potential to produce a wide range of nanomaterials. The criteria for positional assembly differ in many respects when compared to self-organisation and the foundations of this mechanical synthesis are rooted in theoretical analysis and calculations.

The manipulation of matter at this scale is based on the general principles of this so-called "mechanical chemistry". By using mechanical energy in order to push, pull, abstract and replace atoms and other moeties, it is envisaged that nanostructures with custom-designed properties (metallic, dielectric, organic, etc.) may be built on different surfaces. A lot of progress in this area has occurred simultaneously with improvements in scanning probe microscopy. Since the general ideas of mechanically displacing and positioning atoms, functional groups and molecules with atomic precision using tiny robotic arms have been put forward, this approach has been successfully developed using the STM [22][23][28][29]. Lateral and vertical manipulations have been achieved under different conditions [30][31][32]. Various techniques for atomically precise positioning have been explored for specific applications, including Si (100) and (001) surfaces [33][34][35]. Other examples of manipulation at this scale include the deposition and removal of single Si atoms from a Si (111)-(7x7) surface, as well as the arrangement of CO molecules on Cu (211) to form the letters F and U, representing the logo of the Freie University [36][37].

That concludes the introduction and overview of the current state of the art. The next chapter will examine the theory that underpins this thesis.

1.4 References

[1] Taylor Dinerman. Robert A Heilein's Legacy. *The Wall Street Journal*, (26th July), 2007.

[2] Robert A Heinlein. Waldo. *Astounding Science Fiction*, 1942.

[3] Isaac Asimov. I, Robot. *Gnome Press*, 1950.

[4] Isaac Asimov. The Rest of the Robots. *Doubleday*, 1964.

[5] Isaac Asimov. Asimov's Guide to Shakespeare, vols 1 and 2. *Gramercy Books*, 1970.

[6] Isaac Asimov. Asimov's Guide to the Bible: The Old and New Testaments. *Wings Books*, 1981.

[7] Isaac Asimov and John Bradford. The Chemicals of Life. *Signet*, 1954.

[8] Arthur C Clarke. Peacetime Uses for V2. *Wireless World*, (February):58, 1945.

[9] Arthur C Clarke. Extra-Terrestrial Relays Can Rocket Stations Give World-wide Radio Coverage? *Wireless World*, (October):305–308, 1945.

[10] Arthur C Clarke. The Fountains of Paradise. *Victor Gollancz*, 1979.

[11] Philip K Dick. Autofac. *Galaxy*, 1955.

[12] Arthur C Clarke. The Next Tenants. *Renown Publishing*, 1956.

[13] Robert Silverberg. How It Was When the Past Went Away. *Meredith*, 1969.

[14] Neal Stephenson. The Diamond Age. *Bantam*, 1995.

[15] Michael Faraday. The Bakerian Lecture: Experimental Relations of Gold (and other Metals) to Light. *Philos Trans R Soc London*, 147:145–181, 1857.

[16] J C Maxwell. On the Dynamical Theory of Gases. *Philos Trans R Soc London*, 157:49–88, 1867.

[17] Wolfgang Ostwald. An Introduction to Theorical and Applied Colloid Chemistry: The World of Neglected Dimensions. *Chapman and Hall, Ltd. London*, 1917.

[18] John M Thomas. Colloidal metals: past, present and future. *Pure and Appl Chem*, 60(10):1517–1528, 1988.

[19] Richard Zsigmondy and Jerome Alexander. Colloids and the Ultramicroscope: A Manual of Colloid Chemistry and Ultramicroscopy. *Wiley*, 1909.

[20] Richard Feynman. There's Plenty of Room at the Bottom. *Engineering and Science*, XXIII(5), 1960.

[21] T Taniguchi and S Gakkai. Proceedings of the International Conference on Production Engineering, Tokyo. 1974.

[22] H Farrell and M Levinson. Scanning tunneling microscope as a structure-modifying tool. *Physical Review B*, 31(6):3593–3598, 1985.

[23] K Eric Drexler and J Foster. Synthetic tips. *Nature*, 343:600, 1990.

[24] Don Eigler and E Schweizer. Positioning single atoms with a scanning tunnelling microscope. *Nature*, 344:524–526, 1990.

[25] K Eric Drexler. Engines of Creation. *Anchor Books, New York*, 1987.

[26] K Eric Drexler. Nanosystems: Molecular Machinery, Manufacturing and Computation. *Wiley*, 1992.

[27] Rudy Baum. Nanotechnology: Drexler and Smalley make the case for and against 'molecular assemblers'. *Chemical and Engineering News*, 81(48):37–42, 2003.

[28] C Musgrave, J Perry, Ralph C Merkle, and W Goddard. Theoretical studies of a hydrogen abstraction tool for nanotechnology. *Nanotechnology*, 2:187–195, 1991.

[29] Ralph C Merkle and Robert A Freitas Jr. Theoretical analysis of a carbon-carbon dimer placement tool for diamond mechanosynthesis. *J Nanosci Nanotechnol*, 3(3):319–324, 2003.

[30] I Lyo and Phaedon Avouris. Field-Induced Nanometer-to Atomic-Scale Manipulation of Silicon Surfaces with the STM. *Science*, 253:173–176, 1991.

[31] J Stroscio and Don Eigler. Atomic and Molecular Manipulation with the Scanning Tunneling Microscope. *Science*, 254:1319–1326, 1991.

[32] Masakazu Aono, Ataru Kobayashi, Francois Grey, Hironaga Uchida, and De-Huan Huang. Tip-Sample Interactions in the Scanning Tunneling Microscope for Atomic-Scale Structure Fabrication. *Japanese Journal of Applied Physics*, 32(Part 1, No. 3B):1470–1477, 1993.

[33] C Salling and M Lagally. Fabrication of Atomic-Scale Structures on Si (001) Surfaces. *Science*, 265:502–506, 1994.

[34] Phaedon Avouris. Manipulation of Matter at the Atomic and Molecular Levels. *Accounts of Chemical Research*, 28(3):95–102, 1995.

[35] MC Hersam, G C Abeln, and J W Lyding. An approach for efficiently locating and electrically contacting nanostructures fabricated via UHV-STM lithography on Si(100). *Microelectronic Engineering*, 47(1-4):235–237, 1999.

[36] De-Huan Huang and Hironaga Uchida. Deposition and subsequent removal of single Si atoms on the Si(111)-7 x 7 surface by a scanning tunneling microscope. *Journal of Vacuum Science and Technology B*, 12(4):2429–2433, 1994.

[37] G Meyer, B Neu, and K Rieder. Controlled lateral manipulation of single molecules with the scanning tunneling microscope. *Applied Physics A: Materials Science & Processing*, A60:343–345, 1995.

Chapter 2

Discussion of Theory

2.1 Scanning Probe Microscopy

The advances that have been achieved in all aspects of nanotechnology would be inconceivable without commensurate advances in microscopy, particularly with regard to scanning probe technology. This has proved to be vitally important for the development of both self-organised assembly and mechanical synthesis. Today's ability to study, design and realise structures with different ionic and covalent bonds is due, in a large part, to the high resolutions available to researchers using advanced SPMs

2.1.1 Scanning Tunneling Microscopy

The scanning tunneling microscope (STM) was the first tool of this type that was developed. It was invented by Gerd Binnig and Heinrich Rohrer at IBM in 1981 [1]. In 1986, together with Ernst Ruska for his pioneering work on electron microscopy, they shared the Nobel Prize for Physics.

The STM's principle of operation is illustrated in Figure 2.1. It relies on quantum mechanical tunneling effects between an atomically sharp tip and the surface being studied. This tunneling effect requires the tip and surface to be made from conductive materials. When the tip is brought very close, say 1 nm, to the sample surface and a small negative bias of around 1 V is applied, classical physics suggests that the electrons ought not to be able to jump the vacuum between tip and substrate. However, quantum mechanical effects mean that wavefunctions can overlap and that electrons in the tip each have a quantifiable probability of tunneling through to the substrate. Statistical mechanics gives us the tools necessary to predict the sum of these tunneling electrons, allowing us to calculate the current flow. In an STM, the tunneling current is fed into a feedback loop in order to control the tip to sample distance using piezo-electrics, and it is also used to generate the output image.

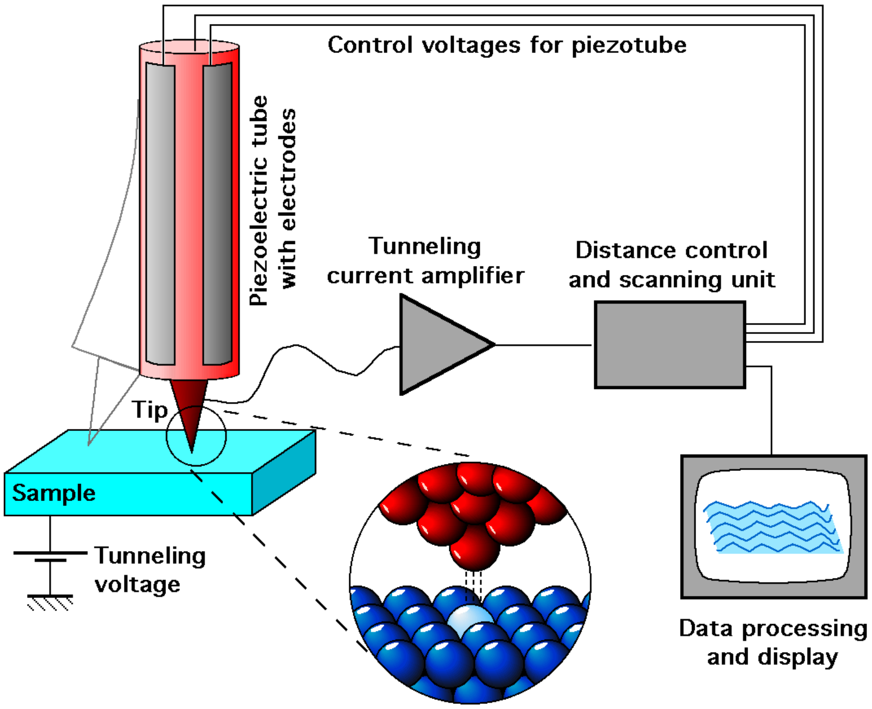

Figure 2.1: Principle components of a STM (Reproduced from ref. [2])

This system allows for two operating modes. Constant current mode, as its name implies, moves the tip at each point of the scan in order to maintain a constant tunneling current and measures the height at which this occurs. A much faster mode is the constant height mode, where the tip height is maintained and the tunneling current is measured and interpreted directly. This mode, however, risks the tip impacting with the surface and is therefore only used on known smooth surfaces.

Not only capable of producing images of nano-structured surfaces, the STM is also able to effect different mechanical manipulations; pushing, pulling and sliding atoms to arrange them in desired configurations [3]. The STM's remarkably high resolution is due to the strongly exponential dependence of the tunneling current upon the tip-to-surface distance, coupled with the extremely precise control afforded by piezo-electics. The theory behind the STM was described by Tersoff and Hamann in 1985 [4]. The tunneling current, as described by Bardeen is shown in equation 2.1 [5].

$$I = \frac{2\pi e}{\hbar} \sum_{\mu,v} f\left(E_\mu\right)\left[1 - f\left(E_v + eV\right)\right]\left|M_{\mu,v}\right|^2 \delta\left(E_\mu - E_v\right) \tag{2.1}$$

In this somewhat unwieldy expression, $f\left(E_\mu\right)$ is the Fermi function for the STM tip, $f\left(E_v + eV\right)$ is the Fermi function for the voltage-biased surface (eV) and $M_{\mu,v}$ is the tunneling matrix element between ψ_μ for the tip, and ψ_v for the surface. At high temperature there would also be a term describing the reverse tunneling but, since experiments are conducted at or below room temperature, this term may be ignored and, taking the limits of small voltages the expression can be simplified to equation 2.2.

$$I = \frac{2\pi}{\hbar} e^2 V \sum_{\mu,v} \left|M_{\mu,v}\right|^2 \delta\left(E_v - E_F\right)\delta\left(E_\mu - E_F\right) \tag{2.2}$$

Further simplification may be achieved by considering the tip to be a point probe, as the tunneling matrix is then directly proportional to ψ_v.

$$I \propto \sum_{v} \left|\psi_v\left(\vec{r}_0\right)\right|^2 \delta\left(E_v - E_F\right) \tag{2.3}$$

This simplification, equation 2.3, is known as the Tersoff Hamann approximation. It can be seen that the tunneling current may be assumed to depend on the squares of the wavefunctions for the surface atoms for energy levels at or near their Fermi level.

2.2 Atomistic Modelling

During the course of my research, I have made use of two computational chemistry methods, Molecular Mechanics (MM) and Density Functional Theory (DFT) in order to study the physical and electronic structure of various systems. The use of MM, in the form of Cerius^2[6], has been massively outweighed by the use of *AIMpro*'s DFT code[7], but it has proved useful for constructing structures relatively quickly and ensuring that they are chemically viable. These structures can then be used as starting points for more accurate analysis using the *AIMpro* code. While *AIMpro* is extremely fast and efficient for a DFT code, there is a price to pay for this and it lacks many of the "user-friendly" niceties of other packages.

2.2.1 Molecular Mechanics

MM is based on classical physics as opposed to the quantum mechanics used in electronic structure calculations. As such, atoms are broadly considered as masses and their attendant bonds as springs. While this approach may seem overly simplistic when compared with the solutions to the Schrödinger equation, it does have some distinct advantages. It is far less demanding in respect of computational resources and, as such, it is a useful tool for feasibility studies prior to the commitment of large quantities of resources. MM is also relevant when applied to very large systems such as the proteins and nucleotides studied by biochemists and the large, non-primitive unit cells that are required in materials science. The object of both electronic structure modelling and MM is to predict the energies associated with different conformations of a molecule or crystal structure. In the case of MM, this is achieved by the use of "force fields". Specific force fields differ in their details but are broadly similar.

2.2.1.1 Cerius^2

Cerius^2, in particular runs the Universal Force Field under Accelrys's proprietry Open Force Field engine as its default [8]. It involves the summation of bonded and non-bonded terms and can be expressed thus:

$$E = E_R + E_\theta + E_\phi + E_\omega + E_{el} + E_{vdw} \tag{2.4}$$

The bond stretch term, E_R, can be modelled as a harmonic oscillator:

$$E_R = \frac{1}{2} k_{ij} \left(r - r_{ij} \right)^2 \tag{2.5}$$

where k_{ij} is the Hooke's law constant, r is the natural bond length and r_{ij} is the length of the stretched or compressed bond.

Alternatively, it can be calculated as the Morse function:

$$E_R = D_{ij}[e^{-\alpha(r-r_{ij})} - 1]^2 \tag{2.6}$$

where D_{ij} is the bond dissociation energy and:

$$\alpha = \sqrt{\frac{k_{ij}}{2D_{ij}}} \tag{2.7}$$

The Morse function is the more accurate representation, better describing anharmonicity near equilibrium.

The three angular terms (E_θ for bending; E_ϕ for torsion and E_ω for inversion) are all described by small cosine Fourier transforms of the form:

$$E_\theta = K \sum_{n=0}^{m} C_n \cos n\theta \tag{2.8}$$

where K is the relevant angular force constant; the coefficients C_n are chosen specifically to satisfy boundary conditions such that the functions each yield minima at the natural bond angles and n signifies the number of terms in the Fourier expansions.

Atomic charges can be assigned within Cerius^2 and the electrostatic term, where required, is computed using Coulomb's law:

$$E_{el} = C\left(\frac{Q_i Q_j}{\epsilon} R_{ij}\right) \tag{2.9}$$

where Q_i and Q_j are the charges in electron units, ϵ is the relative dielectric constant (set to 1 as default in UFF) and C is set at 332.0637 to yield results in kcal/mol.

The van der Waals term is found with a Lennard-Jones 6-12 potential:

$$E_{vdw} = D_{ij}\left\{-2\left[\frac{r_{ij}}{r}\right]^6 + \left[\frac{r_{ij}}{r}\right]^{12}\right\} \tag{2.10}$$

where D_{ij} is the well depth, r_{ij} is the distance at which the potential reaches its minimum and r is the distance between the particles.

As MM is an empirical system, a set of parameters is required in addition to the equations. The Universal Force Field includes a parameter set for the majority of the periodic table.

2.2.2 Density Functional Theory

It has been said that:

> *While solutions to the Hartree-Fock equations may be viewed as exact solutions to an approximate description, the Kohn-Sham equations are approximations to an exact description!*[9]

This quotation, while rather glib, neatly illustrates a major difference between the two *ab initio* quantum mechanical calculation methods popular today; Hartree-Fock (HF) and density functional theory (DFT). The HF equations themselves are necessarily approximations but the various methods employed to solve them do so with precision. In DFT, it has been shown mathematically that while an exact functional exists linking ground-state energy and electron density, the form of that functional is unknown and approximations are included in the calculations to accommodate this. HF is a very useful technique but of limited use due to the way that the resources required to compute the correlation and exchange functionals scale unfavourably with increasing numbers of electrons in the system. DFT also suffers from this limitation, but nowhere near as badly as do the HF methods.

DFT's roots go all the way back to 1927, when Thomas and Fermi independently calculated the energy of an atom by representing its kinetic energy as a functional of the electron density [10][11]. A functional may be thought of as a function whose domain is a set of functions and is denoted by the use of square brackets. This was combined with classical expressions for the nucleus-electron and electron-electron interactions, both of which can also be represented in terms of the electron density. An exchange energy functional was added by Dirac in 1928 [12].

DFT builds on the Thomas-Fermi-Dirac theory with some major assistance from the ground-breaking Hohenberg-Kohn theorems and their proof that the ground-state electronic energy is determined completely by the electron density [13]. This would seem to simplify matters but, although it has been proven mathematically that each different electron density yields a different ground-state energy, the actual functional connecting these two quantities has yet to be derived.

The main problem with all the Thomas-Fermi models is that the kinetic energy is represented poorly. In 1965, Kohn and Sham revolutionised the field when they introduced their equations, splitting the kinetic energy functional into two parts, one of which, where the electrons are considered to be non-interacting, could be calculated exactly [14]. The difference between the exact kinetic energy and that calculated by assuming non-interacting orbitals is small and could then be absorbed into an exchange-correlation term.

A general energy expression for DFT using this concept is:

$$E[\rho] = T_s[\rho] - E_{ne}[\rho] + J[\rho] + E_{XC}[\rho] \tag{2.11}$$

where the first three terms may be calculated exactly and the last is an approximation for the exchange correlation energy.

The kinetic energy for a system of non-interacting electrons is given by:

$$T_s[\rho] = -\frac{\hbar^2}{2m_e}\sum_{i=1}^{n}\int \psi_i^*(r_1)\,\nabla_1^2\psi_i(r_1)dr_1 \tag{2.12}$$

the sum of the expectation values for the one-electron states, where ψ_i (i=1 to n) are the Kohn-Sham orbitals, which satisfy:

$$\rho(r) = \sum_{i=1}^{n}|\psi_i(r)|^2 \tag{2.13}$$

The nucleus-electron interactions are given by:

$$E_{ne}[\rho] = \sum_{I=1}^{N}\int \frac{Z_I}{r_1 - r_I}\rho(r_1)\,dr_1 \tag{2.14}$$

where the sum is over all N nuclei with index I, atomic number Z and location r_I. The Coulomb interaction between the total charge distribution is given by:

$$J[\rho] = \frac{1}{2}\int \frac{\rho(r_1)\,\rho(r_2)}{r_1 - r_2}dr_1dr_2 \tag{2.15}$$

A relatively simple yet robust method for evaluating the exchange-correlation term is the PW92 local density approximation (LDA), given by:

$$E_{XC}[\rho] = \int \rho(r)\,\epsilon_{XC}[\rho(r)]\,dr \tag{2.16}$$

where $\epsilon_{XC}[\rho(r)]$ is the exchange-correlation energy per electron in a homogeneous electron gas of constant density [15]. In the real world, however, the electron density is generally inhomogeneous and so a non-local correction can be added, involving the gradient of ρ, to produce a generalised gradient approximation (GGA). An example of this is the PBE96 functional [16].

2.2.2.1 AIMpro

The specific implementation of DFT that has been used in this thesis is the *AIMpro* code, an extremely efficient Gaussian orbital program. It was originally written to investigate defects in diamond and has been in development and use since the late 1980's [17], although details weren't published formally until it had been in use for around a decade [18]. As the mathematics underpinning DFT and the availability of computational resources have improved over the years, so the capability and efficiency of the *AIMpro* code has been improved to keep pace and the current iteration is both fast and reliable, equally at home on supercomputer clusters and modern desktop machines alike [19].

Some further aspects of the methodology behind *AIMpro* are worth discussing in more detail.

2.2.2.1.1 Modes

AIMpro can be used in two modes: cluster and supercell. The cluster mode, where the calculations are performed for an isolated moiety, was the original mode but is largely deprecated today unless there is a compelling reason for its use, such as symmetry constraints. Indeed, there is no support for the PBE-GGA functional in cluster mode, and it defaults to the PADE approximation to the PW92 functional [20].

Simply by defining a lattice, the user invokes *AIMpro's* supercell mode. The default exchange correlation in this mode is PW92-LDA but the user may select to employ the PBE-GGA functional where required. Supercell calculations can be run using either a reciprocal or a real space build of the Hamiltonian, defaulting to the reciprocal space build. Using the real space build can result in considerable speed gains, particularly for large systems, but also for smaller systems provided they have orthogonal lattice vectors.

These days, it is considered normal practice to use the supercell mode for all calculations. Isolated moieties may be represented by using a large enough supercell to preclude interactions with neighbouring cells.

2.2.2.1.2 k-Point Sampling

Since we are dealing with atoms arranged in a regular periodic structure, we need to take this periodicity into account when dealing with the electrons of the system. All of the integrals (equations 2.12, 2.14, 2.15 and 2.16) need to be performed over the first Brillouin zone. Bloch's theorem [21] states that the eigenstates ψ of the one-electron Hamiltonian:

$$H = -\frac{\hbar^2\nabla^2}{2m} + U(r) \tag{2.17}$$

where $U(r + R) = U(r)$ for all R in a Bravais lattice, can be chosen such that:

$$\psi(r) = e^{ik\cdot r}u(r) \tag{2.18}$$

where the periodic function $u(r{+}R) = u(r)$ and it is multiplied by the plane wave $e^{ik\cdot r}$. *AIMpro*, like most DFT packages replaces these integrals with a summation over special points in the first Brillouin zone. For the self-consistency and optimisation of structures, these special points are usually defined using the Monkhorst-Pack (MP) scheme [22]. If no mesh is defined, then *AIMpro* will assume that a Γ-point run is required. This would typically be the case where an isolated molecule is being examined as a "cluster in a box".

For the subsequent analysis runs there is a choice of methods. Once again, the MP scheme may be employed or an auxiliary file may be specified, defining either a set of discrete points or a path consisting of a number of straight lines through the Brillouin zone, defined by their end points. This latter method is particularly useful when defining the path required for bandstructure calculations.

2.2.2.1.3 Pseudopotentials

The use of pseudopotentials in *AIMpro*, and other codes, is another way of optimising the use of computer resources and improving calculation speeds. The pseudopotential mimics the requirement of the valence electrons to be orthogonal to the core electrons, by replacing the extra kinetic energy arising from orthogonality with a repulsive potential. Various types of pseudopotentials have been used by *AIMpro* historically, including those developed by Bachelet, Hamann and Schülter [23] and Troullier and Martins [24] but the ones in current use are those from Hartwigsen, Gœdecker and Hutter (HGH) [25], which are available for use in both LDA and GGA calculations. The *AIMpro* website has a selection of downloadable pseudopotential files together with their relevant basis sets.

2.2.2.1.4 Basis Sets

Coupled with the pseudopotential are the charge density and wavefunction basis sets, describing the behaviour of the valence electrons. These are optimised within *AIMpro* for specific molecular or structural environments and so the auxiliary potential file may contain many entries for use with different atomic, molecular and crystalline applications.

Optimisation of the charge density basis sets is necessary only when using the cluster code, as the charge density fit is used directly in the self-consistency process. When working in supercell mode this step is optional, as the charge density basis is only used to set up the initial charge density. As such, this step generally improves the speed of the calculation but has no effect on its accuracy.

The wavefunction basis sets can be of the contracted type, such as C44G*, but it is more common within *AIMpro* circles to use the uncontracted type and all of my research was performed using these. Describing a wavefunction by using an uncontracted basis set involves a series of fitting functions, made up from a combination of Gaussians of the form $e^{-\alpha r^2}$. Each of the radial Gaussians is converted into a series of increasing angular momentum by multiplication with a set of functions polynomial in the Cartesian coordinates ($x^i y^j z^k$), where $i = 0, l,\ j = 0, m$ and $k = 0, n$. Where $l = m = n = 0$ there is one function and it has s symmetry, where $l + m + n = 1$, three p symmetry functions are added and where $l + m + n = 2$, a further five d symmetry functions are included, together with an extra s symmetry function ($x^2 + y^2 + z^2$). So, an s-type function is described by a single Gaussian; a p-type by four (one for an "s" plus three for a "p") and a d-type by ten (one for an "s", three for a "p" and six for "d"). Thus a pdpp basis set, as used commonly in calculations involving graphite, would comprise 4 + 10 + 4 + 4 = 22 Gaussians.

2.2.3 Visualisation Software

I have employed two molecular visualisation packages in the preparation of images for this thesis. For images where no MOs are shown, I have used Pymol [26]. But for the majority of images, where MOs are shown and for the simulation of STM images, I have used *AIMview*[27].

That concludes the discussion of the relevant theory. We will now move on to examine the application of these concepts to some aspects of materials science that are felt likely to figure significantly in any future matter compilation project.

2.3 References

[1] G Binnig and H Rohrer. Scanning Tunneling Microscopy. *Surface Science*, 126:236–244, 1983.

[2] Webmaster. STM illustration. (http://en.wikipedia.org/wiki/), 2008.

[3] Don Eigler and E Schweizer. Positioning single atoms with a scanning tunnelling microscope. *Nature*, 344:524–526, 1990.

[4] J Tersoff and D R Hamann. Theory of the scanning tunneling microscope. *Physical Review B*, 31(2):805–813, 1985.

[5] J Bardeen. Tunnelling from a Many-Particle Point of View. *Phys Rev Lett*, 6(2):57–59, 1961.

[6] Accelrys. Cerius2 Molecular Modelling Package. *Accelrys Software Inc*, (ver 4.6), 2000.

[7] Patrick R Briddon and R Jones. LDA Calculations Using a Basis of Gaussian Orbitals. *Physica Status Solidi B*, 217(1):131–171, 2000.

[8] A K Rappe, C J Casewit, K S Colwell, W A Goddard Iii, and W M Skiff. UFF, a Full Periodic Table Force Field for Molecular Mechanics and Molecular Dynamics Simulations. *Journal of the American Chemical Society*, 114(25):10024–10035, 1992.

[9] Grant N Merrill, Scott Gronert, and Steven R Kass. Systematic Study of the Potential Energy Surface for the Base-Induced Elimination Reaction of Fluoride Ion with Ethyl Fluoride Using Density Functional Theory. *The Journal of Physical Chemistry A*, 101:208–218, 1997.

[10] L H Thomas. The Calculation of Atomic Fields. *Mathematical Proceedings of the Cambridge Philosophical Society*, (23):542–548, 1927.

[11] Enrico Fermi. Un Metodo Statistico per la Determinazione di alcune Prioprietà dell'Atomo. *Rend Accad Naz Lincei*, 6:602–607, 1927.

[12] P A M Dirac. Note on exchange phenomena in the Thomas atom. *Mathematical Proceedings of the Cambridge Philosophical Society*, 26:376–385, 1930.

[13] P Hohenberg and W Kohn. Inhomogeneous Electron Gas. *Physical Review*, 136(3B):B864–B871, 1964.

[14] W Kohn and L Sham. Self-consistent equations including exchange and correlation effects. *Physical Review*, 140(4A):A1133–A1138, 1965.

[15] John P Perdew and Yue Wang. Accurate and simple analytic representation of the electron-gas correlation energy. *Physical Review B*, 45(23):13244–13249, 1992.

[16] John P Perdew, Kieron Burke, and Matthias Ernzerhof. Generalized Gradient Approximation Made Simple. *Physical Review Letters*, 77(18):3865–3868, 1996.

[17] R Jones. The phonon spectrum of diamond derived from ab initio local density functional calculations on atomic clusters. *J Phys C: Solid State Phys*, (21):5735–5745, 1988.

[18] R Jones and Patrick R Briddon. The Ab Initio Cluster Method and the Dynamics of Defects in Semiconductors. *Semiconductors and Semimetals,*, 51(A):1–47, 1998.

[19] M J Rayson and Patrick R Briddon. Rapid iterative method for electronic-structure eigenproblems using localised basis .... *Computer Physics Communications*, (178):128–134, 2008.

[20] S Goedecker, M Teter, and J Hutter. Separable dual-space Gaussian pseudopotentials. *Physical Review B*, 54(3):1703–1710, 1996.

[21] Felix Bloch. Uber die Quantenmechanik der Elektronen in Kristallgittern. *Z Physik*, 52:555–600, 1928.

[22] M Methfessel and A Paxton. High-precision sampling for Brillouin-zone integration in metals. *Physical Review B*, 40(6):3616–3621, 1989.

[23] G Bachelet, D Hamann, and M Schlüter. Pseudopotentials that work: From H to Pu. *Physical Review B*, 26(8):4199–4228, 1982.

[24] N Troullier and José Luriaas Martins. Efficient pseudopotentials for plane-wave calculations. *Physical Review B*, 43(3):1993–2006, 1991.

[25] C Hartwigsen, S Goedecker, and J Hutter. Relativistic separable dual-space Gaussian pseudopotentials from H to Rn. *Physical Review B*, 58(7):3641–3662, 1998.

[26] Warren L DeLano. Pymol Molecular Graphics System. *Schrodinger*, (ver. 1.4.1), 2011.

[27] Jerry Hagon. AIMview Molecular Visualisation Package. *Newcastle University*, (ver. 1.1), 2011.

Chapter 3

Scanning Tunneling Microscope Tips

3.1 STM tips as Nanotools

Much of the practical research towards molecular manufacturing has focussed on the use of scanning probe microscopy in an attempt to manipulate single atoms or small functional groups, with Don Eigler's IBM logo picked out in xenon atoms on a nickel substrate being one of the better known early examples [1]. Meanwhile, on the theoretical side, the behaviour of SPMs is being modelled and computational models are being constructed examining various potential methods for "pick and place" assembly [2]. It seems likely that future nanomanufacturing equipment will include functionality based on scanning tunneling microscopy and so computer simulations of the processes involved offer an opportunity to advance the research significantly.

Regarding the tips, early simulations had a pressing need to conserve computing resources and tended to model the tip as a single atom, effectively ignoring any effects that might come from the bulk of the probe [3]. Since then, the capabilities of computers have been increased considerably and so it was decided to attempt to model some real-world tips more comprehensively, effectively taking more account of their overall structure.

3.2 Modelling Tungsten STM Tips

A brief search of suppliers' websites showed that STM tips manufactured from tungsten are a popular choice among manufacturers and that specific tips are available with their axes aligned perpendicular to either the (100) or (110) Miller indices [4]. It was decided initially that both of these tip types, along with tips aligned with the (111) axis, would be modelled in an increasingly sophisticated manner, beginning with just the tip atom and one supporting layer and adding more layers to increase the size of the model.

Some time prior to the actual calculations was devoted to the optimisation of both the charge density and wavefunction basis sets for tungsten. A 6 valence electron HGH pseudopotential was chosen and calculations were run under PBE-GGA. The charge density basis set was optimised using a body centred cubic unit cell, of lattice parameter 3.19 Å, with a 4 4 4 MP k-point mesh. Metallic filling and a temperature of $kT = 0.04$ eV were specified. Once this basis set had been converged, further runs were conducted in order to optimise the wavefunction basis set.

After discussions by email with Jon Goss it was decided that for a transition metal such as Tungsten, a minimum wavefunction basis level of dddd would likely be required. Accordingly, a dddd basis set was chosen and after optimisation, the lattice parameter and bulk modulus were compared to their accepted values of 3.165 Å and 310 GPa, respectively [5]. The results of the wavefunction basis set optimisation are shown in table 3.1. The values obtained were considered to be close enough to the accepted values that it was decided to proceed using that basis set.

Basis	a_0/Å	a_0/norm	BM/GPa	BM/norm
Literature value[5]	3.1652	1.0000	310.00	1.0000
dddd	3.1954	1.0095	291.77	0.9412

Table 3.1: Wavefunction basis set optimisation for BCC tungsten

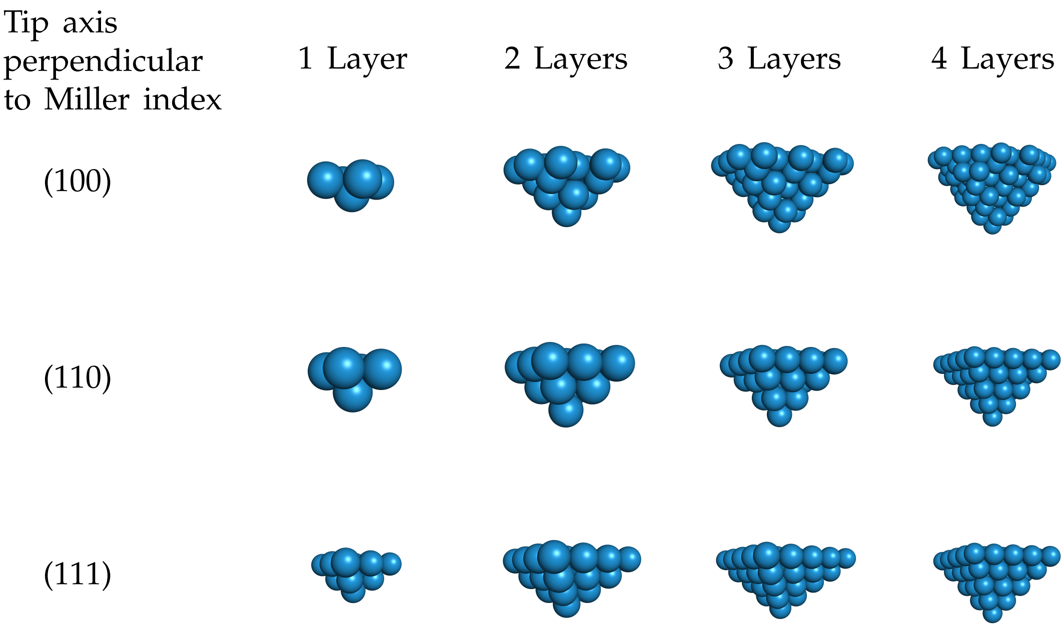

Figure 3.1: The initial, MM based models of various tungsten STM tips.

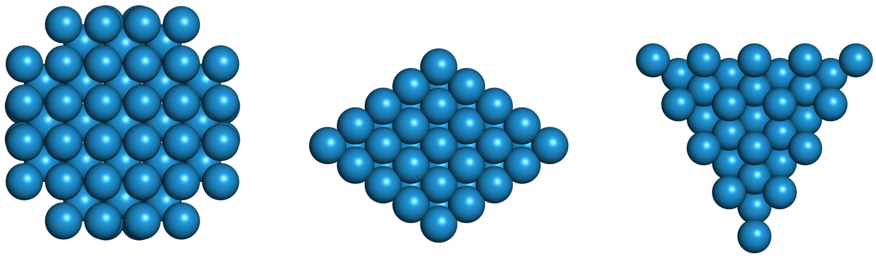
(100) (110) (111)

Figure 3.2: Typical tungsten tip models: plan views

The models, shown in Figures 3.1 and 3.2, were originally built using the Cerius^2 environment by constructing a supercell of BCC tungsten, aligning the atoms to suit the required axes, and then "cleaving" the models to produce an atomically sharp tip. In order to reduce unphysical strain in the model the lattice parameter for BCC tungsten was tweaked by using the converged figure from the *AIMpro* wavefunction basis set optimisation. No optimisation was carried out using MM. Instead, the positions of the atoms were exported for use as the initial atomic positions for optimisation and analysis runs under *AIMpro*. The tip models were placed within simple cubic unit cells (see Figure 3.3 for an example) containing enough vacuum that the atoms were effectively prevented from interacting with the adjacent cell. By treating the tips as periodic systems rather than clusters, *AIMpro* was able to utilise its more efficient and precise Fourier transformed charge density. Since these "clusters in a box" aren't true periodic systems and have no electronic interactions with neighbouring unit cells, no k-point mesh was specified and *AIMpro* was allowed to sample at the gamma point only. Calculations were again run under PBE-GGA and the

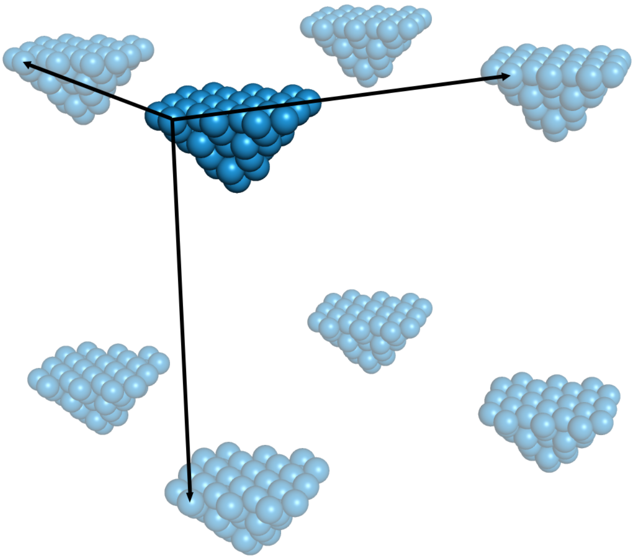

Figure 3.3: Example of tungsten STM tip model and the lattice vectors of its simple-cubic unit cell. This is the 3 layer (100) tip.

previously optimised dddd basis set was employed.

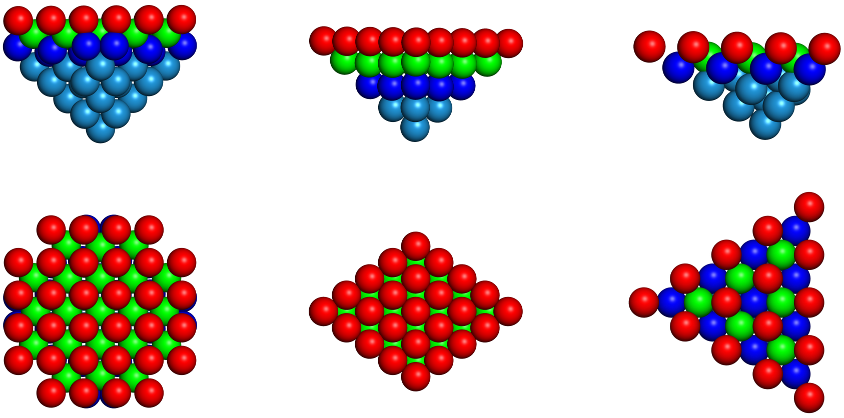

(100) (110) (111)

Figure 3.4: Typical tungsten tip models showing the nature of atomic layering. Colour has been used to distinguish atoms in specific layers.

The top sections of the models were held in place during the optimisation process. These "top sections" were the parts of the models that were felt necessary model the solidity due to layers of atoms above the actual tip. For the simplest models, they simply comprised the upper layer of atoms but, as the complexity was increased, (and especially with the (111) layer models) more layers had to be held in order to achieve this. For the larger (100) models, 2 sub-layers were held; for the (110) models 1 layer was always sufficient; while for the (111) models, 3 sub-layers were required. The nature of the layering in the various models is illustrated in Figure 3.4.

This strategy worked well for all the (100) and (110) models, with some contraction of the tip atom and surface facets apparent as expected. The values for the energy per atom for the optimised structures are presented in tables 3.2 and 3.3 and figure 3.5. The energy per atom decreases as the complexity of the models is increased. This behaviour is perfectly reasonable as it is a consequence of the changing ratio of surface to bulk atoms, with surface atoms being intrinsically less energetically favourable than those in the bulk.

The (111) tip models, especially the largest of them, showed a marked

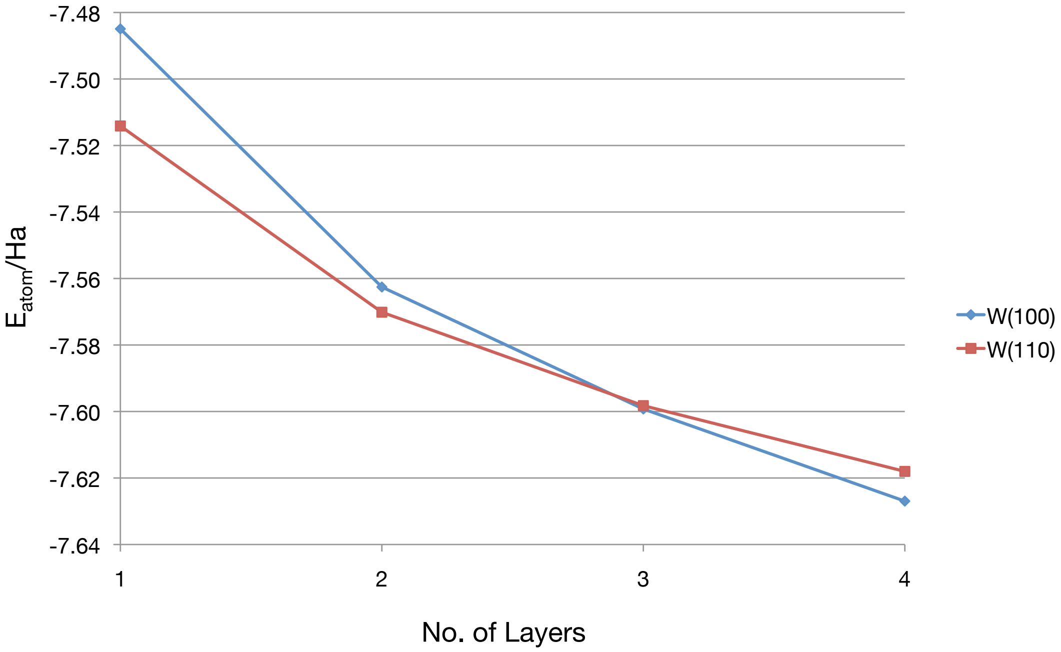

Figure 3.5: Energy per atom for the optimised STM tip models

reluctance to maintain their structural integrity during optimisation. Some further research revealed that Tracy and Blakely [6] had noted the relative instability of the tungsten (100) facets that would characterise such a tip, and the tendency for them to transform into stable (110) planes. In light of this, it was decided to discontinue work on the (111) simulations in favour of the more stable and realistic (100) and (110) models.

3.3 Analysis of Wavefunctions

Once the (100) and (110) tips were fully relaxed, analysis runs were conducted in order to generate the dump files necessary for aimview to visualise their

No. of Layers	No. of Atoms	E_{atom}/Ha
1	5	-7.485
2	22	-7.563
3	59	-7.599
4	112	-7.627

Table 3.2: Energy per atom for the optimised W(100) STM tip models

No. of Layers	No. of Atoms	E_{atom}/Ha
1	5	-7.514
2	14	-7.570
3	30	-7.598
4	55	-7.618

Table 3.3: Energy per atom for the optimised W(110) STM tip models

wavefunctions. For each tip, the energy levels for the HOMO and LUMO were identified by counting the valence electrons in the systems. The wavefunctions of the HOMO and LUMO for the (100) tip models are illustrated in Figure 3.6 and those for the (110) tip models are shown in Figure 3.7. It should be notes that, for larger tips, only a portion of the energy levels above and below the frontier orbitals were calculated in order to conserve computer resources.

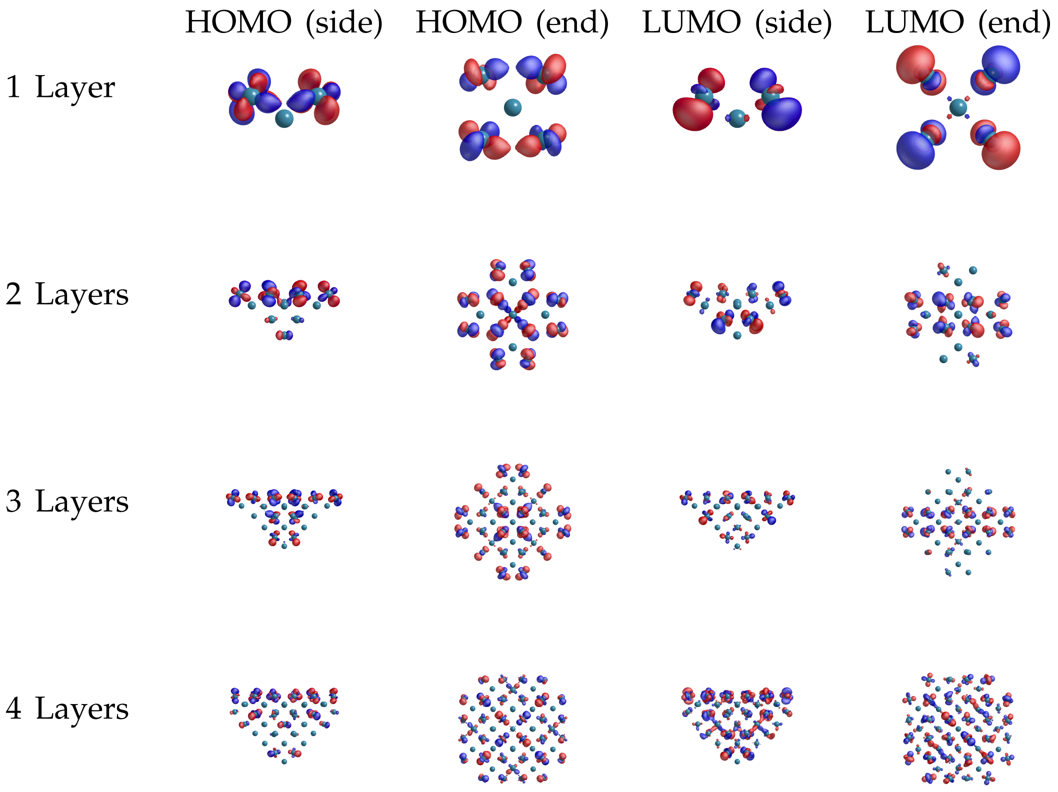

Figure 3.6: The HOMO and LUMO for the tungsten (100) STM tip models.
Larger versions are presented in the Appendix, Figures A.1 to A.4

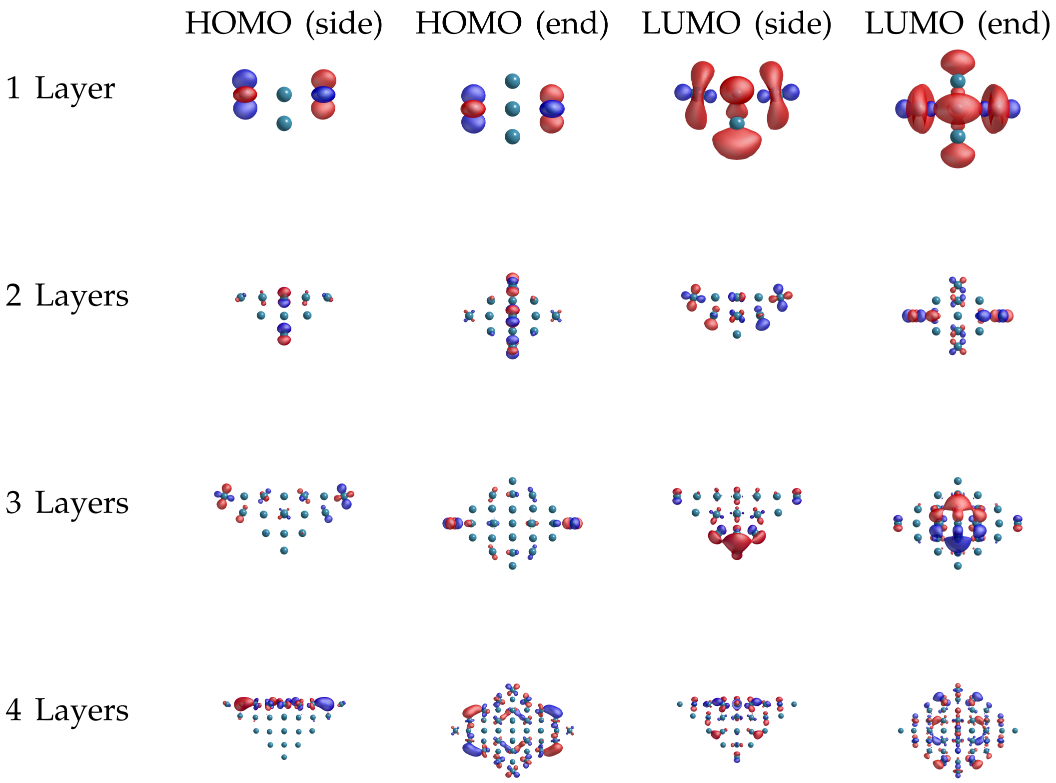

Figure 3.7: The HOMO and LUMO for the tungsten (110) STM tip models.
Larger versions are presented in the Appendix, Figures A.5 to A.8

For example, the (100) 3 layer model comprised of 59 atoms. Using 6 valence electrons per atom, the HOMO would be level 177 and the aimview dump file was calculated for levels 167 - 197.

All of the models' wavefunctions appear significantly more complex than anything that could be approximated by a point-source and so this investigation has shown that a more rigorous method of simulating STM tips is desirable. The results of the energy per atom analysis noted earlier cause something of a dilemma, though. The smaller structures are, in general, the easiest to model but they represent the tips poorly due to their high energy per atom. The larger structures, on the other hand, may better represent the tips' overall structure, but they are much more computationally intensive. If a more rigorous approach to tip modelling is to be adopted then a balance between these extremes will have to be found.

The wavefunctions of the (100) tip models show some similarity of form as complexity is increased, with a marked concentration of electron density just behind the tip and another concentration on the "upper" layer, where the bulk of the material would be in a real tip. In the case of the (110) models, things are not so clear-cut. While there is some concentration of electron density near where the bulk of the tip would be, and the complexity of the wavefunctions increases with the models' complexity, there doesn't appear to be any particular pattern to it.

Unfortunately, this simulation doesn't seem to differentiate adequately between the tip atom itself and other atoms at the extremities of the models. It would seem likely that, in order to simulate STM tips more effectively, the models would need to take account of the presence of the bulk of the material in some way. In spite of that, it may be instructive to examine the extent of the Tersoff-Hamann approximation by placing some of these models, particularly the (100) ones, in close proximity to a model surface and observing any changes that are induced in the surface wavefunctions.

3.4 References

[1] Don Eigler and E Schweizer. Positioning single atoms with a scanning tunnelling microscope. *Nature*, 344:524–526, 1990.

[2] D Mann, Jingping Peng, Robert A Freitas Jr, and Ralph C Merkle. Theoretical Analysis of Diamond Mechanosynthesis. Part II. C2 Mediated Growth of Diamond C(110) Surface via Si/Ge-Triadamantane Dimer Placement Tools. *Journal of Computational Theoretical Nanoscience*, 1:71–80, 2004.

[3] W A Hofer, J Redinger, and R Podloucky. Modeling STM tips by single absorbed atoms on W (100) films: 3d and 4d transition-metal atoms. *Physical Review B*, 64:125108, 2001.

[4] Webmaster. Applied Physics Technologies. (http://www.a-p-tech.com/stmtips.htm), 2008.

[5] Mark Winter. WebElements Periodic Table of the Elements. (http://www.webelements.com/tungsten/), 2008.

[6] J C Tracy and J M Blakely. A study of facetting of tungsten single crystal surfaces. *Surface Science*, 13(2):313–336, 1969.

Chapter 4

Substrates as Nano-Workbenches

The nanoscale tool-tip is only one part of the story, though. Any ambition to assemble moieties in a machine-phase reaction will also likely require the nanoscale equivalent of a workbench. Some kind of conducting substrate capable of interacting weakly with potential reactant molecules will likely be needed.

It was felt that graphitic carbon nanostructures, with their conjugated π system may well provide such a substrate. Additionally, there are a variety of known defect types associated with such materials that may be able to provide useful anchorage points. Any future matter compiler employing such a substrate would need to be able to identify these potential anchorage points. With this in mind, research was undertaken into the nature of the π-π interaction in graphite and layered graphene, and a method for simulating STM images of pristine and defected graphitic surfaces was developed.

4.1 Graphitic Materials

4.1.1 Bulk Graphite

The investigation into the π-π interaction was conducted by modelling the basic 4 atom, hexagonal graphite unit cell, as shown in Figure 4.1. The carbon

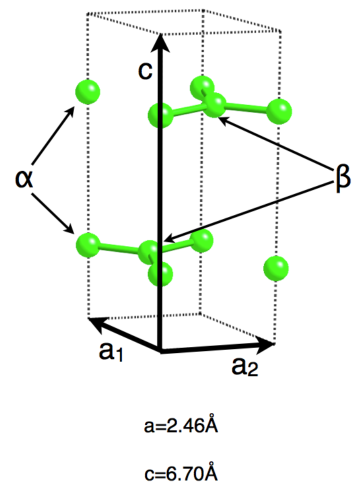

Figure 4.1: The hexagonal Graphite unit cell. Dimensions from Webelements [1]

atoms can be located on one of 2 sublattices, labelled α and β. The α sublattice comprises the atoms that are coincident when viewed from the direction of the c-axis, while the β sublattice comprises those that are offset.

Figure 4.2 gives details of the construction of the first Brillouin zone for a hexagonal lattice. First, the reciprocal lattice vectors were calculated according to equations 4.1 and 4.2.

$$\bar{b}_1 = \frac{(\bar{a}_2 \times \bar{c})}{(\bar{a}_1 \times \bar{a}_2) \cdot \bar{c}} \tag{4.1}$$

$$\bar{b}_2 = \frac{(\bar{c} \times \bar{a}_1)}{(\bar{a}_1 \times \bar{a}_2) \cdot \bar{c}} \tag{4.2}$$

Then, all of the vectors from a known point in reciprocal space to all of its nearest equivalent points were bisected to produce the first Brillouin zone. Sampling was conducted using a MP 4 4 4 grid and a pdddp basis set was used.

Runs were conducted under LDA. This conscious decision requires a little justification as there is some controversy regarding the choice of exchange correlation functionals when modelling graphite with DFT. In much of materials science, the use of GGA is now considered to be more rigorous than the use of LDA and has supplanted it in many applications. Regarding graphitic

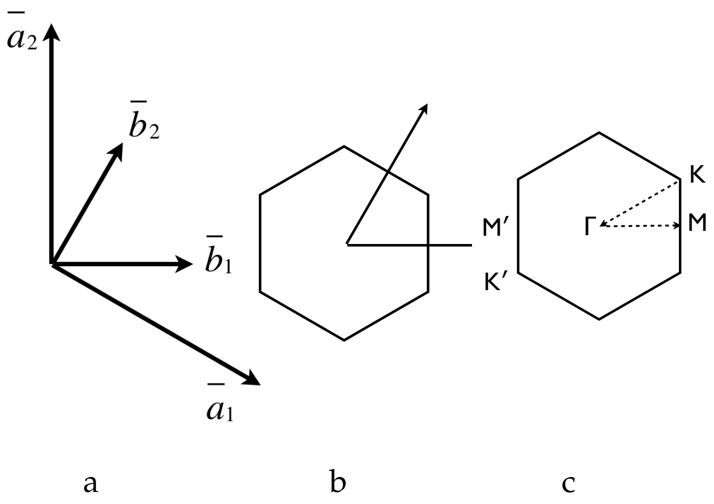

Figure 4.2: Construction of first Brillouin zone for a hexagonal lattice.
a: The lattice vectors and their equivalents in reciprocal space. b: The first Brillouin zone produced by bisecting all the paths to the nearest neighbouring points in reciprocal space. c: The Γ, K, K′, M and M′ points illustrated.

materials, a commonly held view is that dispersion forces are responsible for the interlayer forces and that since no account is taken of these dispersion forces in DFT, neither method reproduces the interlayer separation adequately. LDA, it is said, tends to give the right answer for the wrong reasons [2], while GGA yields a repulsion or a minimal attraction, placing the layers much too far apart. One method that has found favour in the past is to use GGA and to "lock" the ratio between the basal lattice parameter and the interlayer separation artificially, thus ensuring that the experimentally observed separation is achieved, but this hardly seems ideal as it introduces experimental parametisation into what should be an *ab initio* calculation [3].

The argument for dispersion as the main interlayer force requires there to be no overlap between the orbitals of neighbouring layers but, as this section of the thesis shows, that is not the case. Optimisation of the graphite lattice under LDA and subsequent analysis runs to generate the bandstructure (see Figure 4.3) and the wavefunctions at the K point reveal that there is an overlap between π orbitals of the HOMO -1 on the atoms of the α

sublattice, as illustrated in Figure 4.4, producing a bonding orbital. The corresponding anti-bonding orbital is the LUMO +1. Between these are

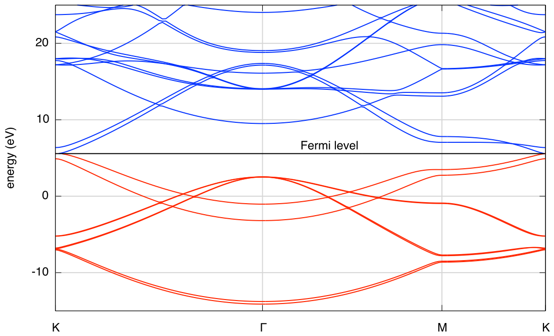

Figure 4.3: The bandstructure of A-B stacked graphite.
A larger version is presented in the Appendix, Figure B.1

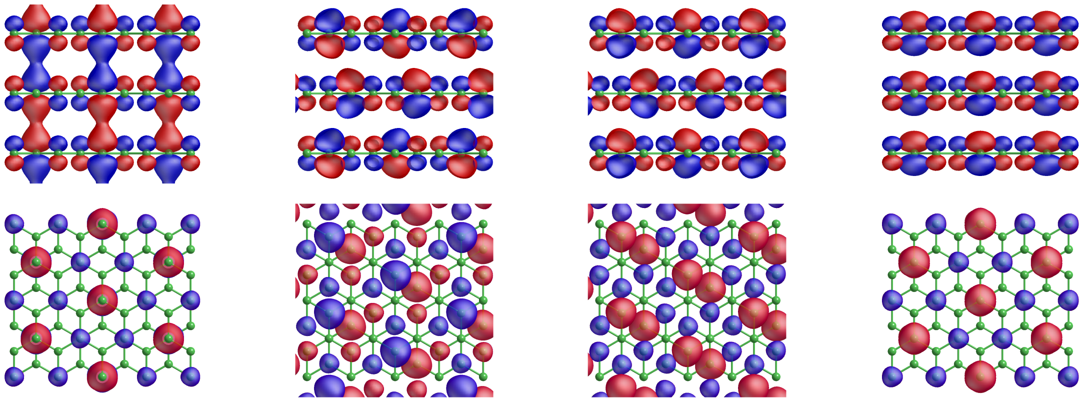

HOMO -1
(bonding)

HOMO
(non-bonding)

LUMO
(non-bonding)

LUMO +1
(anti-bonding)

Figure 4.4: The molecular orbitals responsible for the interlayer bonding in graphite.
A larger version is presented in the Appendix, Figure A.9

the HOMO and LUMO, with their electron density concentrated on the β sublattice. An examination of the orbitals on atoms in neighbouring layers on this sublattice reveals incompatibility between their point group symmetry and so these orbitals are non-bonding. Thus, there is a chemical bond, albeit a rather weak one, between neighbouring c-axis atoms on the α sublattice and the interlayer binding arises from this conjugated system.

It should be noted here that optimisation of the lattice under LDA gives an extremely good match between the calculated and experimental structures, with a lattice parameter of 2.446 Å in the "a" direction and 6.582 Å in the direction of the "c" axis, compared with literature values of 2.46 Å and 6.70 Å respectively [1].

4.1.2 Graphene

Graphene may be thought of as a single layer of graphite. Indeed, early researchers prepared it by simple, mechanical exfoliation of graphite using adhesive tape [4][5]. *AIMpro* runs were conducted using similar parameters to the runs on bulk graphite but the c-axis parameter was set to 48 au (around 25 Å) for two reasons. The main reason was in order to preclude any interaction between neighbouring layers. The second consideration was that a particularly large separation would allow additional layers to be placed in the same cell, enabling direct comparisons between graphene and its multi-level equivalents.

In contrast to graphite, there is no stacking of layers (until we consider multi-layer graphene), but it is still hexagonal with a basis of two coplanar atoms and, as the lattice is very similar, it is useful to compare the two materials' bandstructures and molecular orbitals. The bandstructure is shown in Figure 4.5 and the molecular orbitals in Figure 4.6.

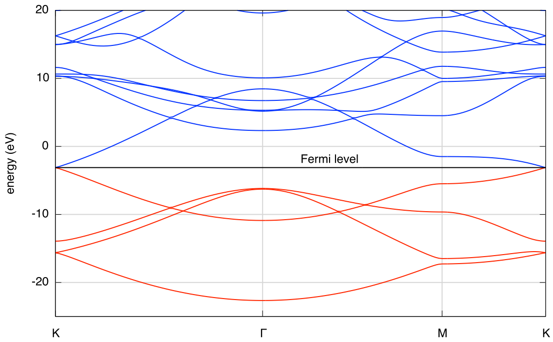

Figure 4.5: The bandstructure of graphene.
A larger version is presented in the Appendix, Figure B.2

Comparing the bandstructure to Figure 4.3, it should be noted that there are significant differences between the behaviour of the bands at the K point. The bands in graphite consist of the degenerate HOMO and LUMO, as well as the HOMO-1 and LUMO+1 forming a small band gap. In graphene, the HOMO and LUMO cross and form a Dirac point at K, responsible for the unusual zero-mass fermions noted by Geim and Novoselov [6].

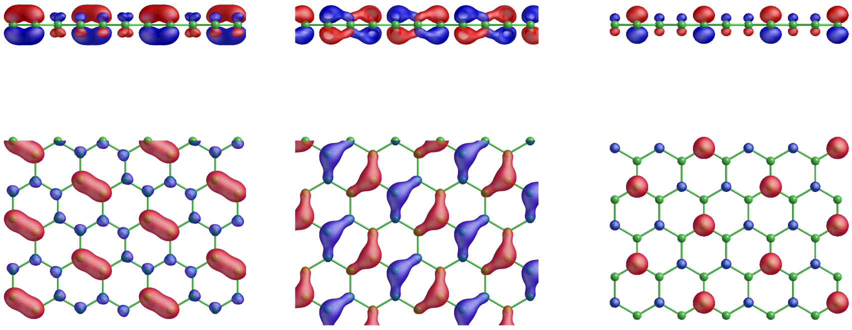

HOMO
(bonding)

LUMO
(anti-bonding)

HOMO+LUMO
(linear combination)

Figure 4.6: The molecular orbitals of graphene.
A larger version is presented in the Appendix, Figure A.10

These two wave functions are degenerate at E_F at K and their pseudospin character is not directly evident because they appear as linear combinations of the pseudospin states. Adding them as a linear combination produces the familliar wavefunction as illustrated.

As an aside, it is appreciated that the use of the terms HOMO and LUMO is not, strictly speaking, appropriate here. However, the nomenclature is widely understood and very useful in describing the ordering of wavefunctions around the Fermi level. Since this degeneracy only occurs at the K point in graphitic-type structures and is resolved elsewhere in the Brillouin zone by band-splitting, I will continue to employ it in the interests of clarity.

4.1.3 Bi-layer Graphene

In bi-layer graphene, the atoms are ordered in a similar manner to graphite. There are α and β atoms and it might be expected that the bandstructure and molecular orbitals should reflect this. The bandstructure is presented in Figure 4.7 and the orbitals are illustrated in Figure 4.8. The bandstructure resembles that of graphite, except that the HOMO-1 and LUMO+1 bands lie somewhat "tighter" to the degenerate, non-bonding HOMO and LUMO. The energies at point K are -2.1657 eV, -1.8005 eV and -1.4272 eV for the HOMO-1, the degenerate HOMO/LUMO and the LUMO+1, respectively.

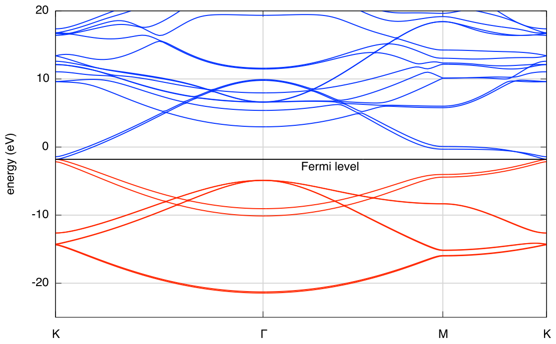

Figure 4.7: The bandstructure of bi-layer graphene.
A larger version is presented in the Appendix, Figure B.3

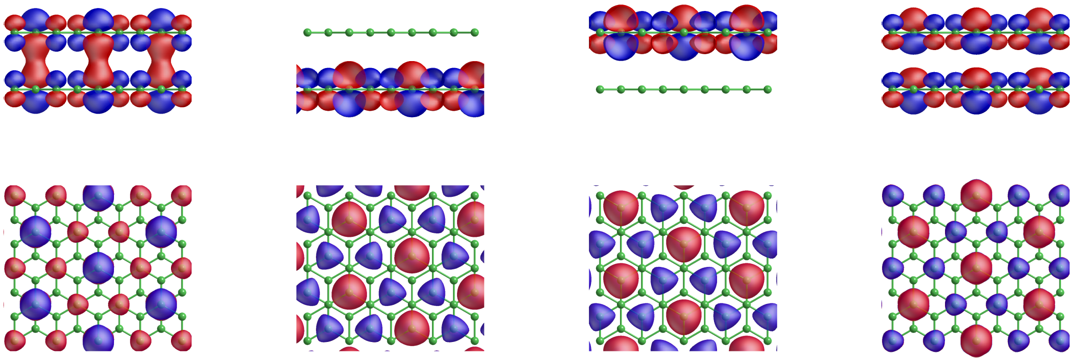
HOMO -1
(bonding)
HOMO
(non-bonding)
LUMO
(non-bonding)
LUMO +1
(anti-bonding)

Figure 4.8: The molecular orbitals of bi-layer graphene.
A larger version is presented in the Appendix, Figure A.11

The bonding and anti-bonding orbitals do indeed resemble those of A-B graphite, with their electron density concentrated on the α atoms. Regarding the two non-bonding orbitals, although their electron density is concentrated on the β sites as in graphite, each is concentrated on only one layer of atoms. In fact, bi-layer graphene could be considered to have three sublattices, compared to graphite's two: one α and two discrete βs, one for each layer. However, these levels are degenerate and if they are combined, as in Figure 4.9, then they form an orbital with the appearance of the LUMO of A-B graphite.

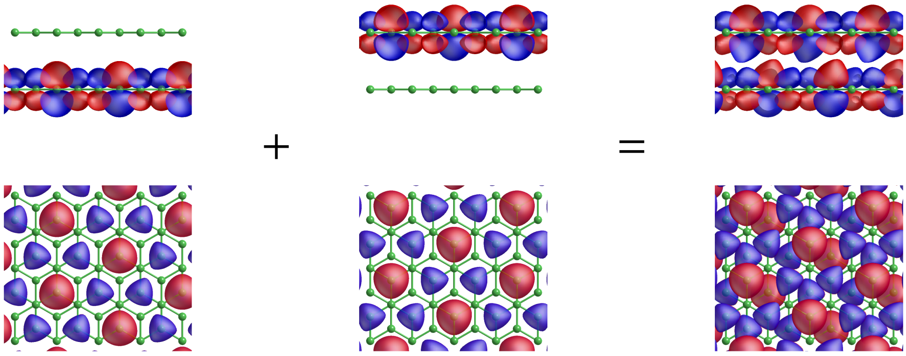

HOMO LUMO

Figure 4.9: Combining the non-bonding orbitals of bi-layer graphene.
Note the similarity between the resulting orbital and the LUMO for A-B stacked graphite in Figure 4.4

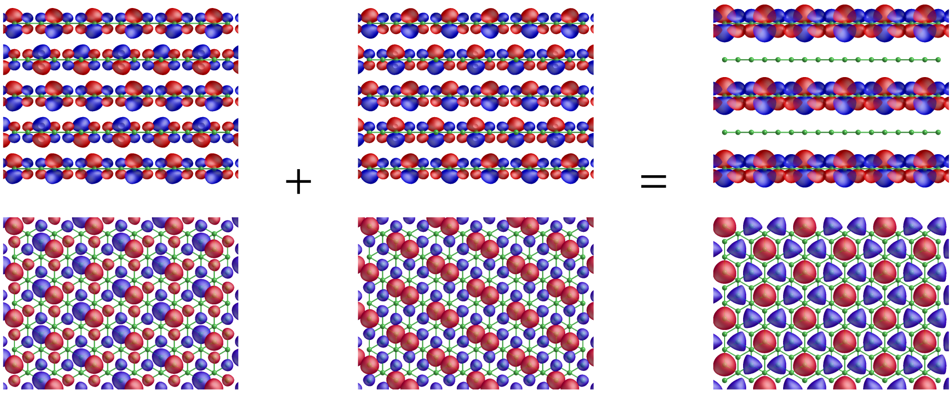

HOMO LUMO

Figure 4.10: Combining the non-bonding orbitals of A-B stacked graphite.
Note the similarity between the resulting orbital and the LUMO for bi-layer graphene in Figure 4.8

Interestingly, the process seems to work in reverse, too. Figure 4.10 shows the result of combining the non-bonding HOMO and LUMO of A-B stacked graphite. The resulting combination of orbitals concentrates electron density on alternating layers in a similar manner to the way that bi-layer graphene's HOMO and LUMO behave.

Since there is overlap between the bonding orbitals of the α atoms, and since these are nearest-neighbour interactions, it is possible to analyse the system using Hückel theory [7]. In the case of the bi-layer, this may be thought of as being analogous to a simple two carbon atom molecule such as ethene, where:

$$E_n = \alpha + c_n\beta \tag{4.3}$$

with c_1=1 and c_2=-1. These coefficients may be plotted against the energies at point K to calculate values for α and β. Figure 4.11 illustrates this and yields values of -1.792 eV and -0.365 eV for α and β, respectively.

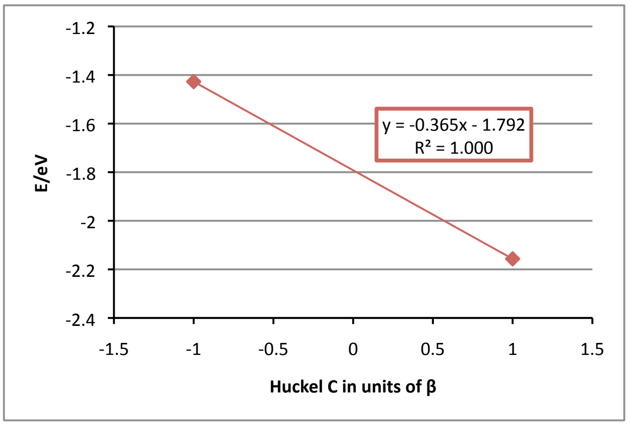

Figure 4.11: Hückel coefficient plotted against energy for bi-layer graphene.

4.1.4 Tri-layer Graphene

Tri-Layer graphene adds to the complexity of the model by including a third layer. There are still α and β atoms but the two kinds of β sites are more distinct. The atoms on the β sites on the central layer have no corresponding atoms in the c direction. These atoms will be referred to as β_1 atoms. The atoms at the β sites on the outer layers correspond to each other in the c direction. Atoms on these sites will be designated as β_2 atoms. The bandstructure is presented in Figure 4.12 and the orbitals are illustrated in Figures 4.13, for the bonding and anti-bonding orbitals and 4.14 for the non-bonding ones.

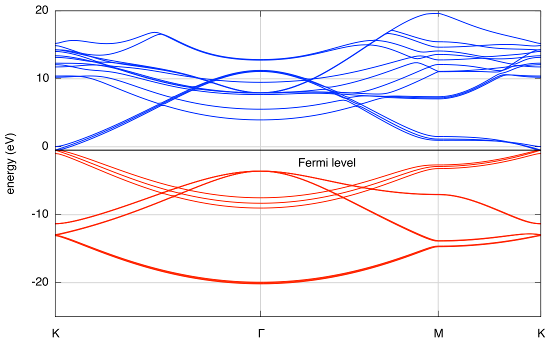

Figure 4.12: The bandstructure of tri-layer graphene.
A larger version is presented in the Appendix, Figure B.4

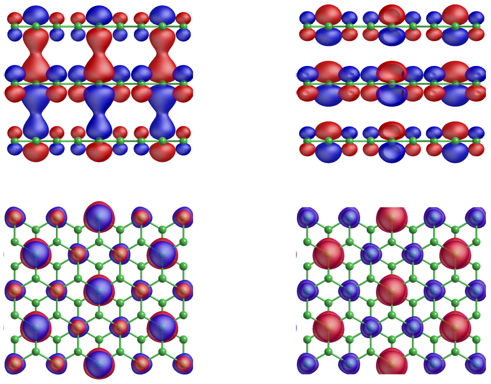

HOMO-2
(bonding)

LUMO+2
(anti-bonding)

Figure 4.13: The bonding and anti-bonding orbitals of tri-layer graphene.
A larger version is presented in the Appendix, Figure A.12

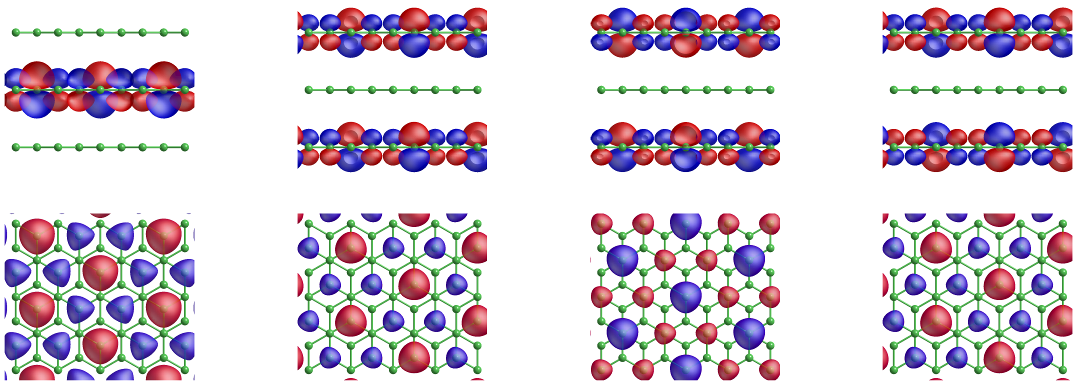

HOMO -1 (non-bonding)
HOMO (non-bonding)
LUMO (non-bonding)
LUMO +1 (non-bonding)

Figure 4.14: The non-bonding orbitals of tri-layer graphene. A larger version is presented in the Appendix, Figure A.12

Once again, the bandstructure resembles that of graphite, except that now there are four degenerate non-bonding orbitals at the K point. The bonding and anti-bonding orbitals on the α atoms are now the HOMO-2 and LUMO+2, respectively and it can easily be seen that there is significantly more electron density on the central layer. The degenerate non-bonding orbitals are no longer confined solely to the β sites. The HOMO-1 is on the β_1 atoms; the HOMO and the LUMO+1 are on the β_2 atoms; but the LUMO is now located on the α atoms, although only those of the two outer layers.

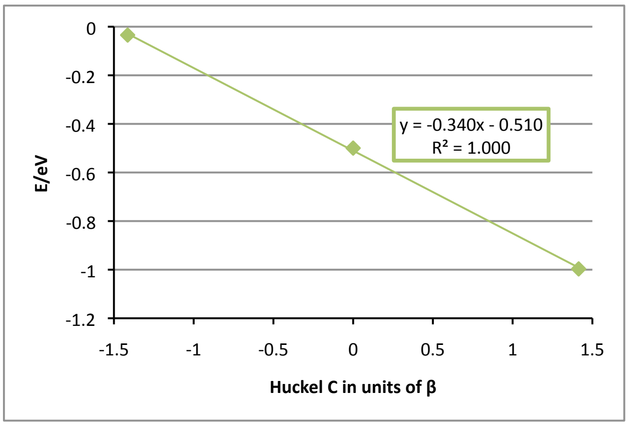

Figure 4.15: Hückel coefficient plotted against energy for tri-layer graphene.

AIMpro gives the energies of the HOMO-2, the four degenerate non-bonding orbitals and the LUMO+2 as -0.9969 eV, -0.4996 eV and -0.0344 eV respectively. Turning to Hückel theory once more, tri-layer graphene may be thought of as analogous to a three carbon atom molecule such as the allyl radical. These energies may be plotted against the coefficients obtained from the solution of a three atom secular determinant, 1.414, 0 and -1.414 as in Figure 4.15. This gives values for α of -0.510 eV and for β of -0.340 eV.

4.1.5 Quad-layer Graphene

Adding another graphene layer increases the system's complexity once more, although the three sublattices, α, β_1 and β_2 are sufficient to describe the positions of the carbon atoms and the positions of the orbitals. The bandstructure is presented in Figure 4.16 and the orbitals are illustrated in Figures 4.17, for the bonding and anti-bonding orbitals and 4.18 for the non-bonding ones. The bandstructure is still very graphitic in nature, with another pair of discrete bands in evidence.

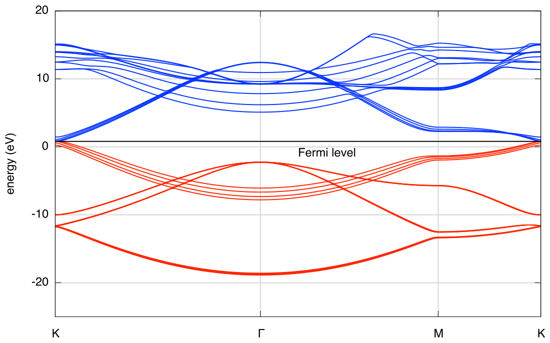

Figure 4.16: The bandstructure of quad-layer graphene.
A larger version is presented in the Appendix, Figure B.5

The system of bonding and anti-bonding orbitals is significantly more complex for this system. The electron density for the HOMO-3 (bonding) and the LUMO+3 (anti-bonding) is more pronounced between layers three and four, and not all of the levels between them can be described as non-bonding. The HOMO-2 shows significant bonding character between layers one and two and

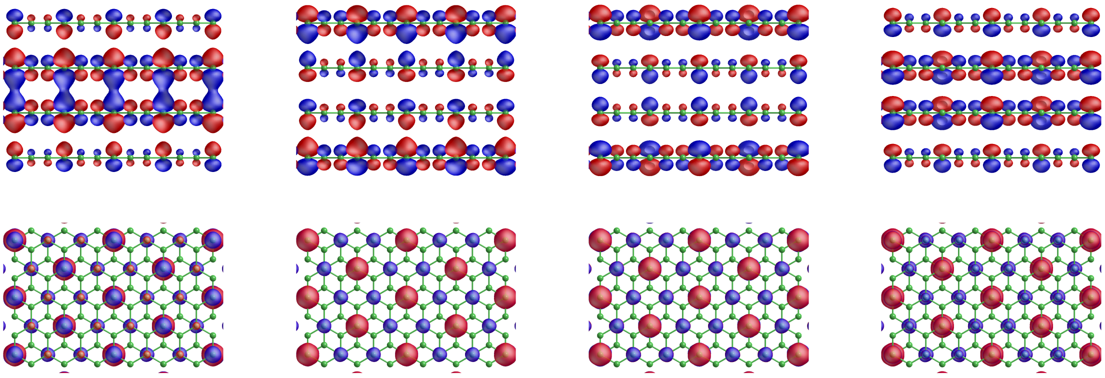

HOMO-3
(bonding)
(all layers)

HOMO-2
(bonding)
(not layers 2 and 3)

LUMO+2
(anti-bonding)
(not layers 2 and 3)

LUMO+3
(anti-bonding)
(all layers)

Figure 4.17: The bonding and anti-bonding orbitals of quad-layer graphene.
A larger version is presented in the Appendix, Figure A.13

between layers three and four, but it also shows some anti-bonding character between layers two and three. The LUMO+2 shows the opposite character, with significant anti-bonding between layers one and two and between layers three and four, but some bonding character between layers two and three. All of these bonding and non-bonding orbitals are located on all of the α atoms.

There are four non-bonding molecular orbitals: the HOMO-1, the HOMO, the LUMO and the LUMO+1. They alternate positioning on the β_1 and β_2 sublattices and, unlike those of tri-layer graphene, none of them sit on any α sites. Also, each of the non-bonding orbitals is primarily concentrated on a specific layer, with the two orbitals lower in energy sitting mainly on the inner layers.

AIMpro gives the energies of the HOMO-3 and HOMO-2 bonding orbitals as 0.2513 eV and 0.5956 eV, and the non-bonding LUMO+2 and the LUMO+3 as 1.0450 eV and 1.4313 eV respectively. The four non-bonding orbitals are split as two pairs of degenerate levels at 0.8038 eV and 0.8292 eV. In Hückel theory we can treat quad-layer graphene as analogous to a four carbon atom molecule such as butadiene. The two pairs of non-bonding orbitals are neglected since

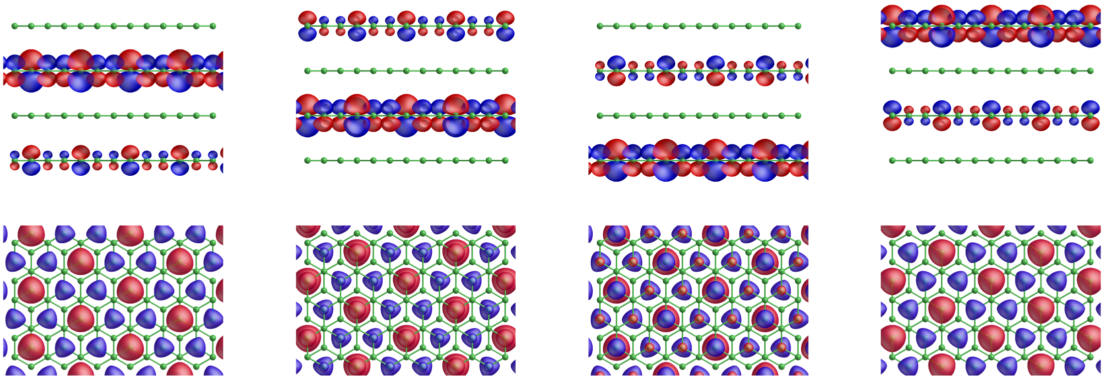

HOMO -1
(non-bonding)

HOMO
(non-bonding)

LUMO
(non-bonding)

LUMO +1
(non-bonding)

Figure 4.18: The non-bonding orbitals of quad-layer graphene.
A larger version is presented in the Appendix, Figure A.14

Hückel theory only applies to nearest neighbour interactions. The energies of the bonding and anti-bonding levels may be plotted against the coefficients obtained from the solution of a four atom secular determinant, 1.618, 0.618, -0.618 1and -1.618 as in Figure 4.19. This gives values for α of 0.831 eV and for β of -0.365 eV.

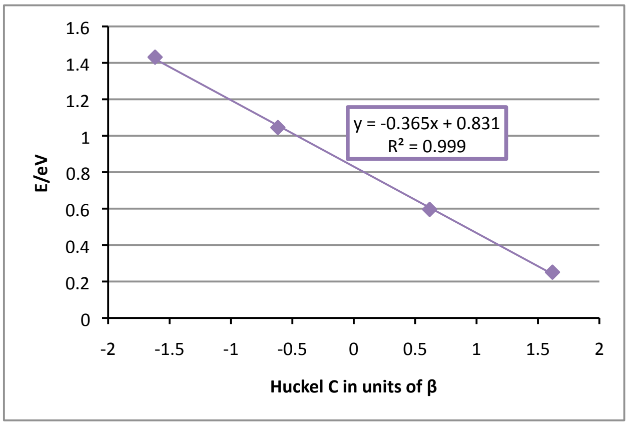

Figure 4.19: Hückel coefficient plotted against energy for quad-layer graphene.

4.1.6 Collation of Hückel Analysis of Multi-layer Graphenes

The three data sets from the Hückel theory analysis of bi, tri and quad-layer graphenes may be plotted together by setting their respective α coefficients to zero. This produces the graph in Figure 4.20. The remarkably good agreement of the three slopes shows that Hückel theory holds true for the interlayer binding in multi-layer graphenes. Consequently, it can be concluded that this interaction has significant covalent characteristics and, as such, it is entirely appropriate to treat calculations on graphitic structures using LDA as valid.

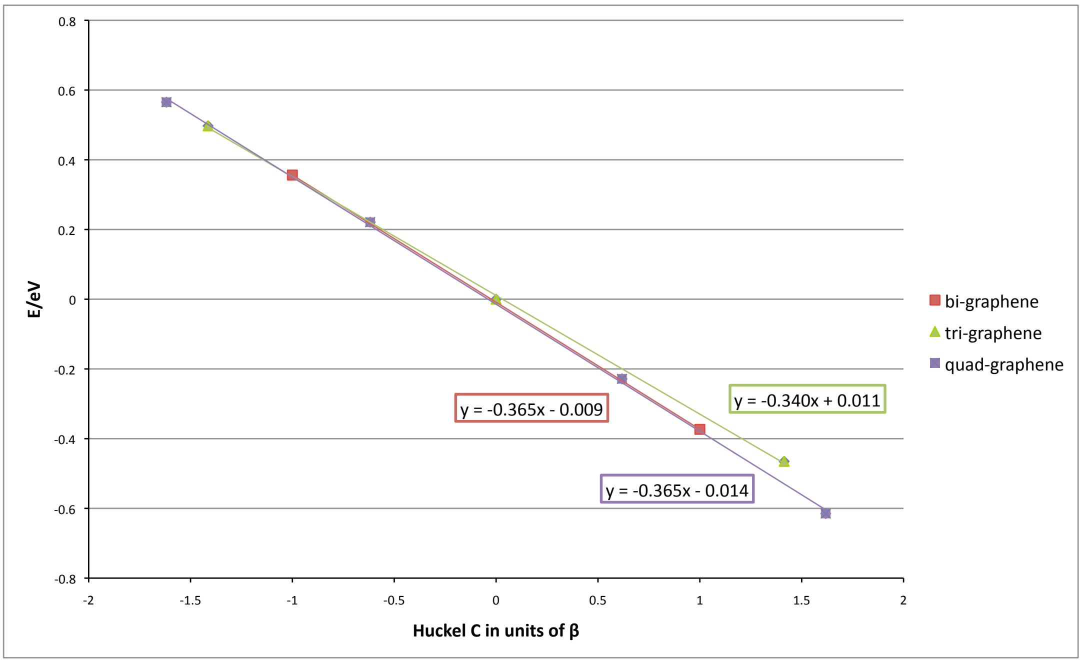

Figure 4.20: Hückel β coefficient plotted against energy differences for the multi-layer graphenes.

4.2 Pristine and Defected Surfaces

When moving on to examine the graphitic surface, both pristine and defected, a larger unit cell was constructed by repeating the standard 4 atom cell 8 times along the basal lattice vectors. The c-axis lattice vector was increased to 25Å in order to create a system of surfaces with sufficient vacuum between them to preclude interaction. The resulting pristine supercell was actually a 256 atom bi-layer graphene unit cell rather than a graphite surface, as shown in Figure 4.21. The 2 layers are coloured in different shades of green for clarity.

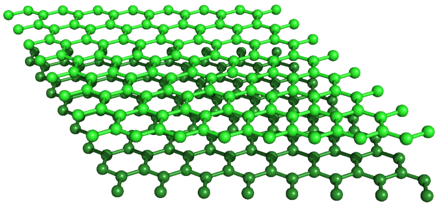

Figure 4.21: The 8x8 hexagonal bi-layer graphene super cell

Defects were introduced into the pristine supercell in the form of vacancies, adatoms or rearrangements. The vacancies studied were mono-vacancies and 1st and 3rd neighbour di-vacancies. The add-atoms studied were the grafted and the spiro interstitials. The rearrangement studied was the Stone-Wales defect, otherwise known as the 7-5 bond rotation [8]. The supercells for these were otherwise identical to the pristine supercell and the general natures of the defects are illustrated in Figure 4.22. Once again, the 2 layers are coloured in different shades of green for the sake of clarity.

The size of the unit cell was selected due to limitations imposed by the level of complexity that could be calculated practically using the then-current version of *AIMpro*. It was felt that this was justified in order to attempt to separate the surface defects as far as possible, thereby minimising periodic

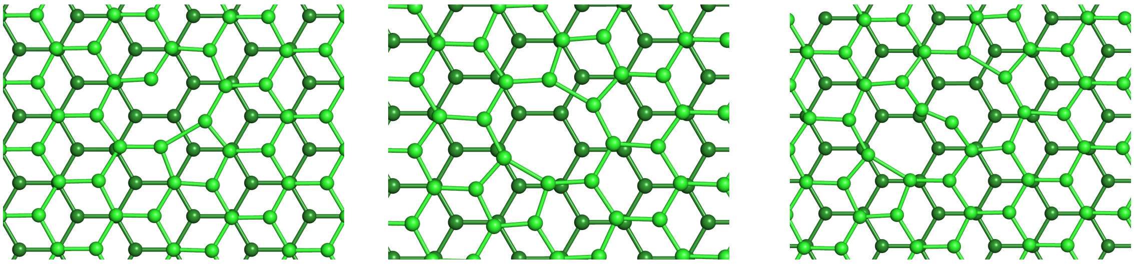

Mono-vacancy 1st neighbour di-vacancy 3rd neighbour di-vacancy

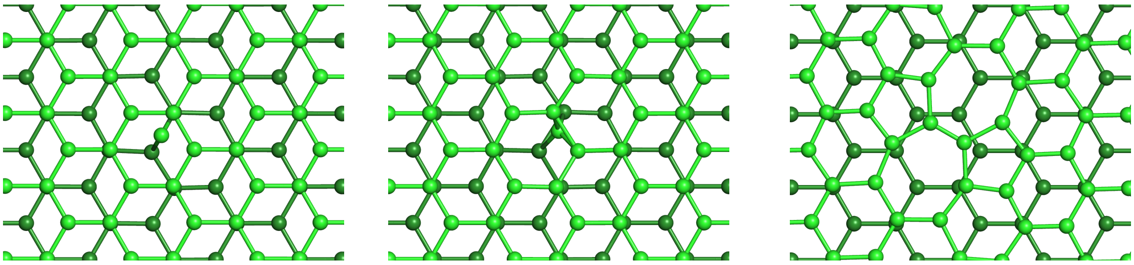

Grafted interstitial Spiro interstitial Stone-Wales defect

Figure 4.22: General form of the graphitic surface defects studied.

interactions. This strategy would seem to have been successful for at least some of the defects studied, yielding almost flat energy levels in some of the bandstructures, most noticeably in the case of the grafted interstitial, figure 4.32.

AIMpro runs were conducted under LDA using a 4-Gaussian pdpp basis set. The Brillouin zone sampling was of the 2x2x1 MP type. Removal of a carbon atom to create a D_{3h} vacancy gives rise to 3 degenerate half occupied sp^2 hybrids on the neighbours, and also withdraws a half occupied p_z orbital. There is potential Jahn Teller distortion to C_{2v} giving a triplet state or for electron transfer between σ and π systems giving a singlet [9]. Both cases were examined with AIMPRO.

Additionally, once the supercells were optimised it became clear that there were multiple possible conformations for some of the defects, a situation that is unique to the surface studies as opposed to the bulk. Both the mono-vacancy and 3rd neighbour may remain in plane or they may protrude or be indented.

$$E_F = E_d - n_d \left(\frac{E_p}{n_p} \right) \tag{4.4}$$

The formation energies of these defects were calculated according to equation 4.4, where E_d is the energy of the defected supercell, E_p is the energy of the pristine equivalent and n_d and n_p are the respective numbers of atoms in the cells. These results are listed in Table 4.1 and are in reasonable general agreement with the literature. Gulans *et al.* have calculated defect energies for the grafted and spiro interstitials at 7.09 eV and 6.59 eV respectively; Jie Ma *et al.* report a defect energy for the Stone Wales defect as 4.96 eV and Zobelli *et al.* report values of 8.25 eV for the 1st neighbour di-vacancy and 4.86 eV for the Stone-Wales defect. [10][11][12]. In all cases but one, *AIMpro*

System	no. atoms	Defect energy/eV
Pristine bi-layer graphene	256	0.00
Mono-vacancy (spin-averaged)	255	8.26
Mono-vacancy (triplet)	255	7.97
1st neighbour di-vacancy	254	7.71
3rd neighbour di-vacancy (protruding)	254	12.92
3rd neighbour di-vacancy (indented)	254	13.12
Stone-Wales defect	256	4.92
Grafted interstitial	257	7.50
Spiro interstitial	257	5.72

Table 4.1: Formation energies for common defects on bi-layer graphene

identified the systems as having no net spin and so calculations were performed spin-averaged. However, in the case of the mono-vacancy, *AIMpro* identified a magnetic moment of 1.033 μ_B and it was found that the triplet state was more energetically favourable than the singlet, agreeing with Yuchen Ma *et al.*'s calculation of a magnetic moment of 1.04 μ_B and an energy of 7.7 eV [13]. This triplet state shows an indented conformation when compared with the spin-averaged form and the singlet, both of which lie in plane. It should also be noted that all these defects are higher in energy than the pristine bi-layer graphene and thus, their production processes are endothermic. Finally, in the case of the 3rd neighbour di-vacancy, the protruding conformation is preferred over the indented.

Once the defected cells had been optimised and the preferred conformations identified, analysis runs were conducted to generate bandstructures and dump files for use in *AIMview*. The analysis path for these calculations was chosen to link the Γ point with a pair of opposite corners of the first Brillouin zone, K and K′, as well as their adjacent boundary mid points, M and M′. The actual path used was Γ-K-M-Γ-K′-M′-Γ and 60 points per path segment were used to produce the bandstructures. This ensured that the curvature of the bands was accurately represented. When generating the dump files for *AIMview*, only 6 points per path segment were specified in order to avoid producing overly large files. *AIMview* is very RAM hungry when working with large systems and, since the dump file contains a full set of wavefunctions for each point on the analysis path, experience has taught me that the fewer the points on the analysis path, the less the likelihood of taxing the computer unduly.

As with the scanning tunneling microscopy tips, only a portion of the energy levels were calculated in order to conserve computational resources. Hund's rule and the Pauli exclusion principle were used to calculate the HOMO for the system and therefore place the Fermi level. For example, the pristine model comprised of 256 atoms. Using 4 valence electrons per atom, level 512 would be equivalent to the HOMO and the bandstructure and *AIMview* dump file were calculated for levels 500-531. The exception to this methodology is in the case of the spin polarised calculation for the mono-vacancy triplet state. In this case, the two chemical potentials, as calculated by *AIMpro*, were used to define the levels of occupation for the spin-up and spin-down bandstructures. The dump files generated by *AIMpro* were used in *AIMview* to produce images of the wavefunctions representing the HOMO -1, HOMO, LUMO and LUMO +1.

This methodology was applied to the pristine and various defected supercells in order to generate their bandstructures and images of their frontier orbitals.

4.2.1 Pristine Bi-layer Graphene

Figure 4.23 shows the bandstructure close to the Fermi level for the pristine, bi-layer graphene supercell. Compared to Figure 4.7, it looks significantly more complicated because the Brillouin zone needs to be folded in order to represent the 2^3 unit cells in each of the lattice directions. Consequently, this graph is focussed on a smaller region of the energy axis and only shows the area of interest near the Fermi level. As usual, it is the "frontier orbitals" in molecular science or the bands near the Fermi level in solids that are important chemically and physically. Figure 4.24 has been plotted using the same path through the Brillouin zone as in Figure 4.7 and shows all of the filled energy levels and a

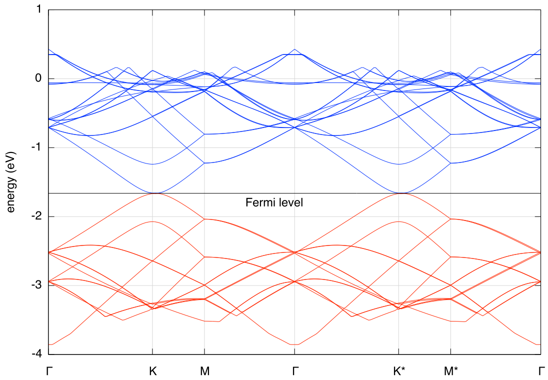

Figure 4.23: The bandstructure of pristine, bi-layer graphene, levels 500-531.
A larger version is presented in the Appendix, Figure B.6

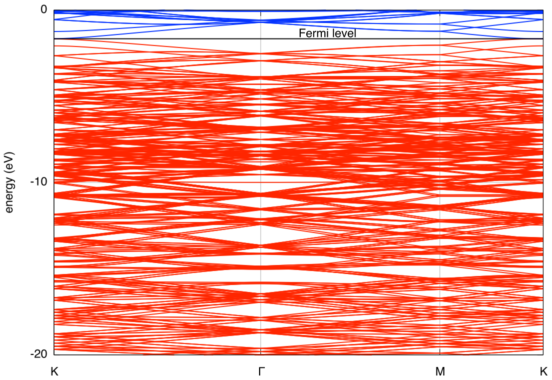

Figure 4.24: The bandstructure of pristine, bi-layer graphene, all levels up to 527. A rationale for filtering the number of levels calculated.

few of the unfilled ones. Note that it has become all but unreadable!

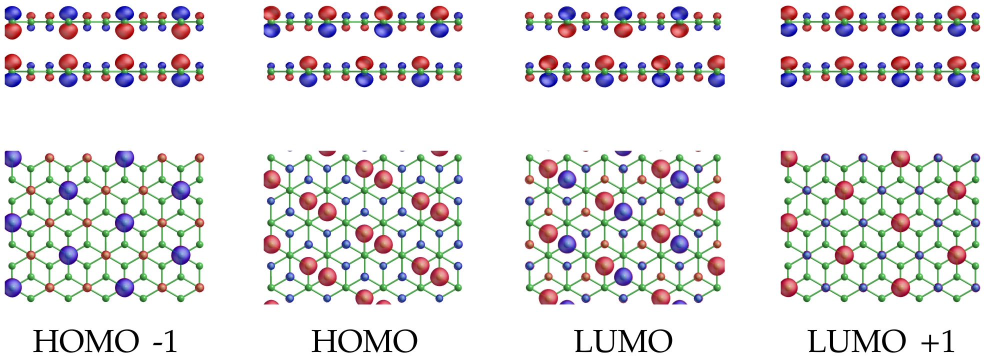

Figure 4.25: The frontier orbitals for pristine, bi-layer graphene modelled in a 256 atom supercell.
A larger version is presented in the Appendix, Figure A.15

The wavefunctions for the pristine bi-layer graphene, when modelled using this 256 atom supercell, are shown in Figure 4.25. Comparing these to the ones calculated for the primitive bi-layer graphene unit cell, as detailed in Figure 4.8, shows significant differences between the simulations of the non-bonding orbitals. However, these differences appear to arise from taking different linear combinations of the degenerate wavefunctions, such that they mix wavefunctions at the K point on the two graphenes.

4.2.2 The Mono-vacancy

Removing an atom from the lattice leaves three atoms with dangling C-C bonds. The vacancy undergoes a Jahn-Teller distortion and two of these bonds reconstruct, forming a 9-5 structure with the third atom protruding from the surface.

The mono-vacancy differs from the other defects studied here, in that it is the only structure whose lowest energy structure is spin polarised. The bandstructures are presented in Figure 4.26. It is evident that the vacancy has disrupted the graphitic nature of the bandstructure, opening a small band gap at the K point. The Fermi level is higher on the spin-up bandstructure because

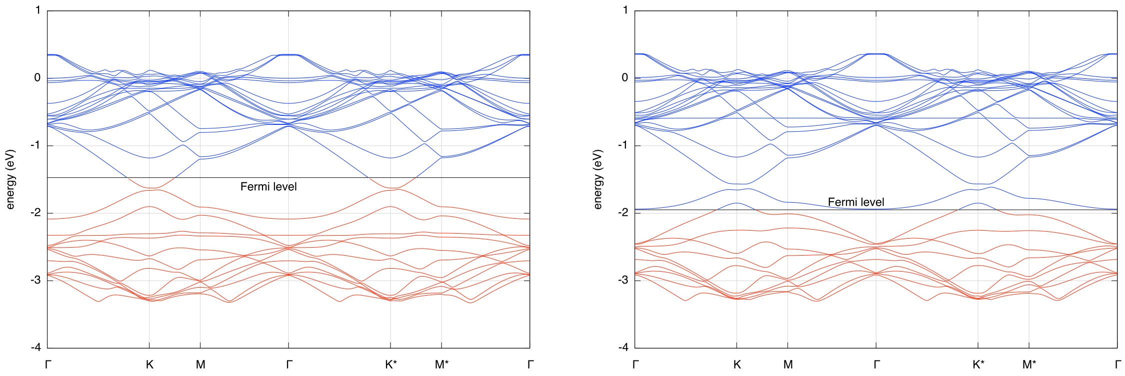

Spin-Up
Spin-down

Figure 4.26: The bandstructures for the spin-polarised mono-vacancy in bi-layer graphene, levels 500-529.
Larger versions are presented in the Appendix, Figures B.7 and B.8

two additional levels contain a spin-up electron, 510 and 511, compared to the spin-down bandstructure. Another result of this is that these two singly occupied bands separate the HOMO and LUMO. The orbitals are illustrated in Figure 4.27. What is represented here seems somewhat counter intuitive.

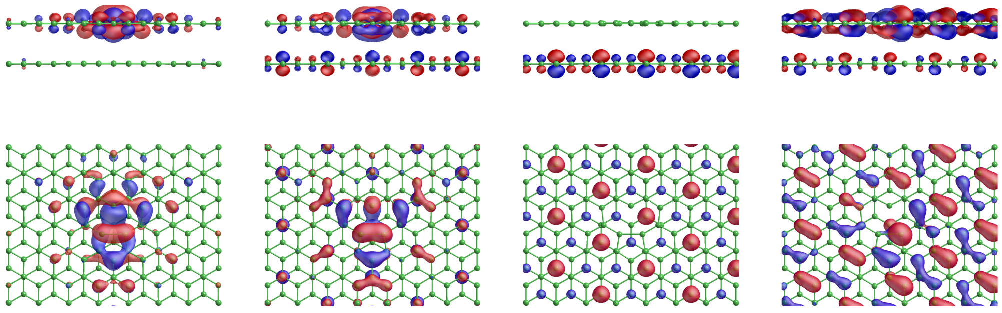

HOMO
SOMO
SOMO
LUMO

Figure 4.27: The frontier orbitals for the spin-polarised mono-vacancy in bi-layer graphene.
A larger version is presented in the Appendix, Figure A.16

When an atom is removed from the surface, electron density actually increases around the vacancy.

4.2.3 The 1st Neighbour Di-vacancy

When two neighbouring atoms are removed four carbon atoms are left with dangling bonds. These reconstruct to form a 5-8-5 structure. The bandstructure is presented in Figure 4.28. Even more disruption of the electronic structure is evident here, with a larger band gap opening at the K point and the LUMO losing dispersion. The LUMO is relatively flat, indicating a marked lack of dispersion (and thus a localised state) but there is still some evidence of interaction with neighbouring cells. The orbitals are illustrated in Figure 4.29.

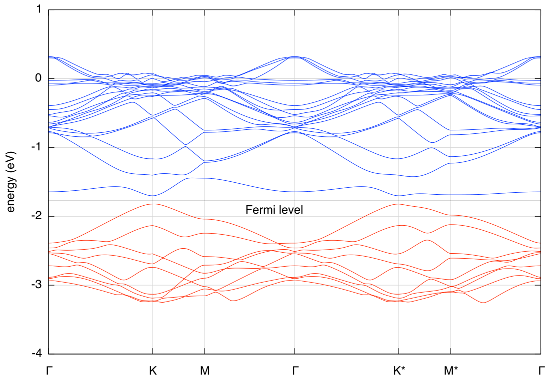

Figure 4.28: The bandstructure for the 1st neighbour di-vacancy in bi-layer graphene, levels 500-527.
A larger version is presented in the Appendix, Figure B.9

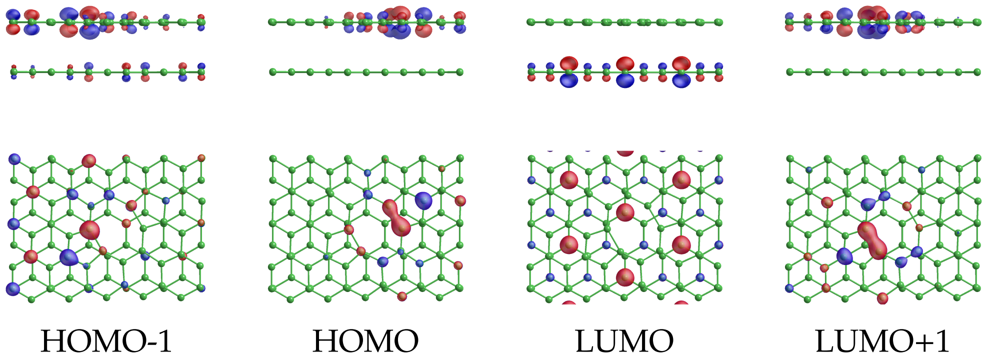
HOMO-1 HOMO LUMO LUMO+1

Figure 4.29: The frontier orbitals for the 1st neighbour di-vacancy in bi-layer graphene.
A larger version is presented in the Appendix, Figure A.17

4.2.4 The 3rd Neighbour Di-vacancy

With the 3rd neighbour di-vacancy we see once again the familiar reconstruction to a pentagon-shaped structure. This time there is a 5-9-9-5 pattern remaining and the central bond of the chain of carbon atoms separating the two halves is a triple bond. The bandstructure is presented in Figure 4.30. Once again, more disruption of the electronic structure is occurring, with an even larger gap in evidence at the K point and the HOMO and LUMO bands becoming flattened. The orbitals are illustrated in Figure 4.31.

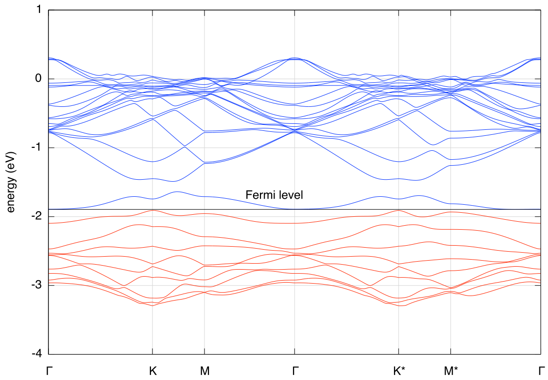

Figure 4.30: The bandstructure for the 3rd neighbour protruding di-vacancy in bi-layer graphene, levels 500-527. A larger version is presented in the Appendix, Figure B.10

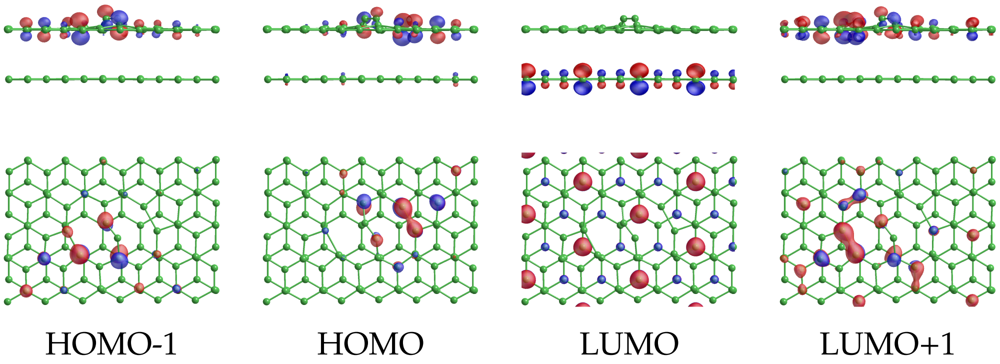

Figure 4.31: The frontier orbitals for the 3rd neighbour protruding di-vacancy in bi-layer graphene.
A larger version is presented in the Appendix, Figure A.18

4.2.5 The Grafted Interstitial

The bandstructure is presented in Figure 4.32. As well as opening up a gap at the K point, the interstitial atom appears to have introduced a fairly flat energy band as the LUMO, just above the Fermi level. The near flatness of this band would indicate that there is virtually no interaction between neighbouring unit cells and that the state is very localised. It is curious that this is not the p orbital on the grafted atom perpendicular to its triangle of bonds, which gives rise to the HOMO and LUMO+1. It is rather p orbital on that atom, within the plane of the triangle. This system also shows some splitting of the bands

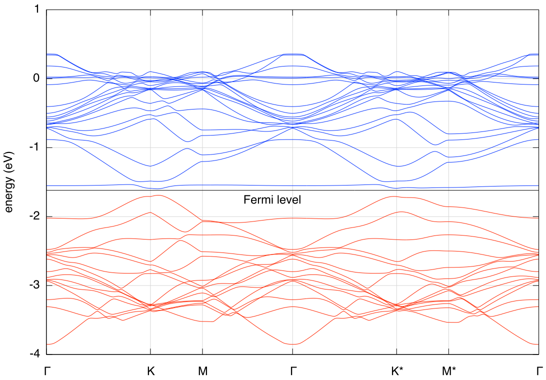

Figure 4.32: The bandstructure for the grafted interstitial in bi-layer graphene, levels 500-533.
A larger version is presented in the Appendix, Figure B.11

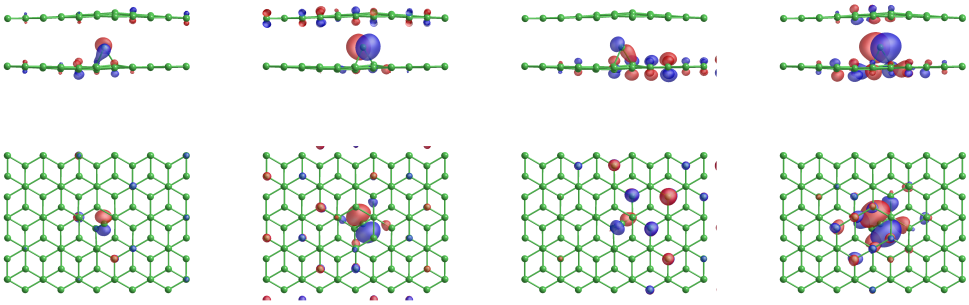

HOMO-1 HOMO LUMO LUMO+1

Figure 4.33: The frontier orbitals for the grafted interstitial in bi-layer graphene.
A larger version is presented in the Appendix, Figure A.19

at the M and M* points and at Γ. The splitting is much more pronounced at the M* point. The orbitals are illustrated in Figure 4.33. Electron density appears to be concentrated quite strongly around the interstitial atom and its neighbours in the layer it's grafted onto.

4.2.6 The Spiro-bonded Interstitial

The bandstructure is presented in Figure 4.34. The disruption caused by the spiro-bonded interstitial atom is very different from that caused by the grafted interstitial. In this case, the disruption is all happening away from the Fermi

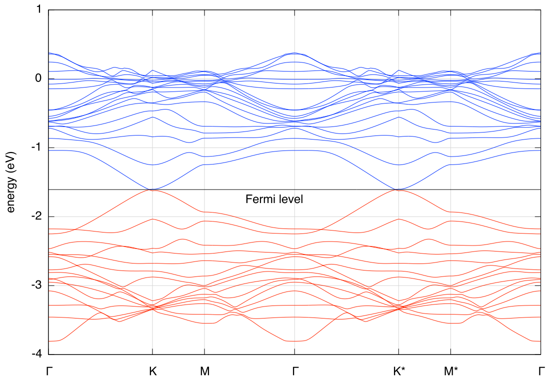

Figure 4.34: The bandstructure for the spiro-bonded interstitial in bi-layer graphene, levels 500-533.
A larger version is presented in the Appendix, Figure B.12

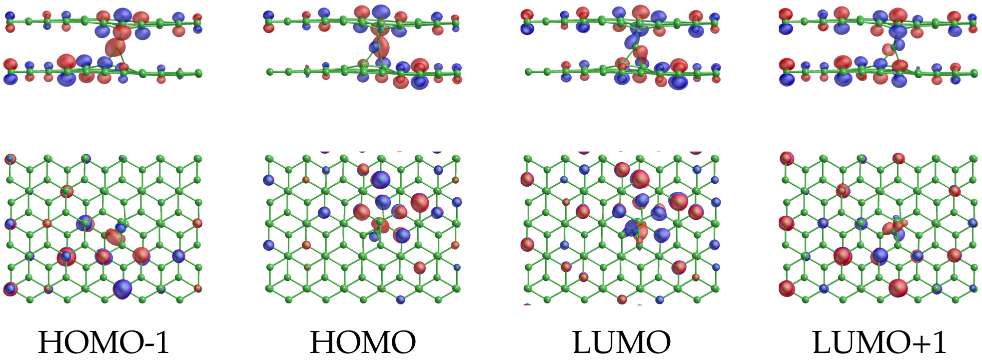
HOMO-1 HOMO LUMO LUMO+1

Figure 4.35: The frontier orbitals for the spiro-bonded interstitial in bi-layer graphene.
A larger version is presented in the Appendix, Figure A.20

level, leaving the area at the K point looking comparatively graphitic in nature. Away from the K point, at the M point and at Γ, the bands are splitting even more than in the case of the grafted interstitial. The orbitals are illustrated in Figure 4.35. As is the case with the grafted interstitial, electron density appears to be concentrated quite strongly around the interstitial atom and its neighbours.

4.2.7 The Stone-Wales Defect

The Stone-Wales defect is the result of a bond rotation and is characterised by a 5-7-7-5 structure. The bandstructure is presented in Figure 4.36. In this case, the main effect of the defect is to lower the energy of the LUMO, introducing a flat band running from the M and M* points to Γ. Also, in comparison to the pristine bi-layer graphene, some band splitting is observed, with more in evidence at the M* point. The orbitals are illustrated in Figure 4.37. With the obvious exception of the defect itself, the orbitals bear much resemblance to those of pristine bi-layer graphene. The bonding and anti-bonding orbitals are reasonably well defined and located on the α sublattice. Likewise, the two non-bonding orbitals are sited on the β sublattices for their respective layers. This is curious in light of the way that the orbitals arranged themselves in the

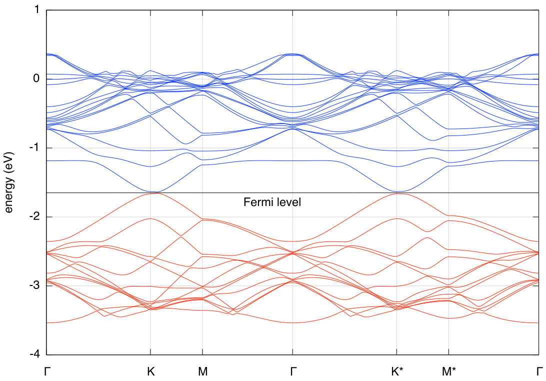

Figure 4.36: The bandstructure for the Stone-Wales defect in bi-layer graphene, levels 500-531.
A larger version is presented in the Appendix, Figure B.13

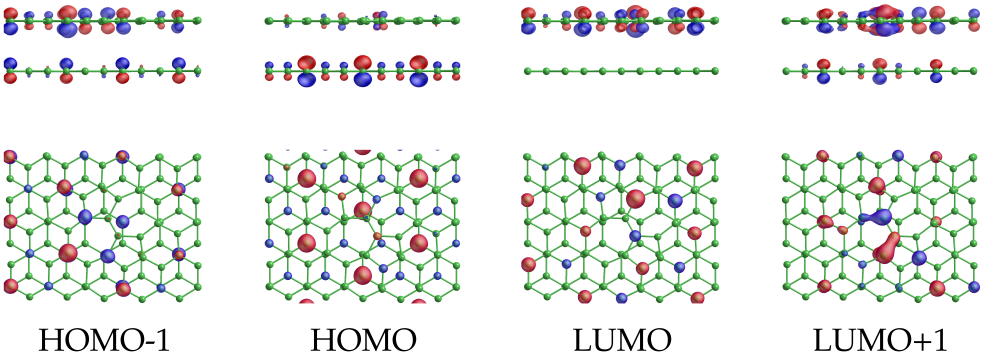

Figure 4.37: The frontier orbitals for the Stone-Wales defect in bi-layer graphene.
A larger version is presented in the Appendix, Figure A.21

pristine 256 atom supercell, Figure 4.25.

4.3 Simulating Scanning Tunneling Micrographs

It is possible to produce exact simulations of STM images computationally but the process is very intensive. Amara *et al* have produced images of graphene and some common defects using a tight-binding approach [14]. The purpose of this project was to develop a more "stripped-down" process so that a relatively quick method could be utilised. The principle of operation of an STM is described in Chapter 3. In order to produce realistic simulations of scanning tunneling micrographs, there are two important concepts to bear in mind. The first is the Tersoff-Hamann approximation, as described in equation 2.3. This means that the tunneling current can be assumed to depend on the squares of the wavefunctions for the surface atoms for energy levels at or near the Fermi level. Secondly, biasing the sample with a positive potential in relation to the tip effectively lowers the Fermi level of the sample under examination. So, a method of predicting the appearance of constant height scanning tunneling micrographs can be devised by noting the effects of a lowered Fermi level on the bandstructure of the sample surface and then simply plotting a cross-section of the corresponding squares of the wavefunctions.

4.3.1 Generalised Method

Taking the pristine model as an example, examination of a portion of the bandstructure generated by the primitive unit cell, as shown in Figure 4.38, reveals that, for a small positive surface bias, the Fermi level is lowered slightly and the orbital that is being tunnelled into is the HOMO-1 orbital at the K point, marked "a" on the bandstructure. For a slightly larger positive bias, the Fermi level is lowered a little more and the same orbitals at the M point, marked "b" on the bandstructure , are available for tunneling. For an even larger positive bias, the Fermi level is lowered even further and a combination of four nearly degenerate orbitals at the Γ point, marked "c" on

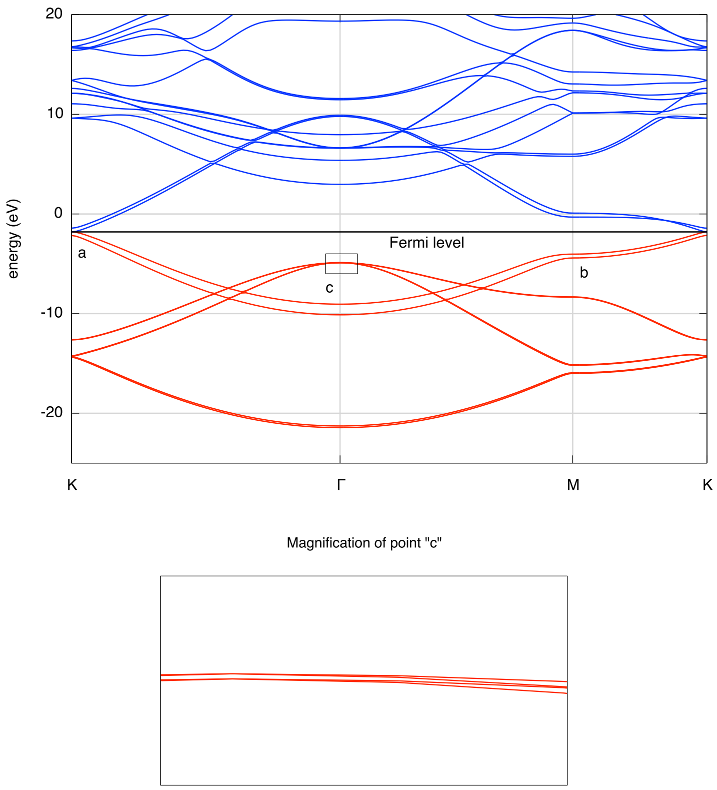

Figure 4.38: A portion of the bandstructure for the pristine bi-layer graphene unit cell.
Note that the magnification of area "c" reveals four energy levels that are either degenerate or very nearly so.

the bandstructure and also shown magnified, become available for tunneling.

Once the orbitals of interest and their position within the Brillouin zone had been identified, they were visualised in *AIMview* using dump files generated in the 256 atom supercell analysis runs. Cross-sections were then produced at heights of 0.8 Å and 1.6 Å and colour-mapped in the manner of traditional scanning tunneling microscopy images. The stages of this method are illustrated in Figure 4.39

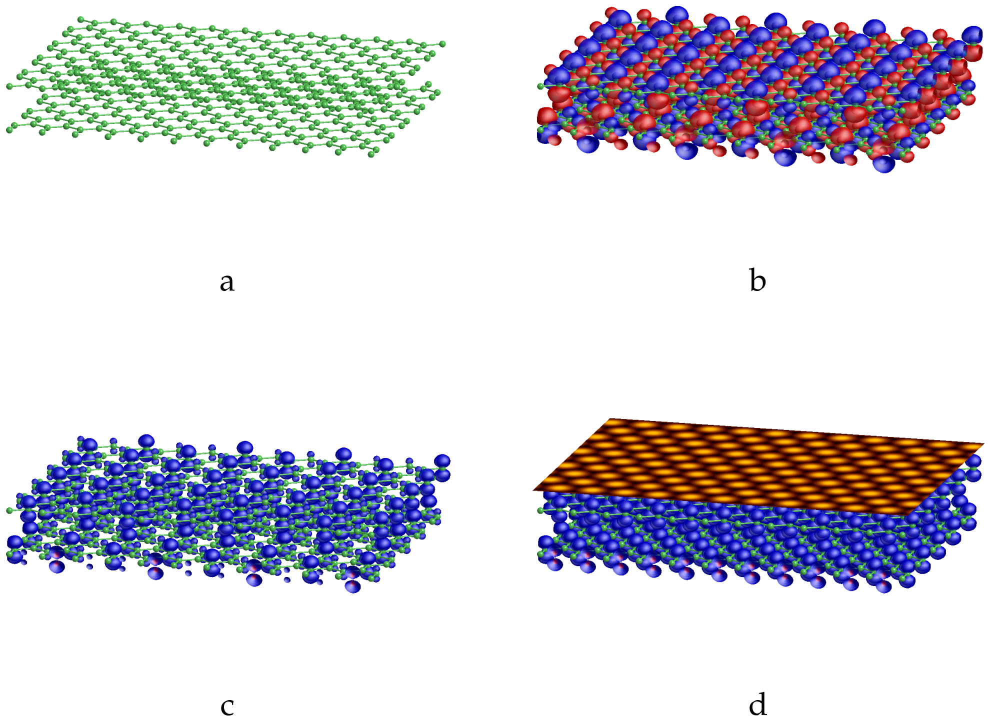

Figure 4.39: The general method of producing a simulated scanning tunneling micrograph.
a. Select the area of interest. b. Select the required wavefunction. c. Plot the mod^2 of the wavefunction. d. Produce a colour-mapped cross-section at the required height.

4.3.2 Pristine Bi-layer Graphene

The orbitals and the scanning tunneling micrographs that were derived from them are illustrated in Figure 4.40. The low surface bias images show a hexagonal array of roughly circular patches of high electron density. These are located over the α atoms. In the medium bias image, the areas of electron density show a more elongated aspect, with electron density shared between the α atoms and the top-layer β atoms. There is slightly more density over the α sites. Neither show much significant change in appearance over height but they both compare favourably with real images of experimental results, such as images a and b in Figure 4.41.

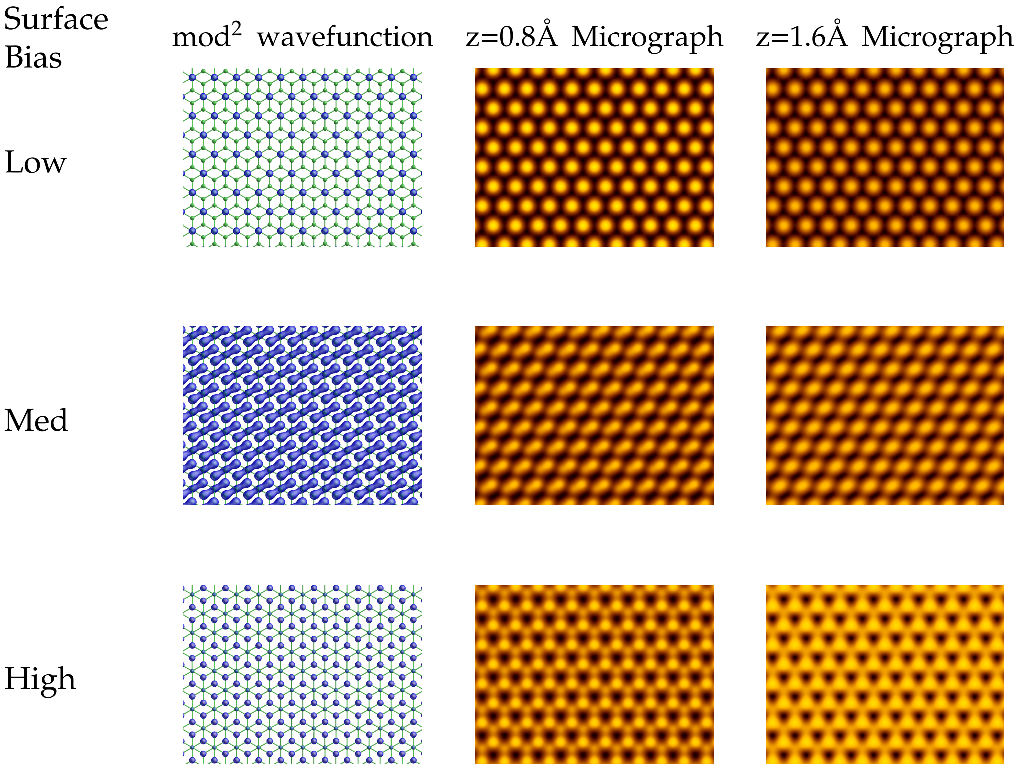

Figure 4.40: The mod^2 orbitals for positive-surface biased pristine bi-layer graphene and the simulated scanning tunneling micrographs that were generated from them. Larger images of the micrographs are presented in the Appendix, Figure C.1

The high bias images are even more interesting. There is more detail

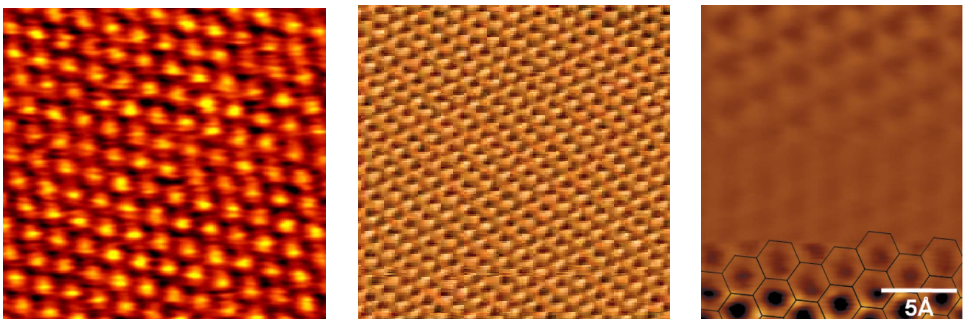

a b c

Figure 4.41: Examples of graphite surface scanning tunneling micrographs. a: Rounded aspect [15]. b: Rectangular aspect [16]. c: Hexagonal transforming to triangular aspect as tip is retracted [17].

being resolved at the lower tip-height, even to the extent of showing areas of different electron density corresponding to atoms in different environments. The β atoms have significantly more electron density than the α sites. At the higher tip height, the orbitals of the β sites completely dominate the image and take on a triangular aspect. This corresponds very well to experimental observations by Cisternas et al., as detailed in image c of Figure 4.41 [17]. This image is the result of retracting the STM tip by 1.0 Å during a run. In the lower portion of the image, where the tip is closest to the surface, a hexagonal pattern with areas of two distinct brightnesses corresponding to the α and β is evident. Once the tip has been retracted, in the upper portion of the image, the triangular aspect is plain to see.

The scanning tunneling micrograph simulations for the surface defects were all produced using this general method. The low bias image was generated using the the orbital just below the Fermi level at the K point. The medium bias image was produced from a combination of the two degenerate (or nearly degenerate) orbitals below the Fermi level at the M point. The high bias image was produced from the cluster of degenerate (or nearly degenerate) orbitals at the Γ point. Where it has been impractical to use this method, the specific reason has been explained in the description.

4.3.3 The Mono-vacancy

The mono-vacancy, as noted before, is spin polarised with two unpaired spin-up electrons. Referring to Figures 4.26 and 4.27, it can be seen that the orbital that is close to the Fermi level has all its electron density on the lower layer. Consequently, this method is not applicable and no images were produced for the low bias conformation. The medium and high bias images are presented in Figure 4.42.

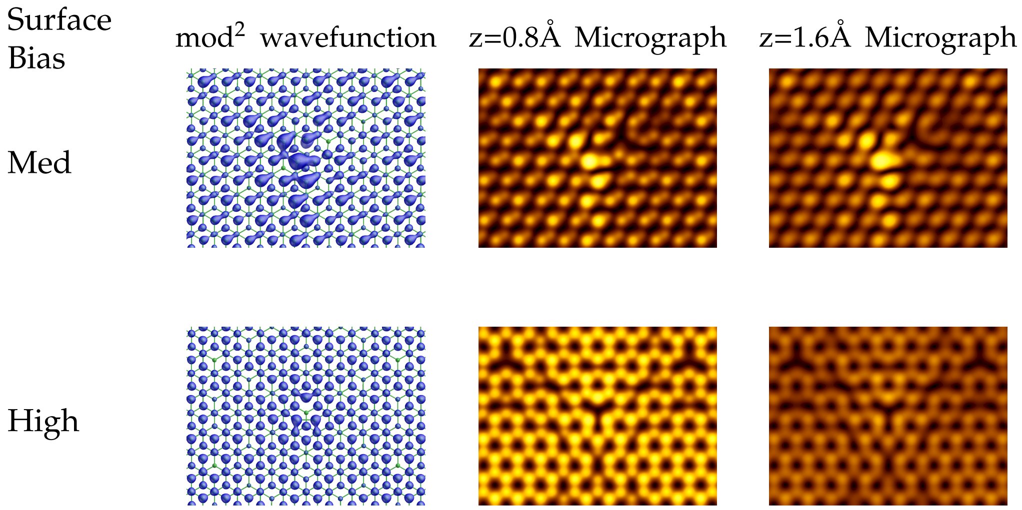

Figure 4.42: The mod^2 orbitals for positive-surface biased mono-vacancy in bi-layer graphene and the simulated scanning tunneling micrographs that were generated from them.
Larger images of the micrographs are presented in the Appendix, Figure C.2

The overall patterns for the surface surrounding the defects comprise the same general shapes evident in the pristine surface. Looking at the high-bias STM simulations, there appear to be some interesting symmetry effects occurring away from the image centre. Specifically, regarding the electron density, there appear to be mirror planes located two lattice parameters out, orthogonal to three axes at 120° intervals. There is a possibility that these could be artefacts introduced by the choice of supercell lattice parameters, 8 being 2^3, and so this simulation should be treated with some caution until simulations comprising larger supercells can be computed practically.

4.3.4 The 1st Neighbour Di-vacancy

The orbitals and the scanning tunneling micrographs for the 1st neighbour di-vacancy are illustrated in Figure 4.43.

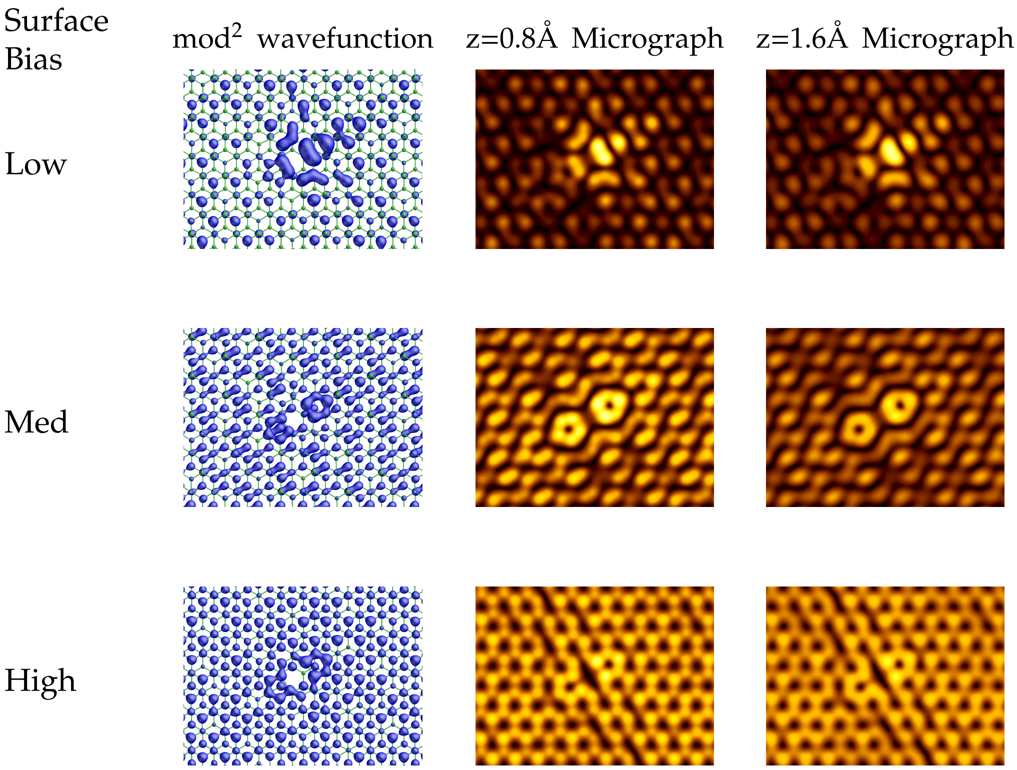

Figure 4.43: The mod^2 orbitals for positive-surface biased 1st neighbour di-vacancy in bi-layer graphene and the simulated scanning tunneling micrographs that were generated from them.
Larger images of the micrographs are presented in the Appendix, Figure C.3

As with the mono-vacancy, the overall patterns for the surface surrounding the defects comprise the same general shapes evident in the pristine surface. In all three simulations, it is evident that the charge density is concentrated in the region of the defect structure and, in the medium and high bias images, most noticeably around the 5-membered rings. The high biassed micrograph appears to show evidence of a very directional disruption to the π system perpendicular to the axis of the 5-8-5 reconstruction. Again, like the mono-vacancy, there is a possibility that this may be an artefact of the unit cell chosen and further investigations using considerably larger unit cells would be desirable, once the resources are available.

4.3.5 The 3rd Neighbour Di-vacancy

The bandstructure, as seen in Figure 4.30 is so disrupted near the Fermi level, that no obvious point in the Brillouin zone could be selected for the medium bias micrograph simulation. The orbitals and the scanning tunneling micrographs for the high bias 3rd neighbour di-vacancy are illustrated in Figure 4.44.

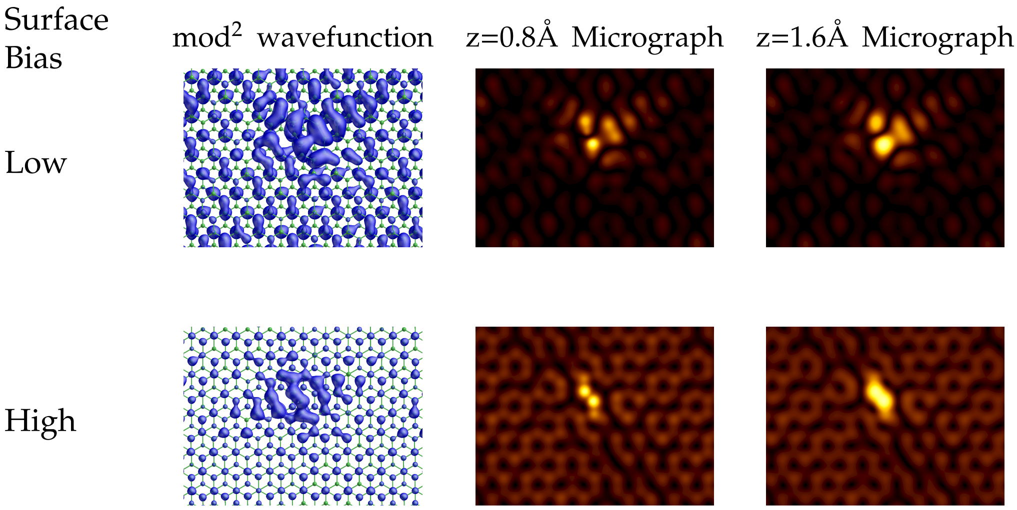

Figure 4.44: The mod^2 orbitals for the positive-surface biased 3rd neighbour di-vacancy in bi-layer graphene and the simulated scanning tunneling micrographs that were generated from them.
Larger images of the micrographs are presented in the Appendix, Figure C.4

These images are particularly poor simulations. The mod^2 wavefunction reveals that most of the electron density is concentrated at the defect but the protruding carbon pair, being much closer to the sampling plane, dominates both the simulations significantly. This demonstrates a major weakness of this method of generating constant height images, in that it is only really suitable for planar systems, or those that are close enough that they may be treated as such.

4.3.6 The Grafted Interstitial

The orbitals and the scanning tunneling micrographs for the grafted interstitial are illustrated in Figure 4.45. Compared to the other simulations, this set of

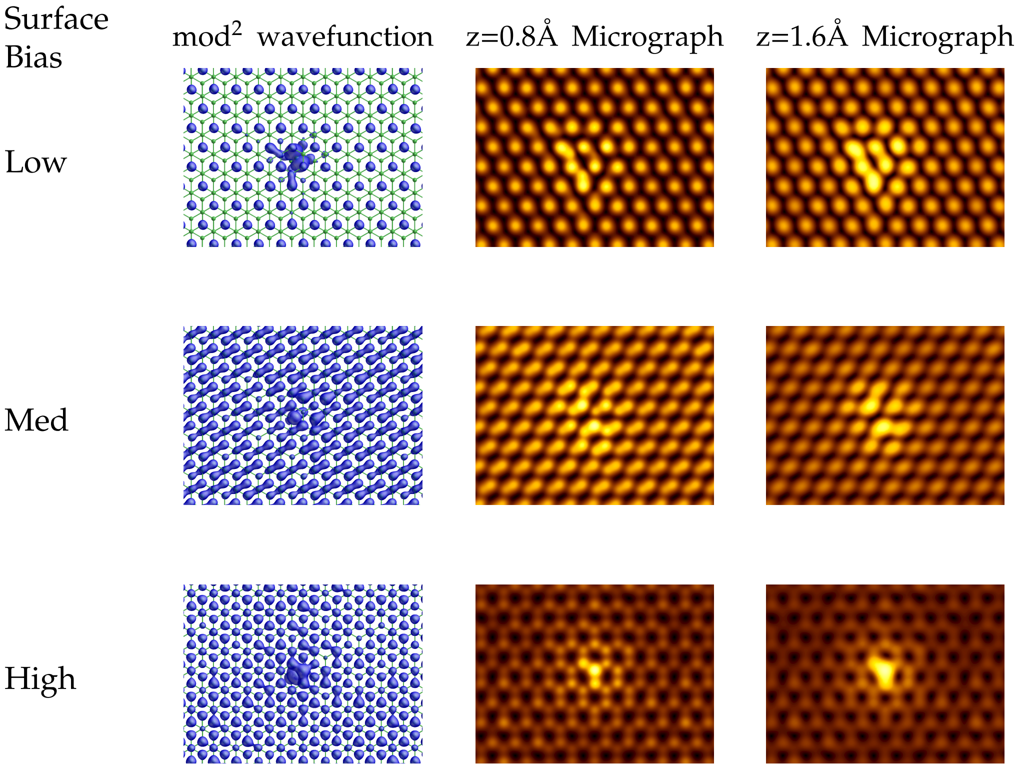

Figure 4.45: The mod^2 orbitals for positive-surface biased grafted interstitial in bi-layer graphene and the simulated scanning tunneling micrographs that were generated from them.
Larger images of the micrographs are presented in the Appendix, Figure C.5

micrographs bears the most resemblance to those of the pristine surface. The defect's presence is revealed by distinctive brightening of the images localised to its vicinity, but the overall geometric basis of the images is virtually unchanged. There would not appear to be much in the way of long range disruption occurring here and this was anticipated because of the presence of the flat, non-interacting energy level in the bandstructure, Figure 4.32.

4.3.7 The Spiro Interstitial

The orbitals and the scanning tunneling micrographs for the spiro interstitial are illustrated in Figure 4.46. This image's appearance is typified by a darkness

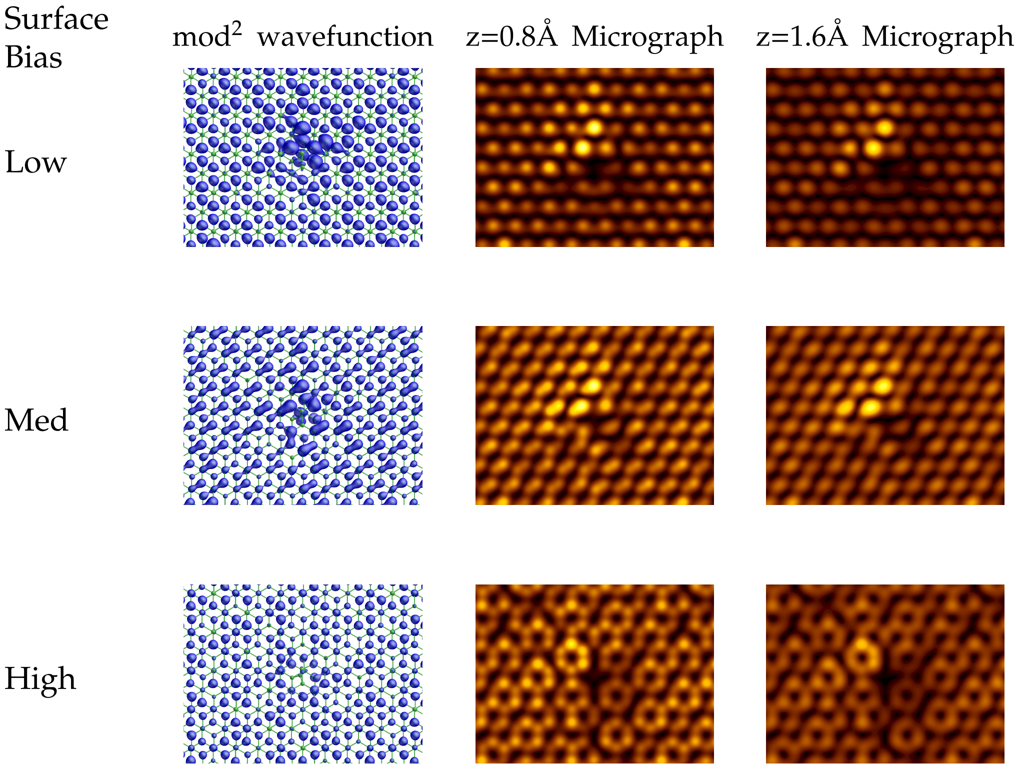

Figure 4.46: The mod^2 orbitals for positive-surface biased spiro-bonded interstitial in bi-layer graphene and the simulated scanning tunneling micrographs that were generated from them.
Larger images of the micrographs are presented in the Appendix, Figure C.6

at the defect's location with a bright region of high electron density localised to one side and a dim region to the other, breaking the symmetry of the surface. The geometric basis of the medium bias image has been altered at the core of the defect, with a portion losing its rectangular shape and forming an open-ended hexagon. The high bias image also shows significant disruption to the symmetry of the electron density at the surface.

4.3.8 The Stone-Wales Defect

The orbitals and the scanning tunneling micrographs for the Stone-Wales defect are illustrated in Figure 4.47. The rotated bond that characterises this defect

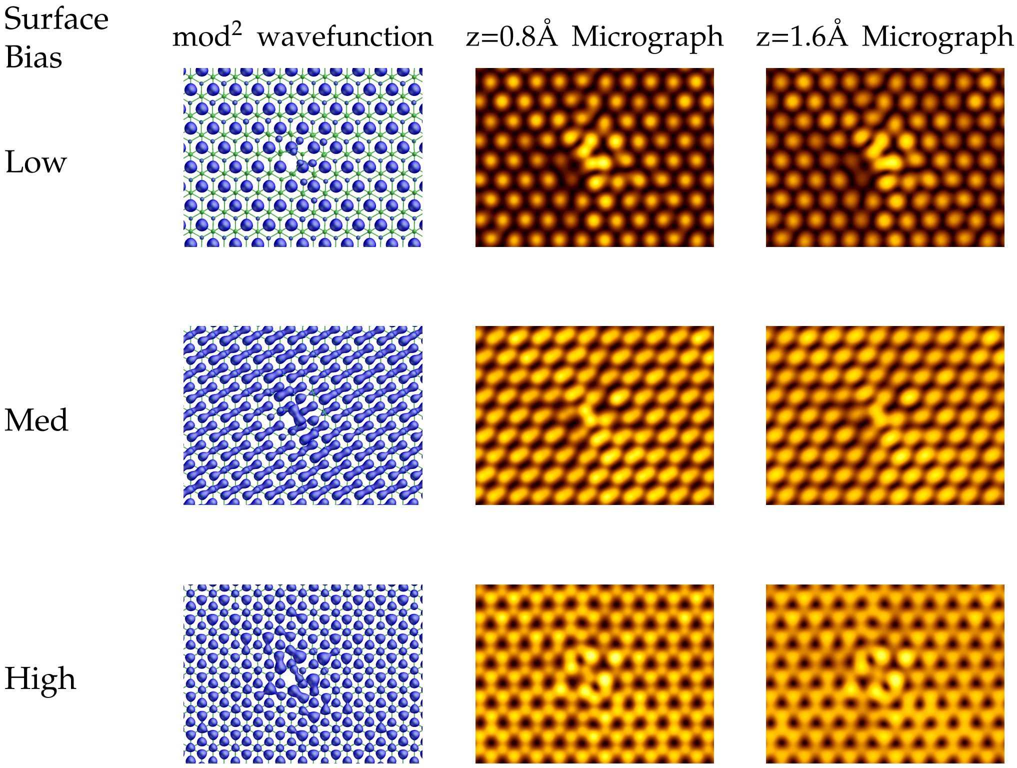

Figure 4.47: The mod^2 orbitals for positive-surface biased Stone-Wales defect in bi-layer graphene and the simulated scanning tunneling micrographs that were generated from them.
Larger images of the micrographs are presented in the Appendix, Figure C.7

is clearly visible in all simulated images. The low bias images show clear evidence of the electron density accumulating to one side of the rotated bond and both the surface's three fold symmetry and the two fold symmetry of the defect itself are broken. The medium and high bias simulations also show this but to a lesser extent, with the high bias image showing a similar electronic structure to the defect's physical conformation.

4.3.9 Summary

The simulation of STM images using this methodology has been a success. Where comparisons with experimental data have been possible, these have shown that my simulations are in agreement with the experimental results. Unfortunately, less comparisons than would be ideal are possible for a number of reasons. My investigations were conducted on bi-layer graphene, whereas much of the work on graphene defects, experimental and theoretical, has been conducted on single graphene layers [18]. The interactions between the two layers in my research adds extra complications to the system that aren't present with a single layer and so direct comparisons are likely to be misleading. Researchers in the field have noted the different symmetry between mono and multi-layer graphene [19]. The same paper also notes the inherent stability and very low defect concentrations in graphene and this may also contribute to the relative lack of experimental data.

As with much of my research, this field would benefit from the use of the latest version of the *AIMpro* code, so that systems with significantly larger surfaces and more layers could be modelled.

4.4 References

[1] Mark Winter. WebElements Periodic Table of the Elements, 2008.

[2] Florent Tournus, Jean-Christophe Charlier, and Patrice Mélinon. Mutual orientation of two C60 molecules: An ab initio study. *The Journal of Chemical Physics*, 122:094315, 2005.

[3] Nicolas Mounet and Nicola Marzari. First-principles determination of the structural, vibrational and thermodynamic properties of diamond, graphite, and derivatives. *Physical Review B*, 71:205214, 2005.

[4] KS Novoselov, AK Geim, SV Morozov, D Jiang, Y Zhang, SV Dubonos, IV Grigorieva, and AA Firsov. Electric field effect in atomically thin carbon films. *Science*, 306(5696):666–669, 2004.

[5] A K GEIM and K S Novoselov. The rise of graphene. *Nature Materials*, 6:183–191, 2007.

[6] K S Novoselov, A K GEIM, S V Morozov, D Jiang, M I Katsnelson, I V Grigorieva, S V Dubonos, and A A Firsov. Two-dimensional gas of massless Dirac fermions in graphene. *Nature*, 438(7065):197–200, 2005.

[7] John N Murrell, Sidney F A Kettle, and John M Tedder. *The Chemical Bond*. John Wiley & Sons, 2nd edition, 1987.

[8] A J Stone and D J Wales. Theoretical Studies of Icosahedral C60 and Some Related Species. *Chemical Physics Letters*, 128(5,6):501–503, 1986.

[9] A El-Barbary, R Telling, C Ewels, MI Heggie, and et al. Structure and energetics of the vacancy in graphite. *Physical Review B*, 68:144107, 2003.

[10] Andris Gulans, Arkady V Krasheninnikov, Martti J Puska, and Risto M Nieminen. Bound and free self-interstitial defects in graphite and bilayer graphene: A computational study. *Physical Review B*, 84(2):024114, 2011.

[11] Jie Ma, Dario Alfè, Angelos Michaelides, and Enge Wang. Stone-Wales defects in graphene and other planar sp2-bonded materials. *Physical Review B*, 80(3):033407, 2009.

[12] Alberto Zobelli, Viktoria Ivanovskaya, Philipp Wagner, Irene Suarez-Martinez, Abu Yaya, and Chris P Ewels. A comparative study of density functional and density functional tight binding calculations of defects in graphene. *Physica Status Solidi B*, pages n/a–n/a, 2011.

[13] Yuchen Ma, P O Lehtinen, A S Foster, and R M Nieminen. Magnetic properties of vacancies in graphene and single-walled carbon nanotubes. *New J Phys*, 6(68), 2004.

[14] H Amara, Sylvain Latil, V Meunier, Ph Lambin, and J-C Charlier. Scanning tunneling microscopy fingerprints of point defects in graphene: A theoretical prediction. *Physical Review B*, 76(11):115423, 2007.

[15] Webmaster. Camp Nanotech. (http://411.fit.edu/campnanotech), 2008.

[16] Webmaster. Haverford course materials. (http://www.haverford.edu/physics/), 2008.

[17] E Cisternas, F Stavale, M Flores, C A Achete, and P Vargas. First-principles calculation and scanning tunneling microscopy study of highly oriented pyrolytic graphite (0001). *Physical Review B*, 79(20):205431, 2009.

[18] Eric Cockayne. Graphing and Grafting Graphene: Classifying Finite Topological Defects. *arXiv.org*, cond-mat.mtrl-sci:1106.6273v2, 2011.

[19] Elena Stolyarova, Kwang Taeg Rim, Sunmin Ryu, Janina Maultzsch, Philip Kim, Louis E Brus, Tony F Heinz, Mark S Hybertsen, and George W Flynn. High-resolution scanning tunneling microscopy imaging of mesoscopic graphene sheets on an insulating surface. *Proceedings of the National Academy of Sciences of the USA*, 104(22):9209–9212, 2007.

Chapter 5

Self Assembly

5.1 Tetracene on Copper

I was asked by Dr. Qiao Chen to investigate the adsorption of a monolayer of tetracene onto an oxygen terminated Copper (110) surface using DFT. He had noticed an interesting phenomenon occurring within a STM, whereby the adsorbate seemed to be rendered transparent under certain conditions [1]. Figure 5.1 shows the result of increasing the tunneling current from 1 nA

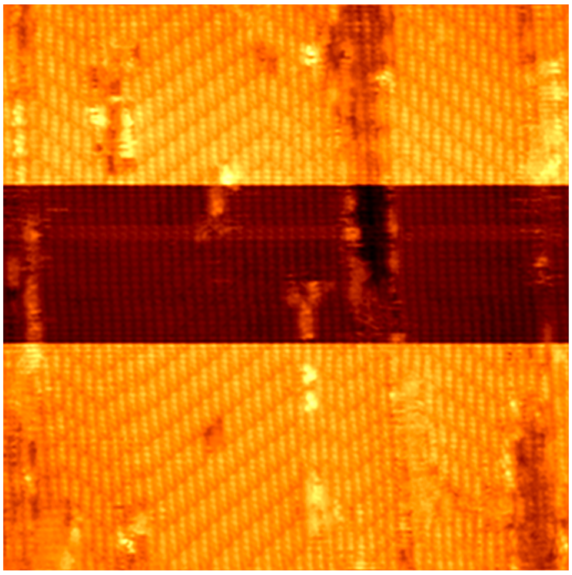

Figure 5.1: An experimental STM image of a tetracene monolayer on the oxygen terminated, reconstructed row Copper (110) surface, with the tunneling current varied from 1 nA to 50 nA and back to 1 nA.

(bright) to 50 nA (dark) and back again during a single STM scan. The two bright sections of the micrograph show the tetracene monolayer while the dark, central portion shows the underlying surface. It was suggested that it would be beneficial to build a theoretical simulation in order to understand this phenomenon.

A quick, proof of concept simulation of a single tetracene molecule on a copper surface with a layer of oxygen atoms was built and run in Cerius^2. One of the advantages offered by the speed at which a graphically based MM package is able to run is that one is able to observe the paths that the various components take on their way to the minimum energy configuration. In this case, it appeared that the tetracene behaved in a similar manner to some buoyant object, held just below the surface of a liquid and then released. The molecule did not adopt any specific conformation in relation to the surface as suggested by the experimental observation. This simulation was repeated with the tetracene molecule starting from a different initial position and the tetracene behaved in a similar manner, finishing in a different, but still unexpected, position. A third attempt yielded similar, unpredictable results. The resulting structures are shown in figure 5.2.

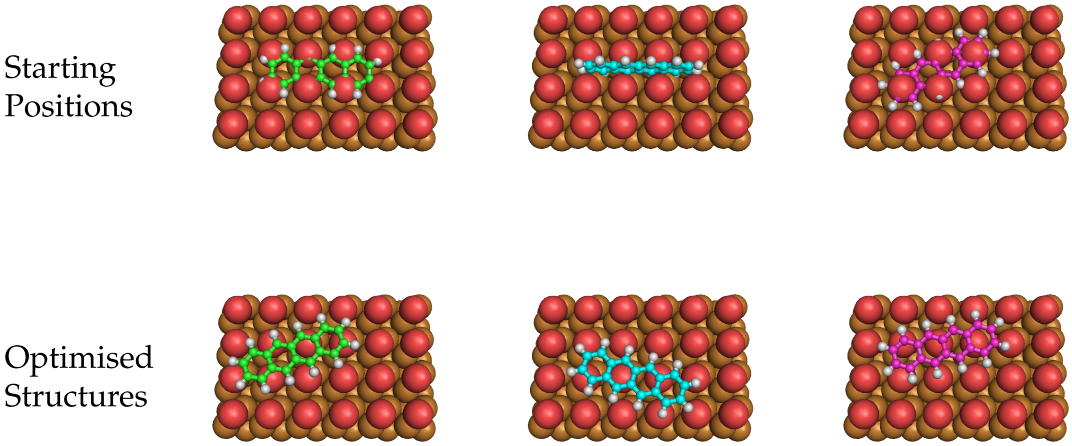

Figure 5.2: Structures from initial Cerius^2 investigation.

This illustrates one of the primary drawbacks of MM, namely that any interatomic interactions being studied need to be specifically defined and parametised in order to be modelled. DFT improves on this significantly as, by its nature, it calculates the interactions that arise from the electron density implicitly. It was concluded that a more detailed, DFT based study would be necessary to produce trustworthy results.

Two further points were also apparent from this initial study. Firstly, the surface that had been modelled was the (100) plane and not the (110) plane that was required and secondly, that the repeating supercell required to reproduce the observed mono-layer structure would need to be constructed, using non-orthorhombic lattice vectors.

5.1.1 The Reconstructed, Oxygen-Terminated Surface

Different models of the same basic surface were used in order to model different degrees of tetracene saturation. All the models were built to a depth of four partial copper layers plus the reconstructed row. For an example of this construction, see Figure 5.5. This model was constructed from 4 x 1 unit cells and the vectors were chosen to satisfy the structures that had been observed experimentally. It was employed initially in the absence of any tetracene coverage in order to test methodology and later used to model the saturated monolayer condition.

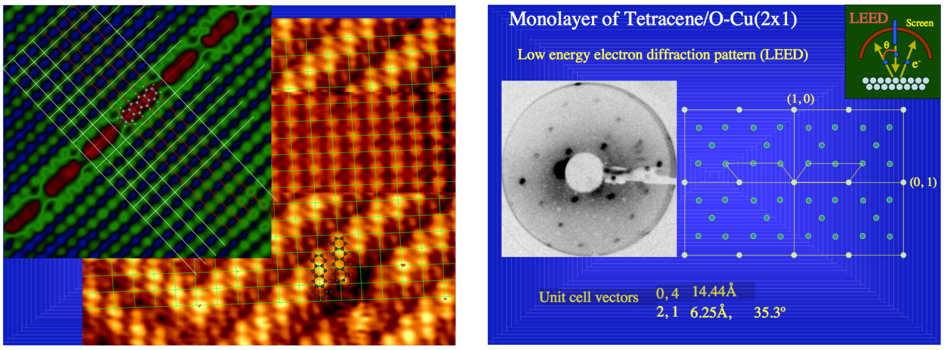

Figure 5.3: STM and low energy electron diffraction analysis used to model the system.[1]

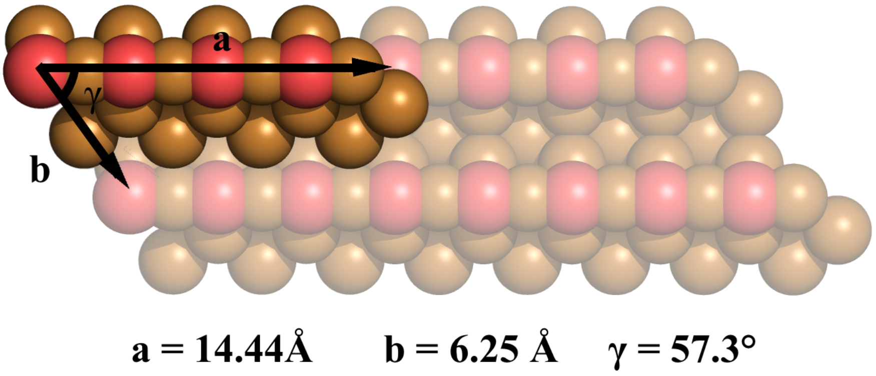

Figure 5.4: The repeating surface supercell

A plan view of this model is illustrated in Figure 5.4, along with the lattice vectors that had been extracted from the analysis of scanning tunneling micrographs and low energy electron diffraction patterns as illustrated in Figure 5.3 Effectively, the repeating supercell was offset by one primitive cell for each translation. Qiao Chen had also identified what appeared to be the adsorption site, which would prove to be useful for positioning the tetracene in later studies [1]. For the unsaturated studies, larger models comprising 4 x 2 and 2 x 4 unit cells were used. These are described in more detail in section 5.1.3.

In all cases, care was taken to ensure that the surface comprised of the (110) plane; that there was sufficient vacuum above the oxygen terminated layer to ensure that there was no vertical interaction between unit cells and that the lattice parameters repeated the structure correctly in order to accurately model the substrate. The models were built and optimised under the Open Force Field method in Cerius^2 in order to provide a good starting position for *AIMpro*.

The charge density and wavefunction basis sets were optimised specifically for the system using *AIMpro*. First a face centred cubic copper unit cell was used to optimise the copper basis sets. Then a unit cell of copper (I) oxide was constructed and the basis sets for both copper and oxygen were optimised, using the face centred cubic copper result for the copper start point and pre-existing Ag_2O basis sets for the oxygen. The final results of the wavefunction basis set optimisation for metallic copper and copper (I) oxide are shown in table 5.1. Substitution of p-type functions for some of the d-types was attempted in order to simplify the calculation process but, in every case, the lattice parameter deviated too far from the experimental value to be acceptable. As it is, the bulk modulus calculated under LDA for face centred cubic copper seems rather high when compared to the accepted value [2], but it is only an intermediate step. The results for the copper (I) oxide basis sets, that are intended to actually represent the surface of the substrate, are much better, at least under LDA, when compared with the accepted values for cuprite, the mineral form of copper (I) oxide [3]. The use of contracted basis sets was attempted but no progress could be achieved here, with the resulting bulk modulus being ludicrously unphysical and sometimes even negative! As a result it was decided to employ the dddd basis sets to model the substrate. The model was optimised in *AIMpro* under both LDA and GGA while holding the lowest layer of Copper atoms fixed. Various dimensions of interest (see Figure 5.5) from the resulting structure were compared to experimental and theoretical values within the literature. The results of these

Literature Values	a_0/Å	a_0/norm	BM/GPa	BM/norm
Cu FCC (lit)[2]	3.6100	1.0000	140.00	1.0000
Cu_2O (lit)[3]	4.2670	1.0000	131.00	1.0000

Calculated Values	a_0/Å	a_0/norm	BM/GPa	BM/norm
fcc-dddd LDA	3.5531	0.9842	171.17	1.2226
Cu2O-dddd LDA	4.1875	0.9814	144.54	1.1034
fcc-dddd GGA	3.6426	1.0077	143.05	1.0218
Cu2O-dddd GGA	4.3194	1.0123	111.60	0.8519

Table 5.1: Wavefunction basis set optimisation for FCC Copper and SC Cu_2O

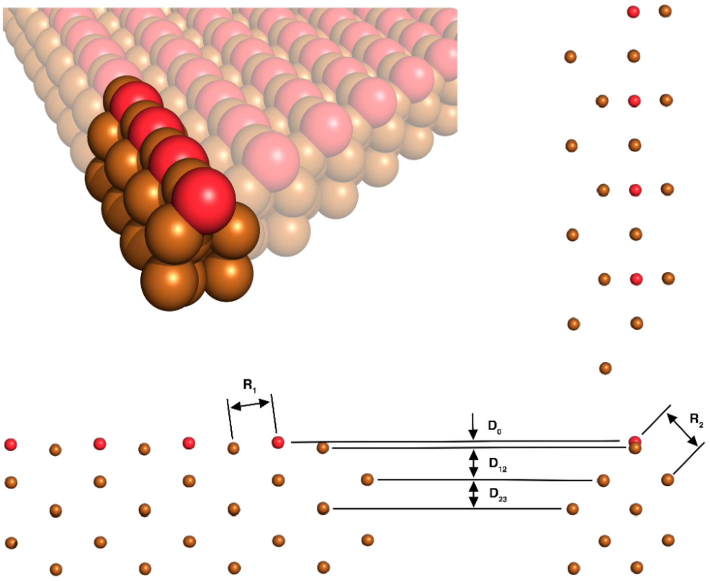

Figure 5.5: The 4 x 1 supercell of the oxygen terminated (110) copper surface, showing dimensions of interest.

Method	D_0/Å	D_{12}/Å	D_{23}/Å	R_1/Å	R_2/Å
ICISS [4][5]	-0.08	1.51	1.28	1.81	2.00
LEED [6]	+0.04	1.49	1.21	1.81	2.01
XRD [7]	-0.34	1.65	1.28	1.84	1.85
Schimizu, Tsukada (LDA) [8]	+0.55	1.32	0.97	1.89	2.27
Katagiri et al (GGA) [9]	+0.09	1.46	1.27	1.83	2.04
AIMpro (LDA)	+0.23	1.31	1.14	1.82	2.02
AIMpro (GGA)	+0.20	1.44	1.16	1.81	2.04

Table 5.2: Comparison of the optimised reconstructed row, oxygen terminated (110) copper surface to literature values.

dimensional studies are displayed in Table 5.2 and Figure 5.6, where they are compared with results from experiment and theory, specifically ICISS [4][5], LEED [6], XRD [7] and earlier LDA [8] and GGA [9] DFT studies. The strong agreement with the surface dimensions quoted in the literature lends a certain authority to the methodology used regarding optimised basis functions and selection of k-points. This is in agreement with the accepted wisdom that LDA tends to over-bind [10].

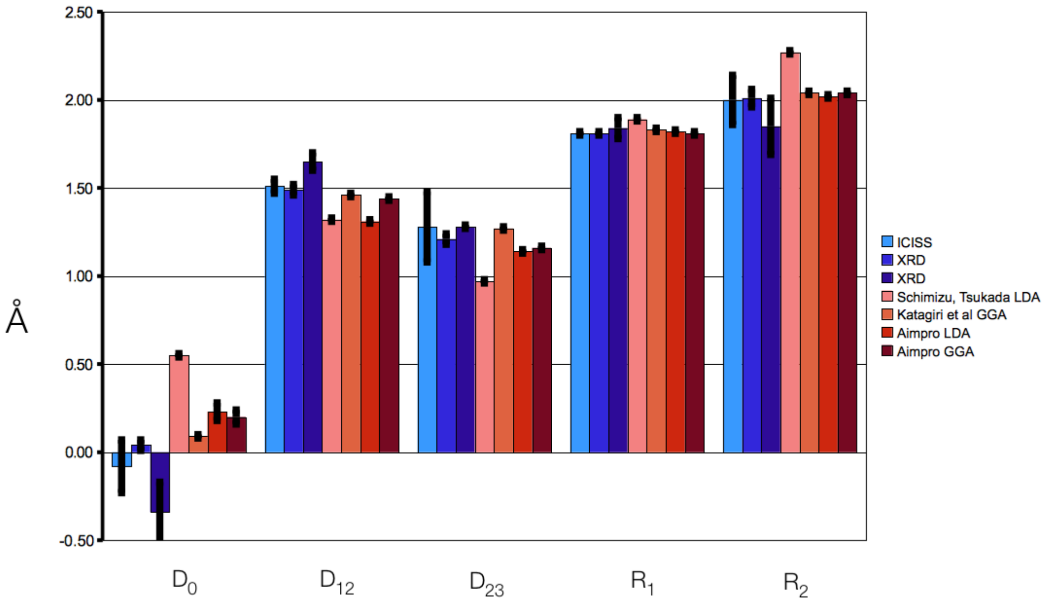

Figure 5.6: Comparison of the optimised reconstructed row, oxygen terminated (110) copper surface to literature values.

5.1.2 Saturated Adsorption

The models for three potential versions of the adsorbed tetracene molecule were constructed in Cerius^2, translated to the *AIMpro* format and then optimised. These three starting conformations, as shown in Figure 5.7, were constructed with the tetracene molecule placed differently in each case. They are identified according to the position of the central, cross-linking C-C bond: bridging, copper-centred or oxygen centred.

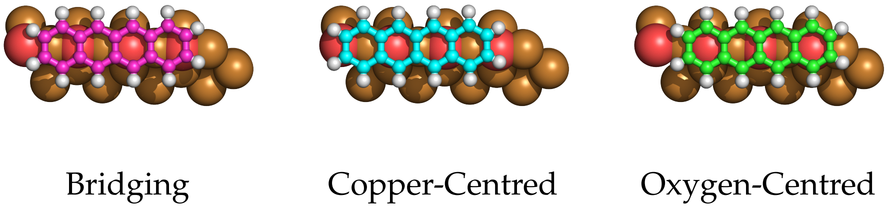
Bridging Copper-Centred Oxygen-Centred

Figure 5.7: The starting positions for the tetracene in relation to the surface.

In all cases involving the substrate, the positions of the lower three layers of copper atoms were held and a 2 1 8 MP k-point mesh was specified. For its optimisation, the tetracene molecule was placed within a 40 au cubic unit cell and treated as a periodic structure (using a 4 4 4 MP k-point mesh) in order to take advantage of the plane wave portion of the *AIMpro* code. All runs were conducted under both LDA and GGA. The adsorption energy for tetracene in the three different positions was then calculated as follows.

$$E_{ADS} = -(E_{SYS} - E_{SUB} - E_{TET}) \tag{5.1}$$

The results of the LDA optimisation are shown in table 5.3 and those for GGA are in table 5.4. The binding energies obtained differ significantly between LDA and GGA, although both methods establish that the Copper centred conformation has the lowest binding energy by around 200 meV. It is interesting to note that LDA places the oxygen centred conformation at a higher energy than the bridging conformation, while GGA has them reversed. It should be noted, however, that the difference in energy between these 2 conformations under LDA is significantly higher (around 60 meV) than under GGA (around 10 meV).

System	E_{ADS}/eV
Bridging	2.212
Cu-centred	2.041
O-centred	2.268

Table 5.3: Total energies for the 3 candidate adsorption sites under LDA

System	E_{ADS}/eV
Bridging	0.681
Cu-centred	0.411
O-centred	0.659

Table 5.4: Total energies for the 3 candidate adsorption sites under GGA

The results of the geometric optimisation provide more than just data regarding the final energies. We are also able to extract the co-ordinates for

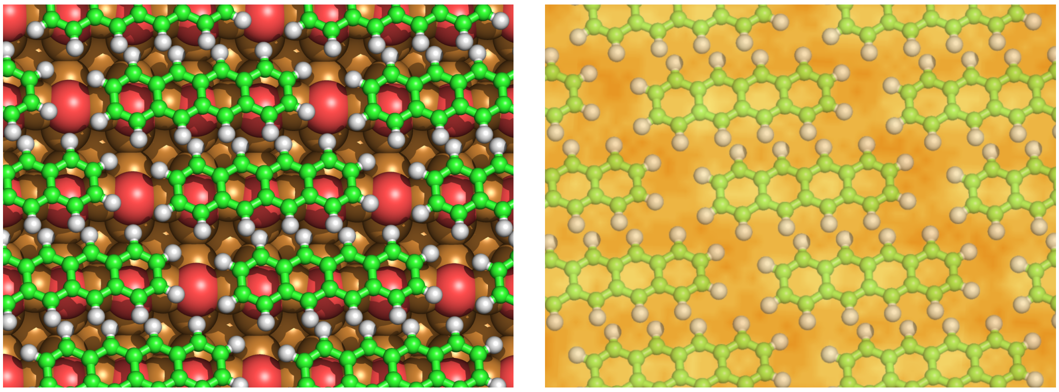

a b

Figure 5.8: a. Plan view of tetracene monolayer on the reconstructed row, oxygen terminated (110) copper surface, O-centred conformation. b. The same tetracene monolayer overlaid onto an STM image of similar system.

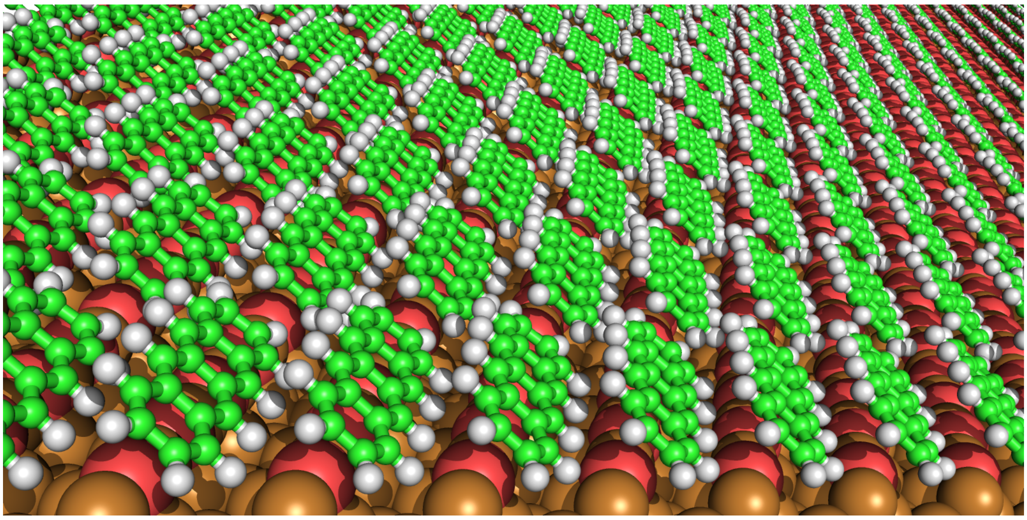

Figure 5.9: An Overview of the optimised, monolayer and surface, O-centred conformation.

the final positions of all the atoms in the system, and even repeat the unit cell in accordance with the lattice parameters. When looking at a view of one of these optimised systems, as in figure 5.8, we can see that the model of the tetracene does indeed self-assemble in a similar manner to that observed in the STM. Additionally, when viewed from the side or end-on, as in figure 5.9, it appears that the tetracene molecules are not able to lie flat. Instead they seem to be somewhat distorted from their normal, flat conformation and they also appear to adopt a staggered, overlapping formation, somewhat reminiscent of tiles on a roof. In order to quantify this non-parallel adsorption, the angles that each of the cross-linking C-C bonds make to the horizontal were measured. This is illustrated in Figure 5.10.

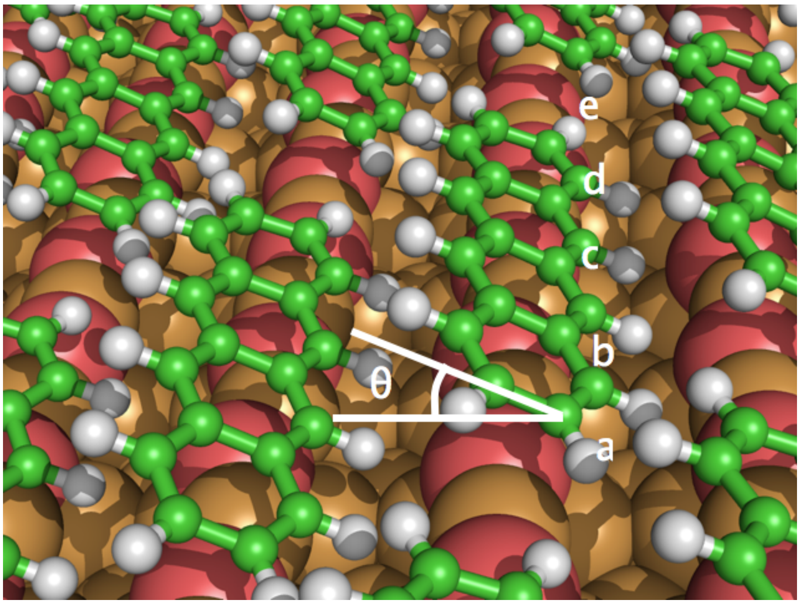

θ	a	b	c	d	e
angle	31.4^o	32.0^o	31.9^o	28.3^o	24.5^o

Figure 5.10: The non-parallel nature of the adsorption and the twisted nature of the tetracene molecules.

5.1.2.1 Analysing the Electronic Structure

In order to analyse the electronic structure of the system, such as its bandstructure and its molecular orbitals, it was necessary to construct its first Brillouin zone. As the system is a surface with no interactions normal to the surface plane, a two-dimensional construct will suffice. First, the reciprocal lattice vectors were calculated according to equations 5.2 and 5.3.

$$\bar{b}_1 = \frac{(\bar{a}_2 \times \bar{a}_3)}{(\bar{a}_1 \times \bar{a}_2) \cdot \bar{a}_3} \tag{5.2}$$

$$\bar{b}_2 = \frac{(\bar{a}_3 \times \bar{a}_1)}{(\bar{a}_1 \times \bar{a}_2) \cdot \bar{a}_3} \tag{5.3}$$

These vectors were plotted manually and used to construct the reciprocal lattice. The vectors from one point on this lattice to its nearest neighbours were bisected, moving progressively out from the central point. It was found that after the 3rd nearest neighbour vectors had been bisected, any additional constructs fell outside of the zone. The high symmetry points were then identified and their co-ordinates extrapolated in relation to the reciprocal lattice so that they could be incorporated into an analysis path for *AIMpro*. Please see Figures A.22 and A.23 in the appendix for scans of the geometrical construction. The distinct high symmetry points are A and B, at 2 corners of the Brillouin zone, and X, Y and Z, at the mid points of three sides.

Atom type	Quantity	Valence electrons	Sub-total
Copper	36	11	396
Oxygen	4	6	24
Carbon	18	4	72
Hydrogen	1	12	12
		Total	504

Table 5.5: The total number of electrons in the system

Table 5.5 shows the total number of electrons in the system. Hund's rule and the Pauli exclusion principle mean that level 252 is the HOMO and level 253 is the LUMO. Analysis runs were conducted over the path X-A-Y-B-Z , and between levels 246-261.

5.1.2.2 The Bandstructure and Molecular Orbitals

The bandstructure for the system is presented in Figure 5.11. Mulliken analysis of the system was conducted at the Γ point. This is illustrated in Figure 5.12

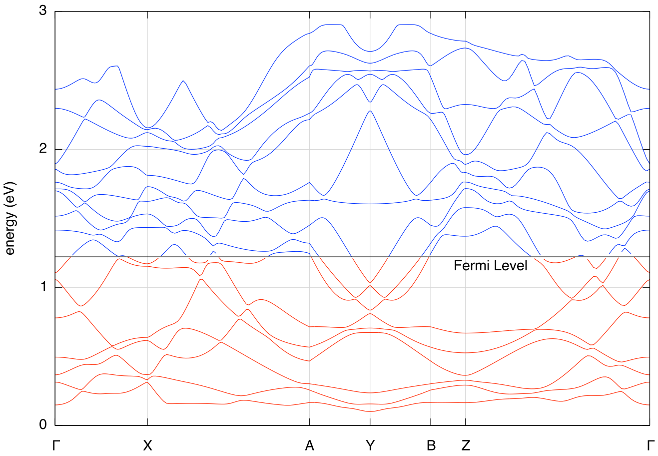

Figure 5.11: The bandstructure for tetracene adsorbed on the oxygen terminated, reconstructed row Copper (110) surface, levels 246-261.
A larger version is presented in the Appendix, Figure B.14

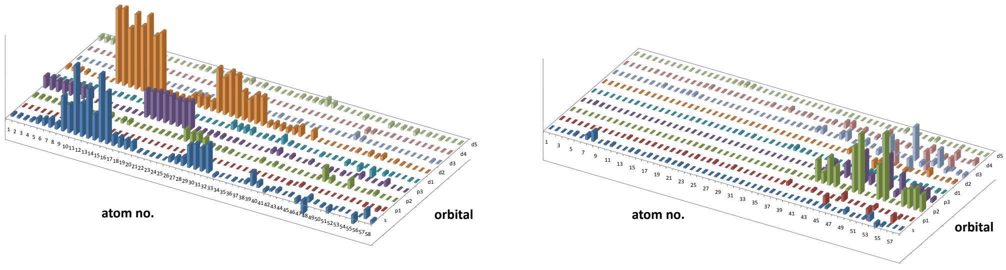

HOMO LUMO

Figure 5.12: Results of the Mulliken analysis for the tetracene absorbed on the oxygen terminated, reconstructed row Copper (110) surface. Atoms 1-40 are the substrate.

and indicates that electron density is concentrated on the substrate for level 252, the HOMO, and on the absorbate for level 253, the LUMO. The portion of the bands that this relates to is shown in Figure 5.13. The Molecular orbitals for the HOMO and LUMO are presented in Figure 5.14. Particular attention

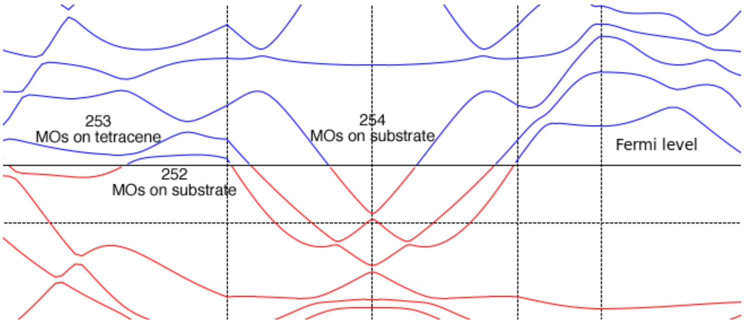

Figure 5.13: A portion of the bandstructure in Figure 5.11

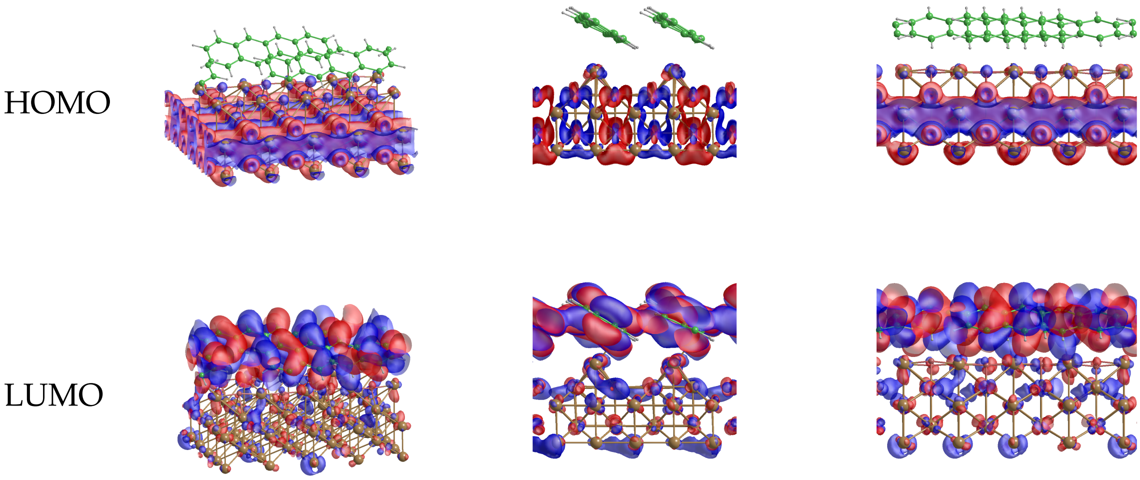

Figure 5.14: The HOMO and LUMO for tetracene adsorbed on the oxygen terminated, reconstructed row Copper (110) surface

should be paid to the way that the orbitals overlap from the upper surface of one tetracene molecule to the lower surface of its neighbour.

5.1.2.3 Simulating an STM Image

The same general method as was employed to generate scanning tunneling micrographs of graphitic surfaces in Chapter 4 was employed here. The wavefunctions concerned were identified and a cross-section was plotted using *AIMview*. This method yields simulated constant height micrographs of planar surfaces. It is not well suited to repeating ridged structures, such as the tetracene monolayer on the oxygen terminated copper (110) surface. However, with a little ingenuity, a reasonable approximation may be produced. Instead of plotting a horizontal cross-section, two angled cross-sections may be defined that approximate the ridged nature of the surface, as in Figure 5.15. So long as the base of the prism-like structure that is formed corresponds to an appropriate unit cell for the lattice, the two angled cross-sections can be projected to the horizontal plane and assembled to form a reasonable basis for generating a simulated scanning tunneling micrograph.

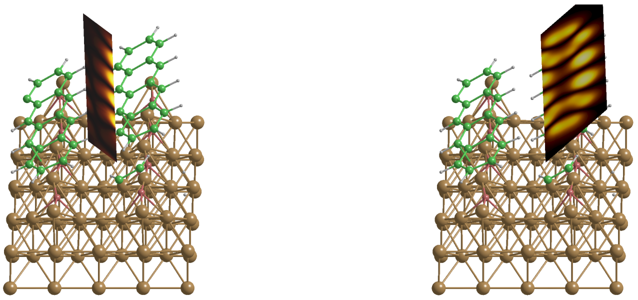

Figure 5.15: The two cross-sections that were used to Simulate constant height on the interleaved surface.

The steps for this procedure are shown in Figure 5.16 Some care needs to be exercised in the assembly of the unit cell and its duplication. In particular, it is tempting to align the unit cells corner to corner but this would not reproduce the lattice accurately. Instead, the structure should be repeated according to the lattice parameters for the system. The assembled image is presented in Figure 5.17 and it compares favourably with experimental images from Qiao Chen, such as Figure 5.18.

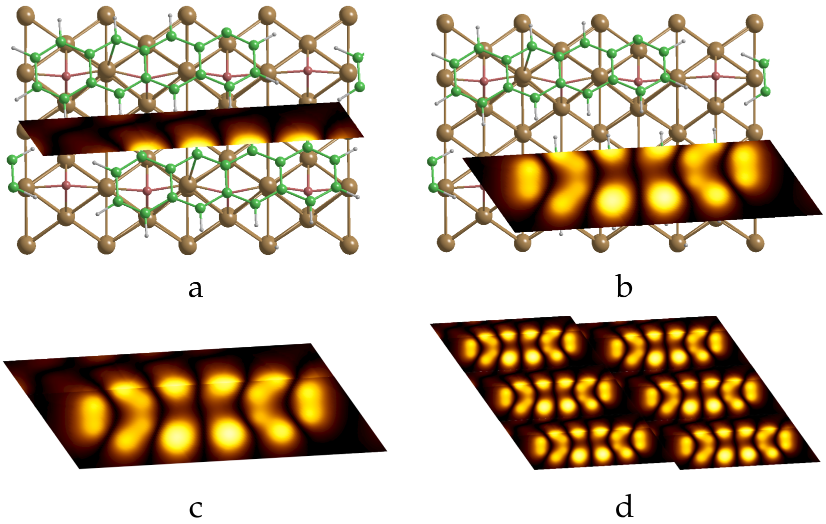

Figure 5.16: The steps employed to simulate the constant height micrograph of the interleaved surface.
a and b. The two component images as produced by *AIMview*. c. The assembled image for the unit cell. d. Six images assembled according to the correct lattice parameters.

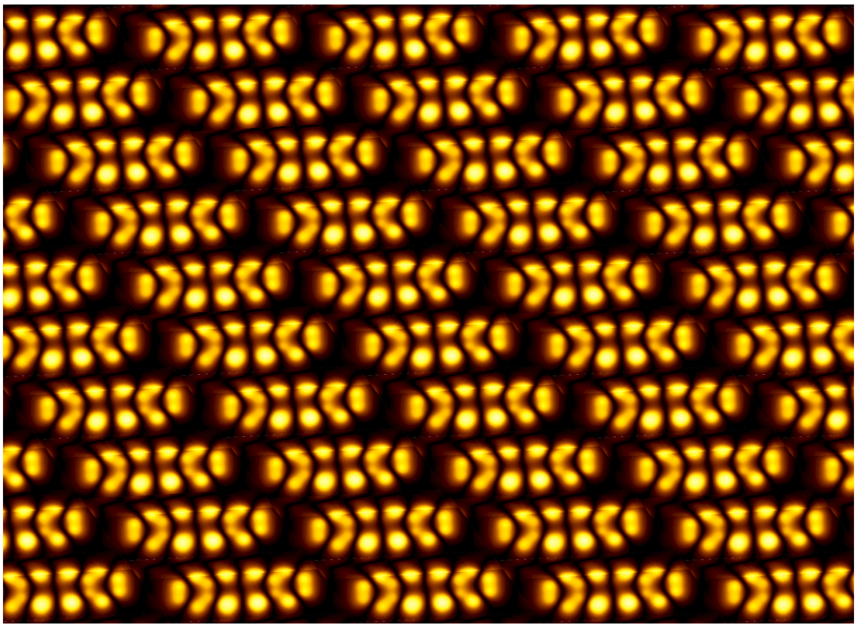

Figure 5.17: The completed simulated scanning tunneling micrograph of a tetracene monolayer on the oxygen terminated, reconstructed row Copper (110) surface

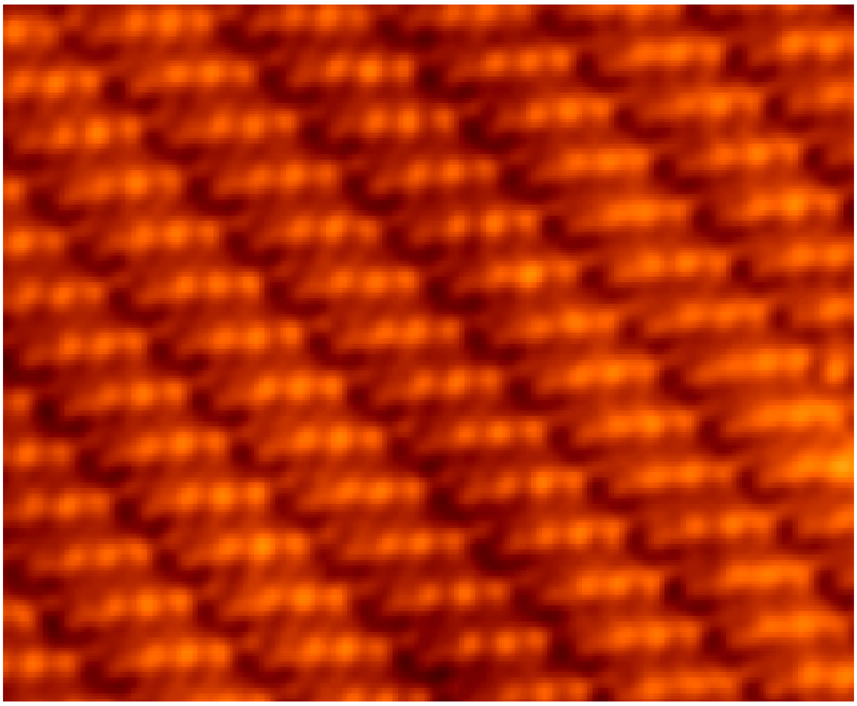

Figure 5.18: An experimental STM image of a tetracene monolayer on the oxygen terminated, reconstructed row Copper (110) surface

5.1.3 Unsaturated Adsorption

Experimental observations of lower concentrations of tetracene on the reconstructed row, oxygen terminated (110) Copper surface show tetracene molecules adopting two distinct orientations in relation to the reconstructed rows, either parallel or perpendicular to them, as shown in Figure 5.19 from Qiao Chen's experimental observations. This would suggest that, although the saturated monolayer's energetically preferred conformation is to be formed from molecules lying parallel to the rows, there are local energy minima representing more than one stable orientation where the coverage is lower. This can also be investigated using DFT.

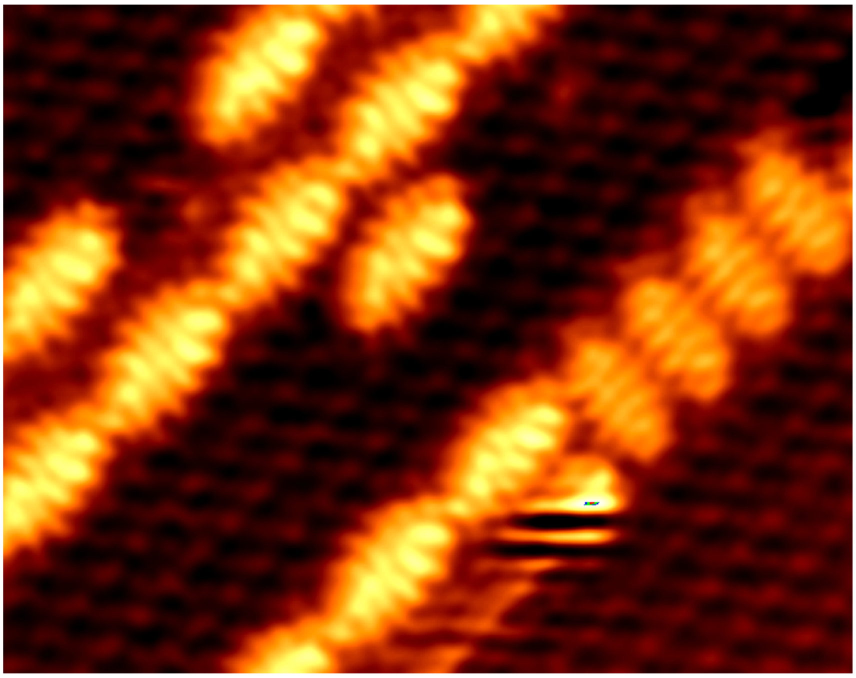

Figure 5.19: An experimental STM image of unsaturated coverage of tetracene on the oxygen terminated, reconstructed row Copper (110) surface

Two periodic models of the surface were built, each one using twice the number of copper and oxygen atoms in order to represent twice the surface area that had been used to model the monolayer. These models differed in the orientation of their "long" axes: one was parallel to the reconstructed rows; the other was perpendicular. Lattice vectors were chosen in order to minimise the

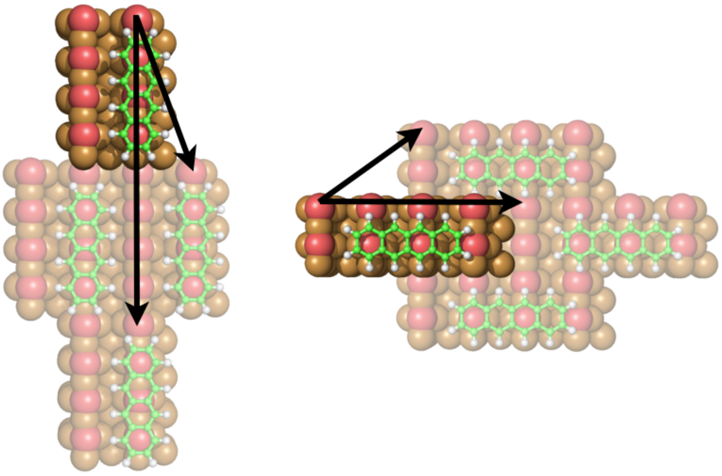

Figure 5.20: The initial placement for the parallel and perpendicular conformations. Arrows indicate lattice vectors.

interactions between tetracene molecules in neighbouring unit cells, once they were added, and the unit cells were optimised. The basis sets from the previous investigation were used, the k-point sampling was chosen in order to produce a similar mesh and the calculations were run under GGA. Furthermore, two types of copper atoms were specified in the species listing. Copper atoms in the bulk of the solid were considered to be FCC-copper, while copper atoms neighbouring oxygen atoms were considered to be cuprite, or Cu_2O. The placement of the tetracene molecule in relation to the atoms of the surface in the parallel conformation was taken directly from the starting placement of the energetically favourable conformation of the monolayer, while the initial placement of the perpendicular conformation was achieved by simply rotating the tetracene molecule about an axis running perpendicularly through the centre one of the end ring structures. The two initial conformations for this experiment are shown in Fig 5.20. During the runs the distance between the tetracene molecules and the substrate was optimised. In neither case did the adsorption site of the tetracene molecules change from their initial condition, although there were no constraints placed on them in this respect. The final energies for the two systems are shown in table 5.6.

System	E_{ADS}/eV
Tetracene on Parallel Substrate	0.108
Tetracene on perpendicular Substrate	0.310

Table 5.6: Results for the unsaturated reconstructed row, oxygen terminated (110) copper surface.

The results clearly show that the parallel conformation is the more energetically favourable but the difference of around only 0.2 eV is low enough that, in the case of low coverage, molecules in both conformations may be reasonably expected to be present.

5.2 References

[1] Qiao Chen. Presentation of ongoing research. 2007.

[2] Mark Winter. WebElements Periodic Table of the Elements. (http://www.webelements.com/copper/), 2008.

[3] JR Smyth, SD Jacobsen, and RM Hazen. Comparative crystal chemistry of dense oxide minerals. *Reviews in Mineralogy*, 40(9):1–24, 2000.

[4] T Fauster, R Schneider, and H Dürr. Added-row growth of the (2 x 1) O-Cu (110) reconstruction. *Physical Review B*, 43(2):1802–1804, 1991.

[5] T Fauster, R Schneider, and H Dürr. Surface structure determination of the (2 x 1) O-Cu (110) reconstruction by low-energy ion scattering. *Surface Science*, 244:237–246, 1991.

[6] S Parkin, H Zeng, M Zhou, and K Mitchell. Low-energy electron-diffraction crystallographic determination for the Cu(110) 2 x 1- O surface structure. *Physical Review B*, 41(8):5432–5435, 1990.

[7] R Feidenhans'l, Francois Grey, M Nielsen, F Besenbacher, F Jensen, E Laegsgaard, I Stensgaard, K Jacobsen, J Nørskov, and R Johnson. Oxygen chemisorption on Cu(110): A model for the c(6 x 2) structure. *Physical Review Letters*, 65(16):2027–2030, 1990.

[8] T Schimizu and M Tsukada. Origin of the different formation modes of the oxygen added row overlayer on Ag (110) and Cu (110) surfaces. *Surface Science*, 295:L1017–L1022, 1993.

[9] H Katagiri, T Uda, and K Terakura. Structural and vibrational properties of added-row reconstructions on O/Cu (110) and O/Ag (110) surfaces. *Surface Science*, 424:322–330, 1999.

[10] Shobhana Narasimhan and Stefano de Gironcoli. Ab initio calculation of the thermal properties of Cu. *Physical Review B*, 65(6):064302, 2002.

Chapter 6

Conclusion

6.1 Scanning Tunneling Microscope Tips

The central idea that the simplification of a scanning microscope tip to a single atom is very unrealistic has been vindicated. The change in energy per atom for the optimised structures as bulk begins to dominate surface effects shows that fidelity of the models improves with size and the lateral extent of the wavefunctions is evidence that the tip-surface interactions are likely to be far more complex than can be modelled using a simple point-source. However, no easily observable pattern within the electronic structure is evident spreading from the tip atom towards the bulk as the models' complexity is increased. If any pattern could be said to have emerged, it would be at the interfaces where the tip models would be joined to the bulk of the probes. In the absence of a method to simulate this bulk, it would seem that all this part of the project has achieved is to model some interesting Tungsten nanoparticles of a somewhat constrained crystal structure. If further research is to be attempted in this field, some way to simulate the full continuum of the bulk material attached to the base of each model will likely be required.

Another point is worth noting here. The current practice of simulating the results of scanning tunneling microscopy tend to rely on the Tersoff-Hamann approximation, equation 2.3, where the tip is explicitly required to be considered a point-source. Any attempt to include a complex tip model in the calculation of simulated images would require a transition to the use of the full expression, equation 2.1, and the increase in computational overheads that would entail. On a more positive note, some generalised gradient approximation basis sets for Tungsten have been added to the *AIMpro* knowledge pool.

6.2 Graphitic Surfaces

This section's results are more positive. Modelling the bandstructures and orbitals of graphite and graphene, together with its multi-layer siblings, has been achieved. An explanation for the interaction between the layers in graphitic-type carbon substances has been offered with the bonding and anti-bonding orbitals clearly identified. A fairly simple method of producing constant height scanning tunneling micrographs of surfaces has been described and the resulting images compare well to the various images in the literature. Known defects in graphitic materials have been modelled and analysed within the context of bi-layer graphene. Their effect on the bandstructure of pristine material has been studied and simulated STM images predicting their appearance have been produced. These images are in reasonable agreement with experimental data and other simulations where available. If this line of enquiry were to be continued, it would certainly be useful to collaborate with an experimentalist in order to track down specific surface defects and compare their appearance to these predictions.

6.3 Tetracene on Copper Surfaces

In this portion of my research, the oxygen terminated Copper (110) surface has been modelled successfully and its dimensions, as modelled, compare well with values from experiment and other simulations, validating the uncontracted basis sets that were produced. The non-parallel nature of the adsorption of tetracene on the surface, along with the energy of adsorption has been described. The way that the electron density changes its localisation sharply from substrate to adsorbate at the frontier orbitals, along with the orbital overlap between neighbouring tetracene molecules, may offer some explanation for the phenomenon of imaging through the tetracene.

A constant height scanning tunneling micrograph of the tetracene monolayer has been simulated by a method of approximation, although no method has been found that is able to reproduce the "image-though" behaviour. Given that this behaviour seems to occur at specific tunneling currents, a method of generating constant-current scanning tunneling micrographs would likely be of assistance here.

6.4 Discussion

The one major realisation that has forced itself upon me over the course of my research is one that I am fairly sure every theoretician must come to. It is that, even with the massive computational resources available to us, the complexities involved in electronic interactions are still beyond analysis for all but relatively simple systems. That said, the meaning of "relatively simple" changes all the time. The capabilities of hardware and software are being developed constantly over time and recent advances in *AIMpro* promise the ability to analyse orders of magnitude more atoms in the near future. Much of this work, particularly the scanning tunneling micrograph simulations of the graphitic surface defects, would benefit from being repeated using the new code running on more modern clusters with considerably larger unit cells in order to further isolate the defects under analysis. The ability to model significantly larger numbers of atoms would also be useful in order to study similar defects on multi-layered graphitic surfaces.

And what of the matter compiler envisaged in the introduction to this thesis? I have to conclude that, given the immense computational resources required to simulate even these relatively simple systems, and given the significant infrastructure required to control even a single SPM tip acting alone, the ambition to build some kind of device capable, not only of coordinating the quantum chemical calculations, but also controlling the billions of billions of SPM tips that would be required, is so impractical as to be unrealistic for the foreseeable future. But that is not to say that some device with similar functionality won't be available in the future. It is easy, for example, to imagine high-resolution versions of the currently available 3D rapid-prototyping machines, equipped with multiple polymer deposition systems dispensing materials with differing electronic and mechanical properties as required. Even operating at the microscale, rather than the nano, as envisaged at the start of this project, a device similar to the matter compiler in functionality would likely seem to be inevitable.

Appendix A

Images and Scans

Many of the figures included in the body of this thesis have been rendered at a very small scale, leaving some of their details illegible. This section consists of larger renders of some of these figures and is included for the sake of clarity. Also included are scans of hand-written material.

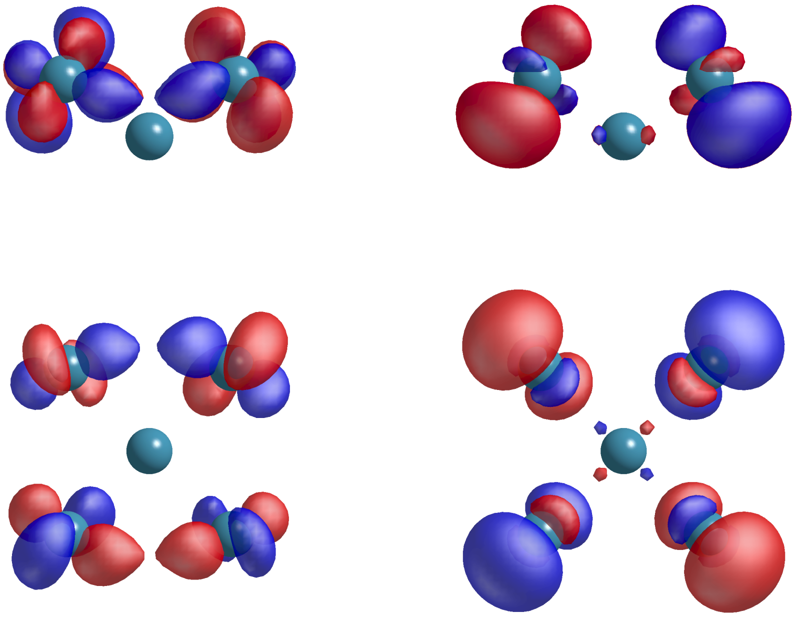

HOMO LUMO

Figure A.1: HOMO and LUMO of the Tungsten (100) 1 layer STM tip model

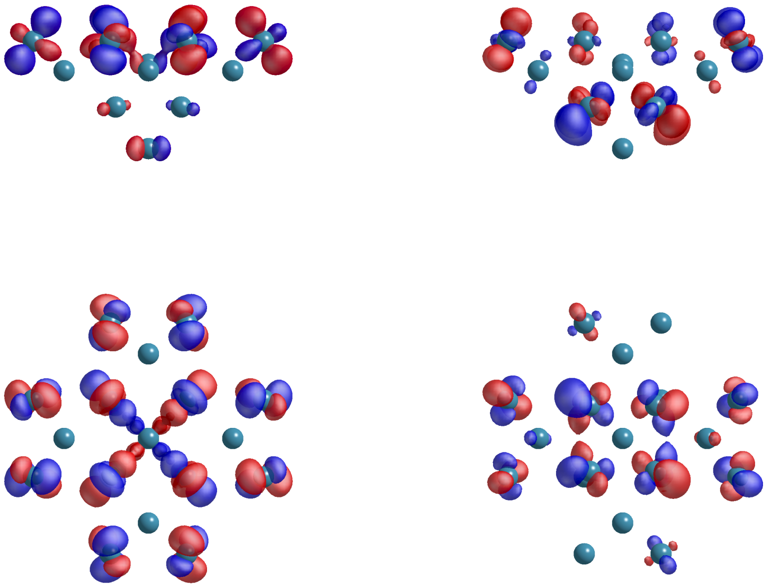

HOMO LUMO

Figure A.2: HOMO and LUMO of the Tungsten (100) 2 layer STM tip model

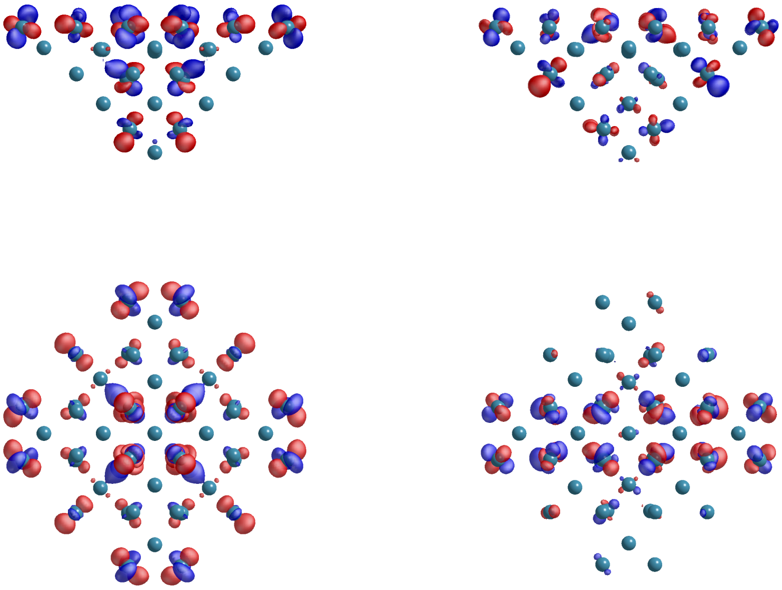

HOMO LUMO

Figure A.3: HOMO and LUMO of the Tungsten (100) 3 layer STM tip model

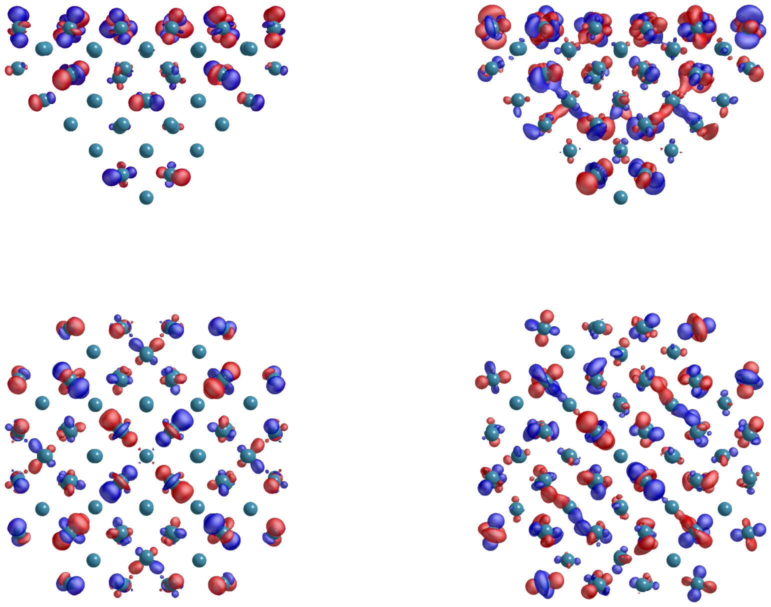

HOMO LUMO

Figure A.4: HOMO and LUMO of the Tungsten (100) 4 layer STM tip model

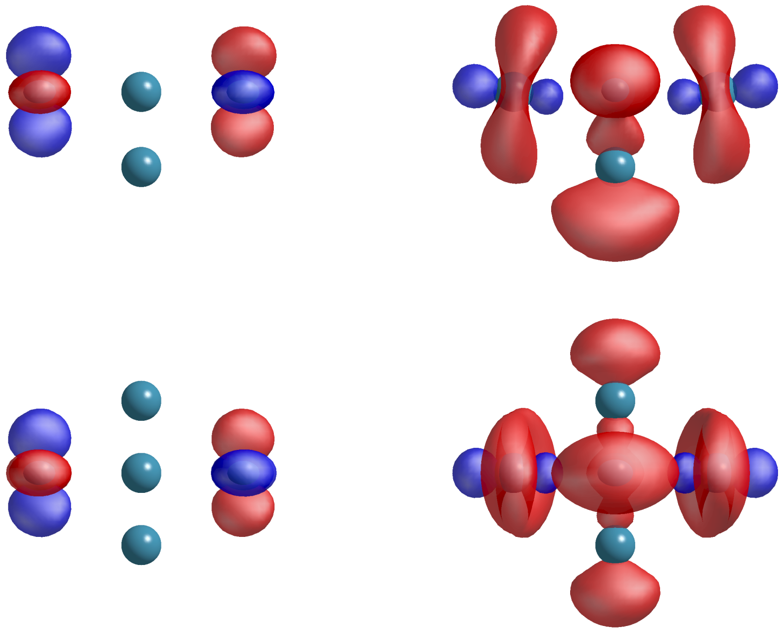

HOMO LUMO

Figure A.5: HOMO and LUMO of the Tungsten (110) 1 layer STM tip model

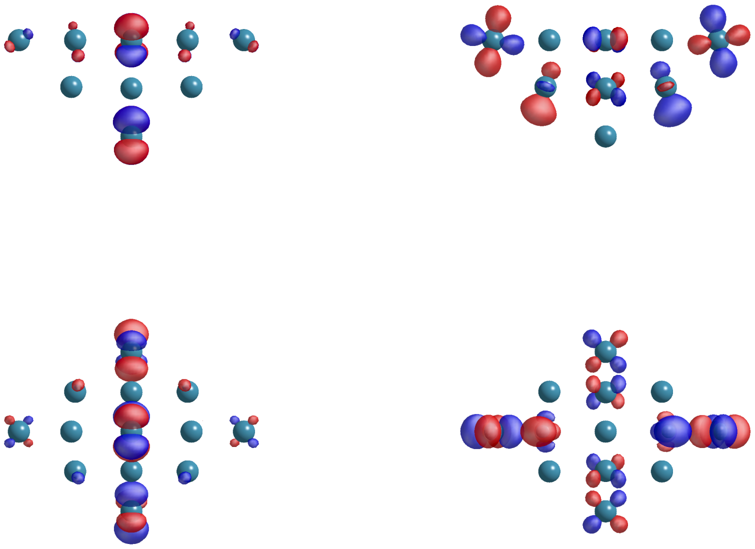

HOMO LUMO

Figure A.6: HOMO and LUMO of the Tungsten (110) 2 layer STM tip model

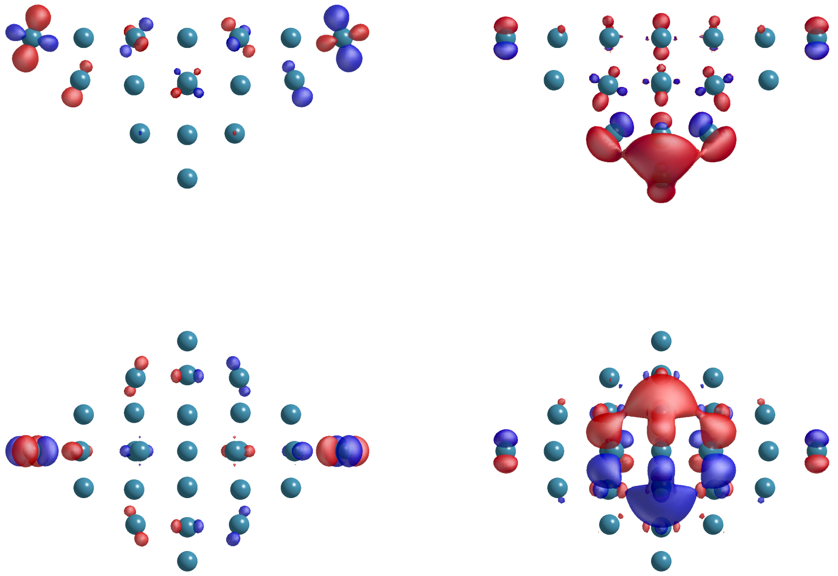

HOMO LUMO

Figure A.7: HOMO and LUMO of the Tungsten (110) 3 layer STM tip model

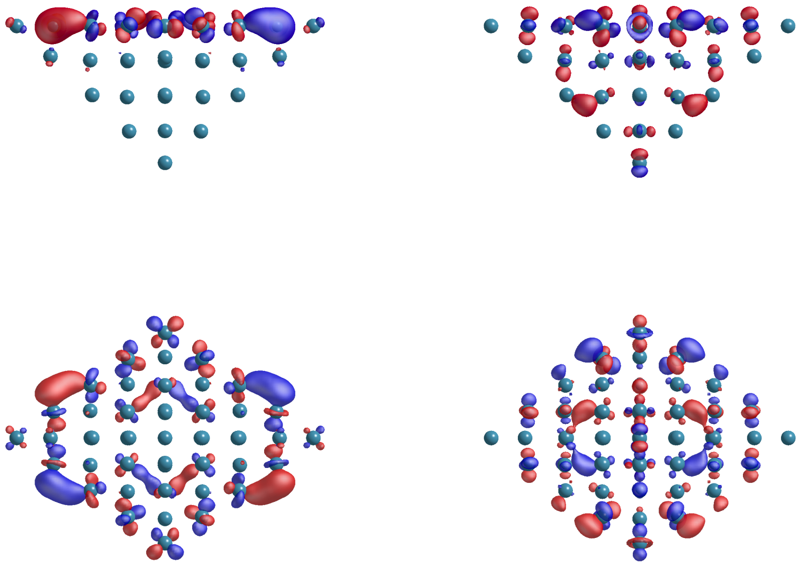

HOMO LUMO

Figure A.8: HOMO and LUMO of the Tungsten (110) 4 layer STM tip model

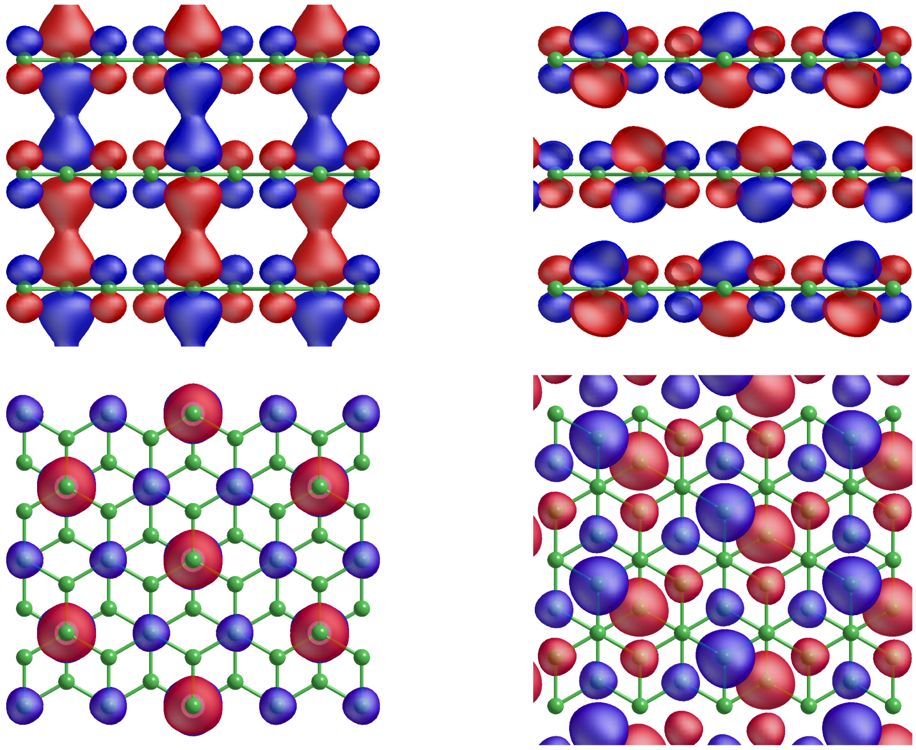

HOMO -1
(bonding)

HOMO
(non-bonding)

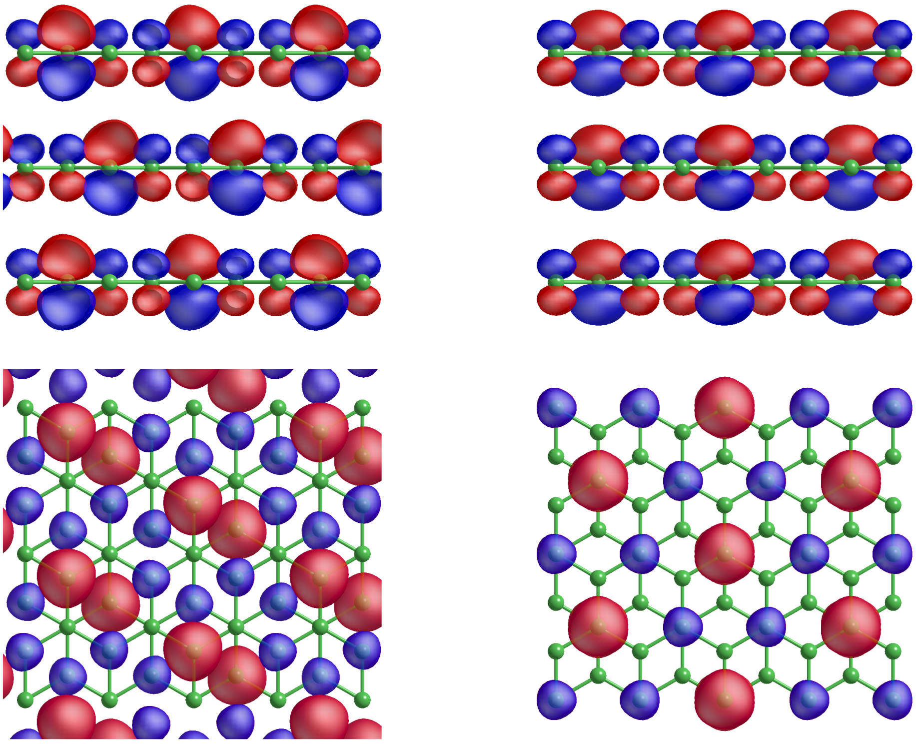

LUMO
(non-bonding)

LUMO +1
(anti-bonding)

Figure A.9: The molecular orbitals responsible for the interlayer bonding in graphite

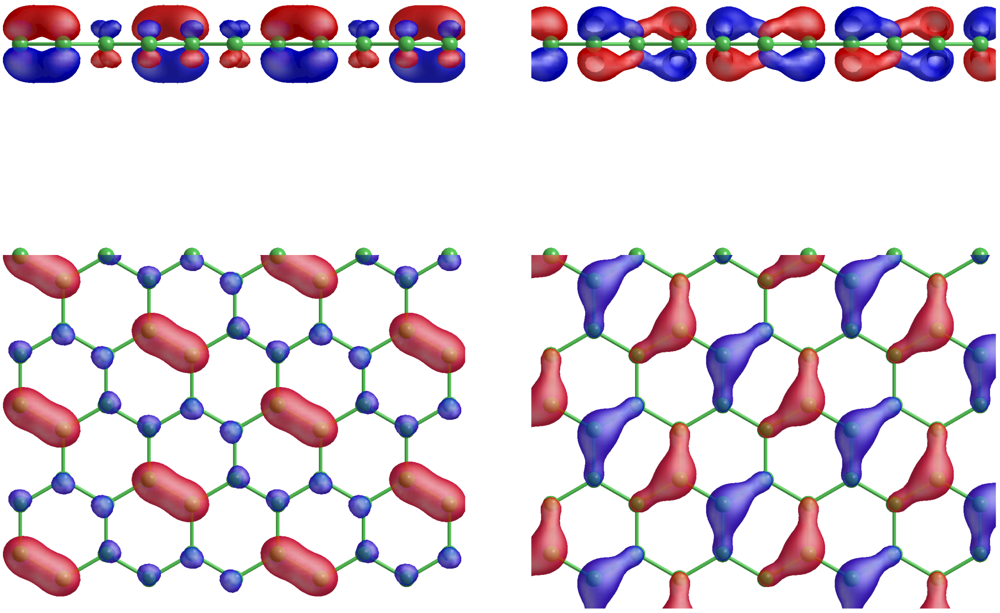

HOMO
(bonding)

LUMO
(anti-bonding)

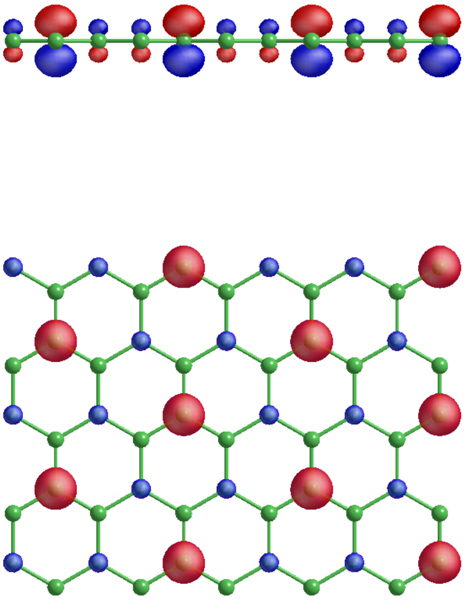

Linear Combination

Figure A.10: The molecular orbitals of graphene

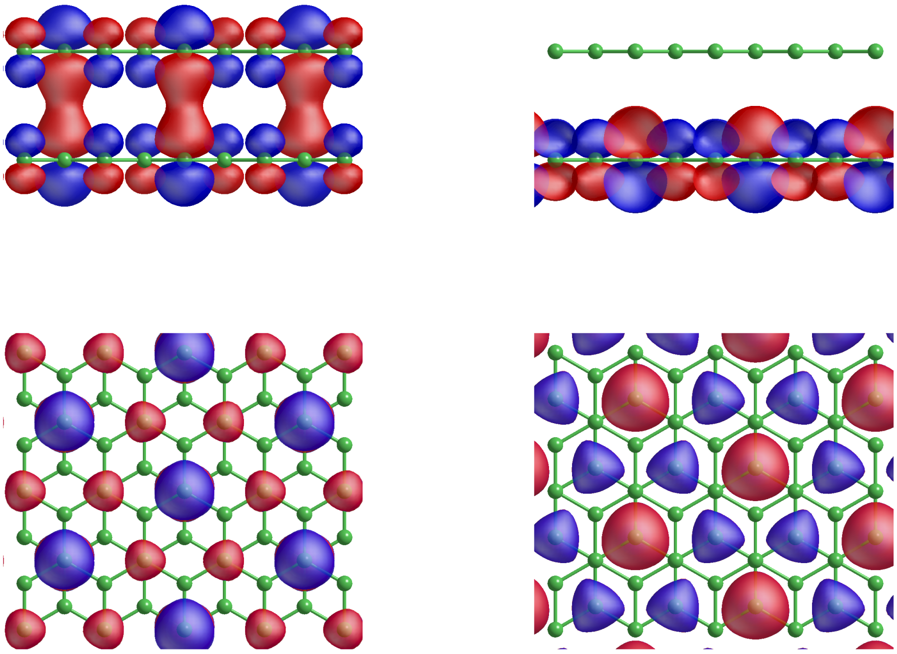

HOMO -1
(bonding)

HOMO
(non-bonding)

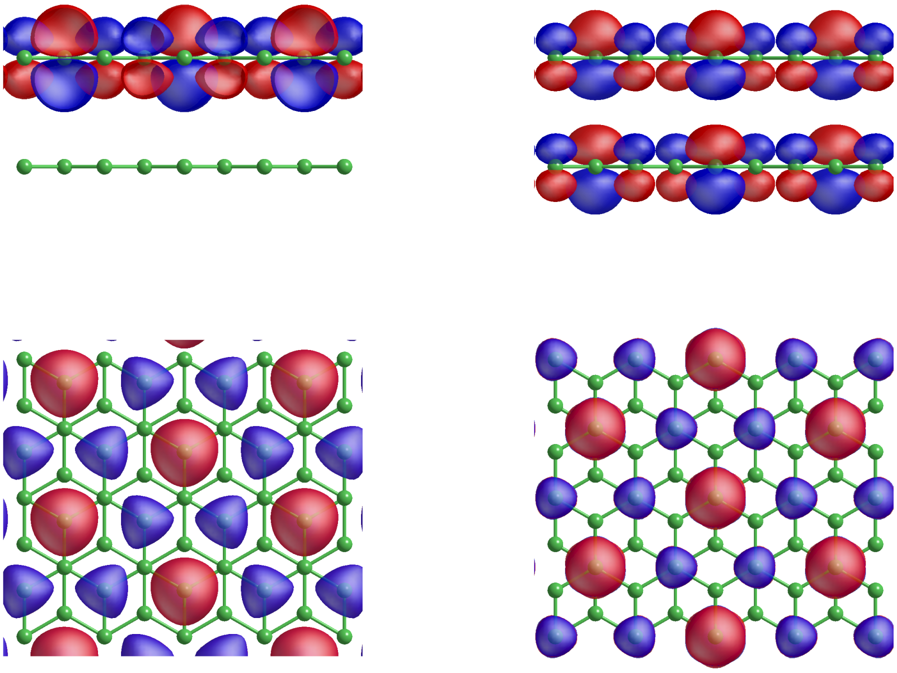

LUMO
(non-bonding)

LUMO +1
(anti-bonding)

Figure A.11: The molecular orbitals of bi-layer graphene

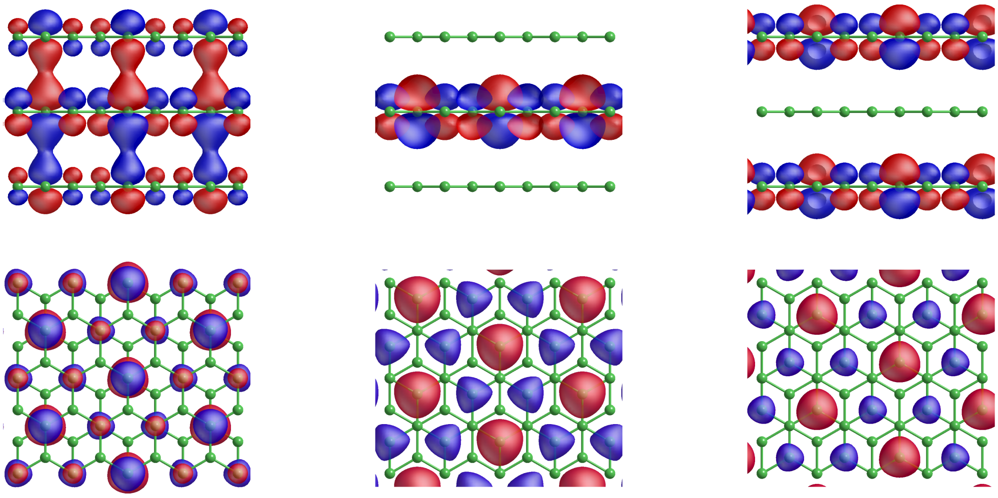

HOMO-2
(bonding)

HOMO -1
(non-bonding)

HOMO
(non-bonding)

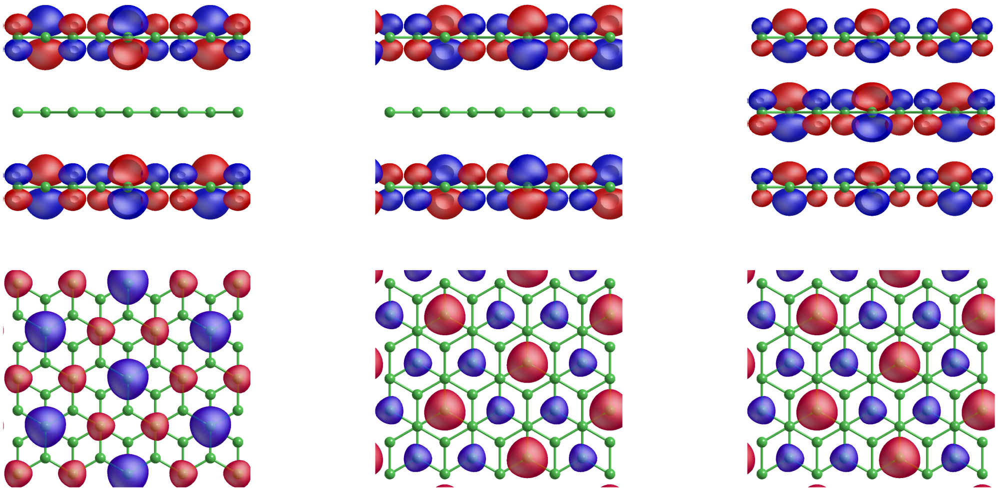

LUMO
(non-bonding)

LUMO +1
(non-bonding)

LUMO+2
(anti-bonding)

Figure A.12: The molecular orbitals of tri-layer graphene

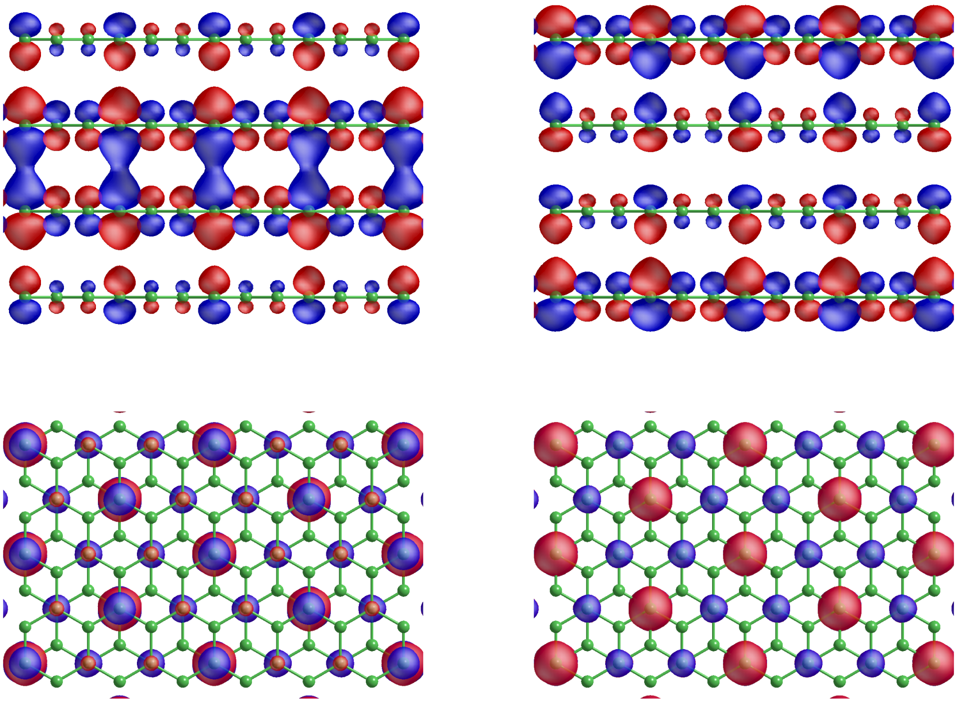

HOMO -3
(bonding)

HOMO-2
(bonding)
(not layers 2 and 3)

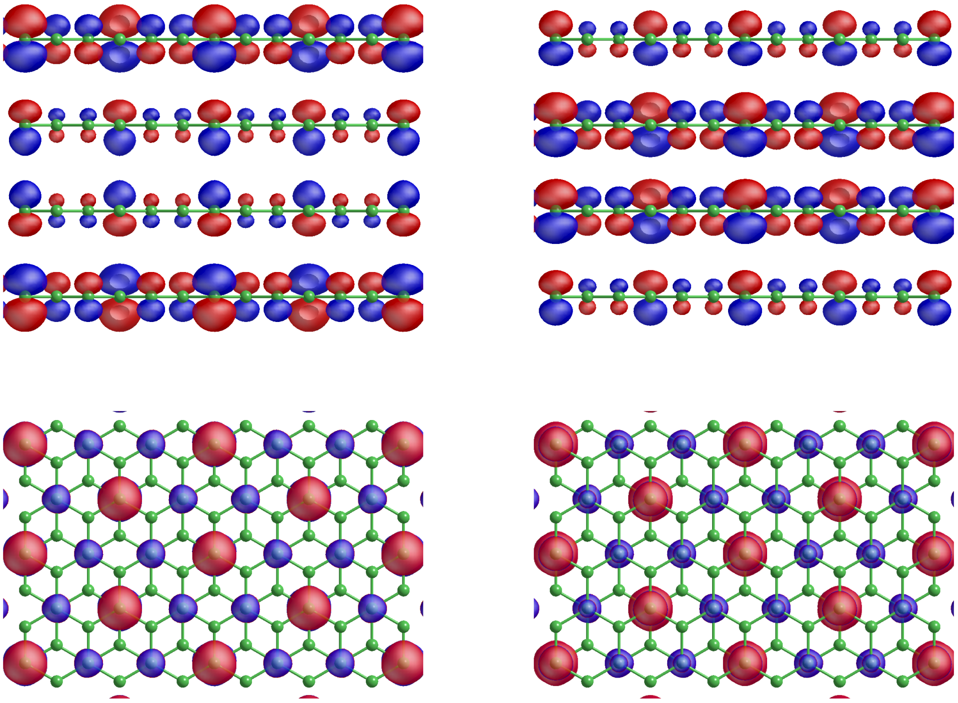

LUMO+2
(anti-bonding)
(not layers 2 and 3)

LUMO +3
(anti-bonding)

Figure A.13: The bonding and anti-bonding molecular orbitals of quad-layer graphene

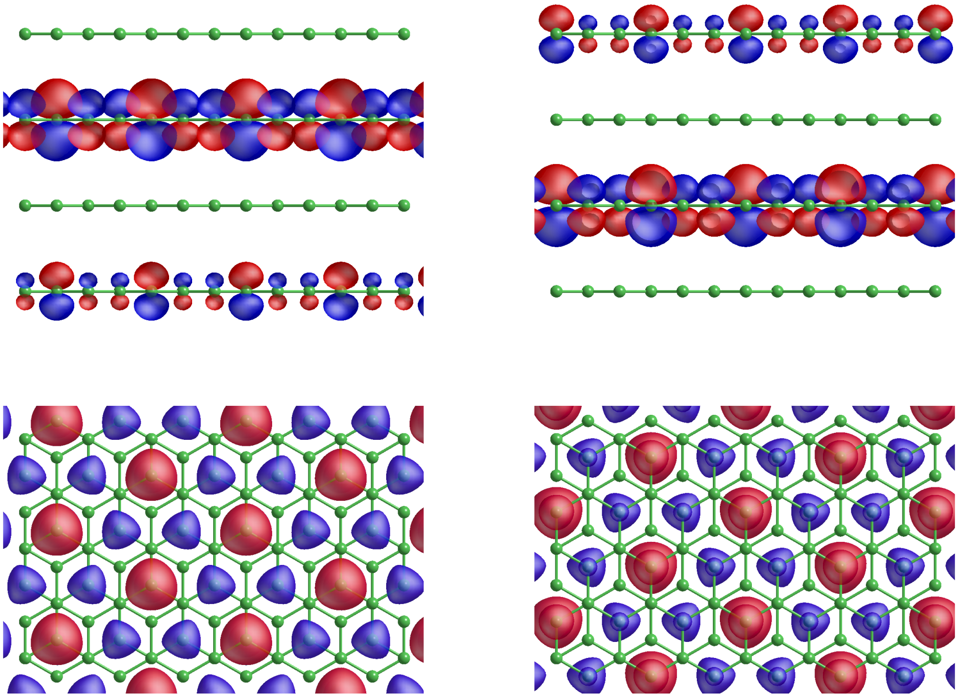

HOMO -1
(non-bonding)

HOMO
(non-bonding)

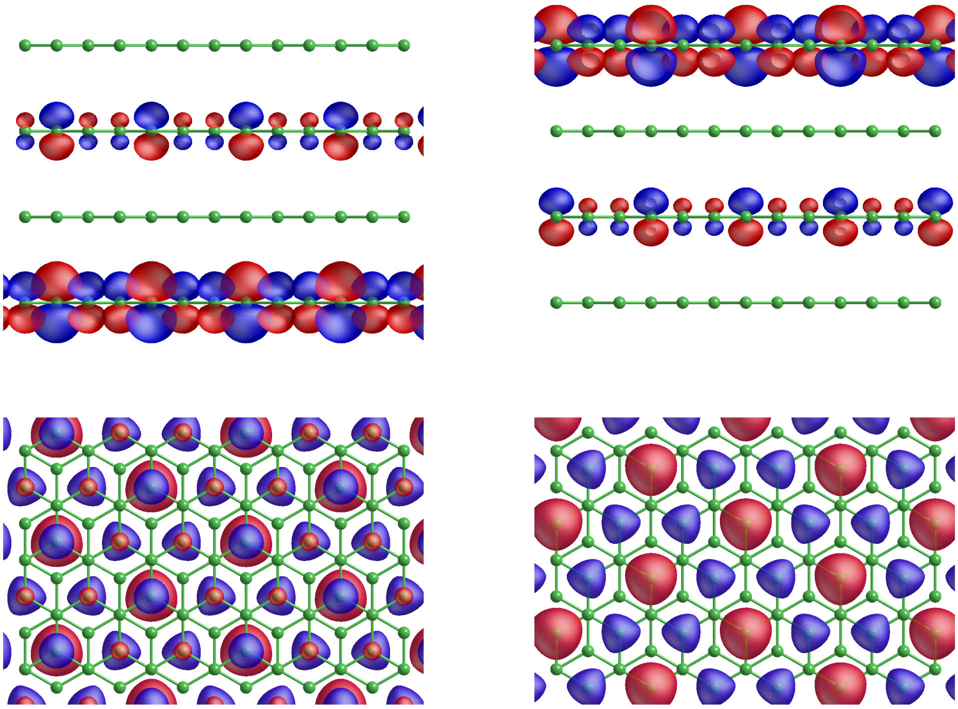

LUMO
(non-bonding)

LUMO +1
(non-bonding)

Figure A.14: The non-bonding molecular orbitals of quad-layer graphene

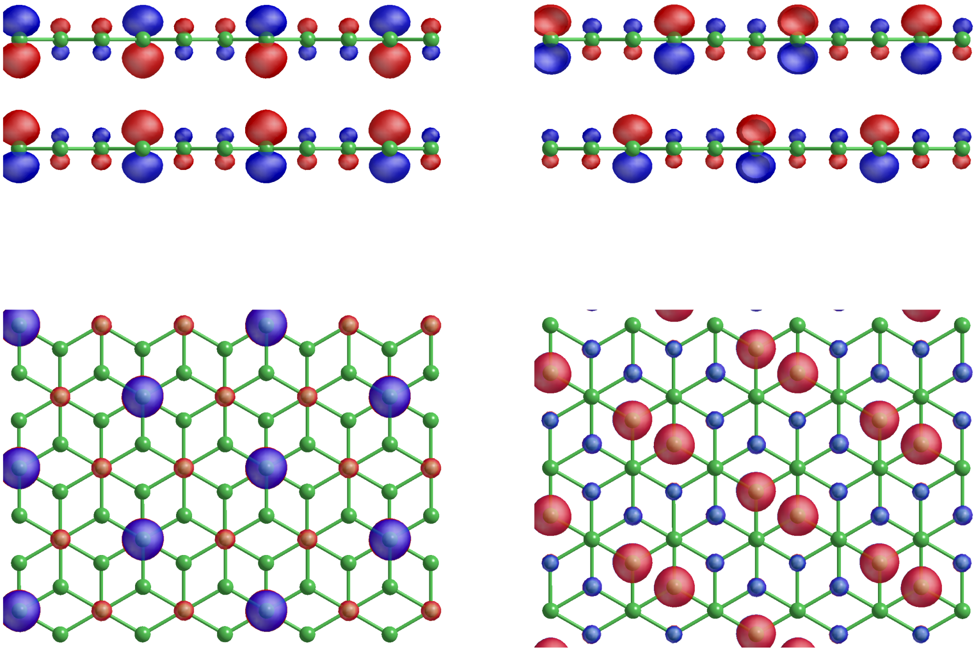

HOMO -1

HOMO

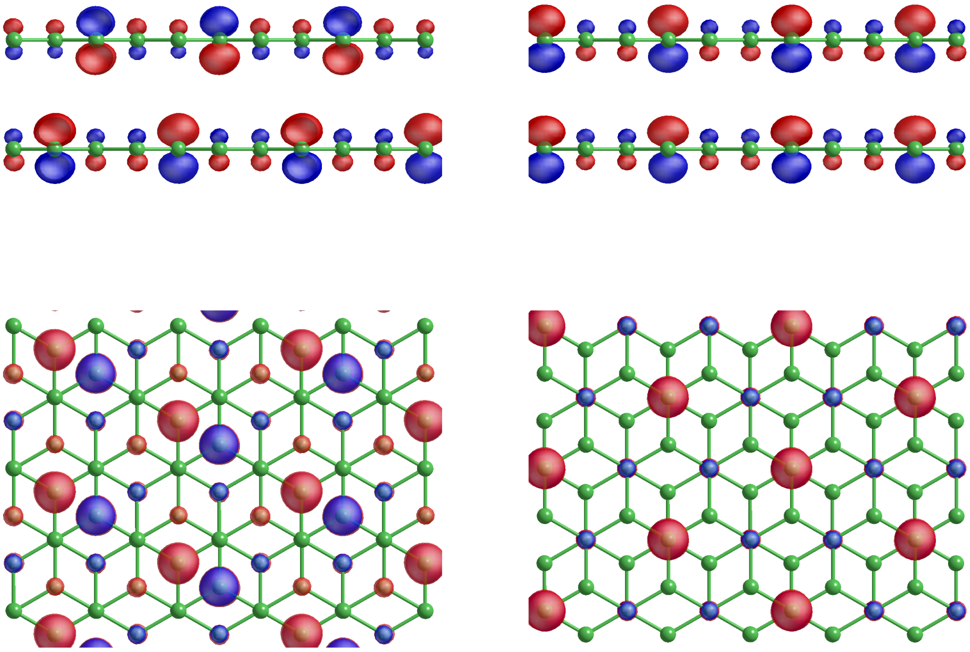

LUMO

LUMO +1

Figure A.15: The frontier orbitals for pristine, bi-layer graphene modelled in a 256 atom supercell.

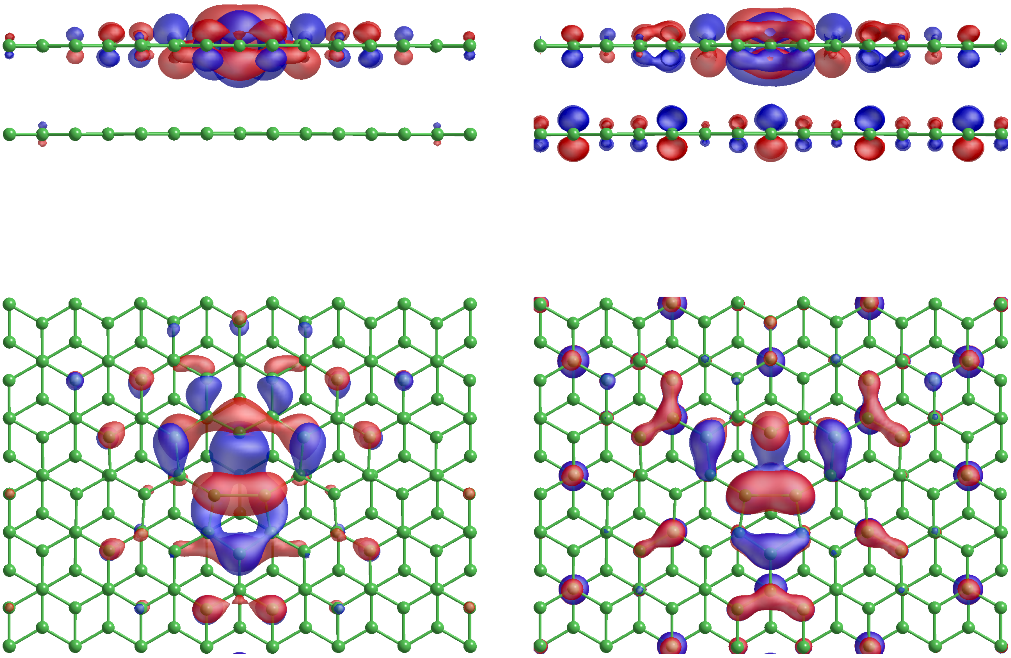

HOMO SOMO

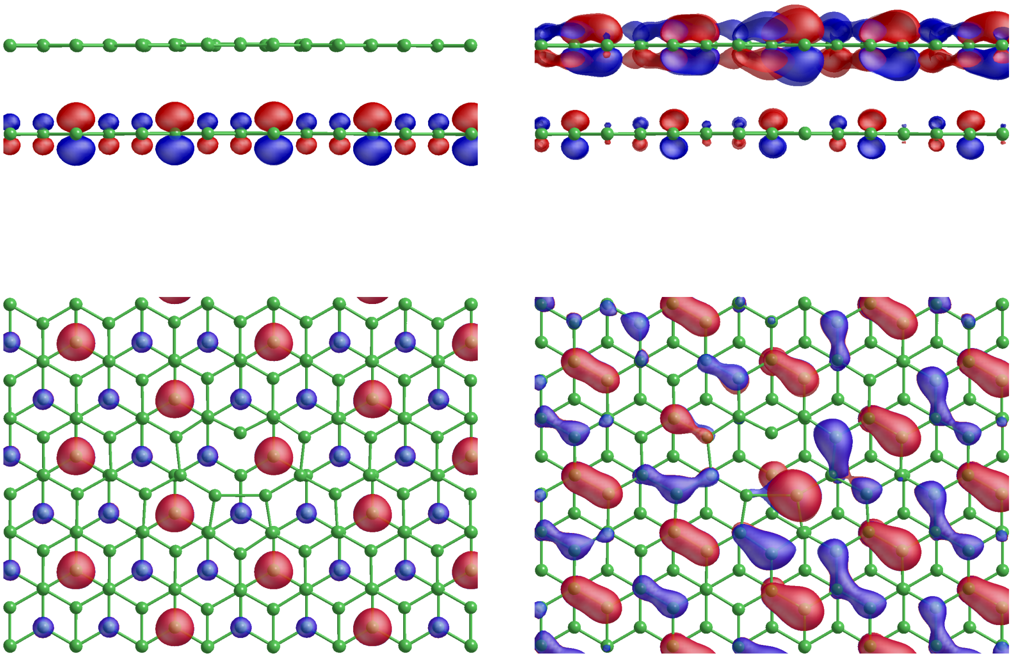

SOMO LUMO

Figure A.16: The frontier orbitals for the spin-polarised mono-vacancy in bi-layer graphene.

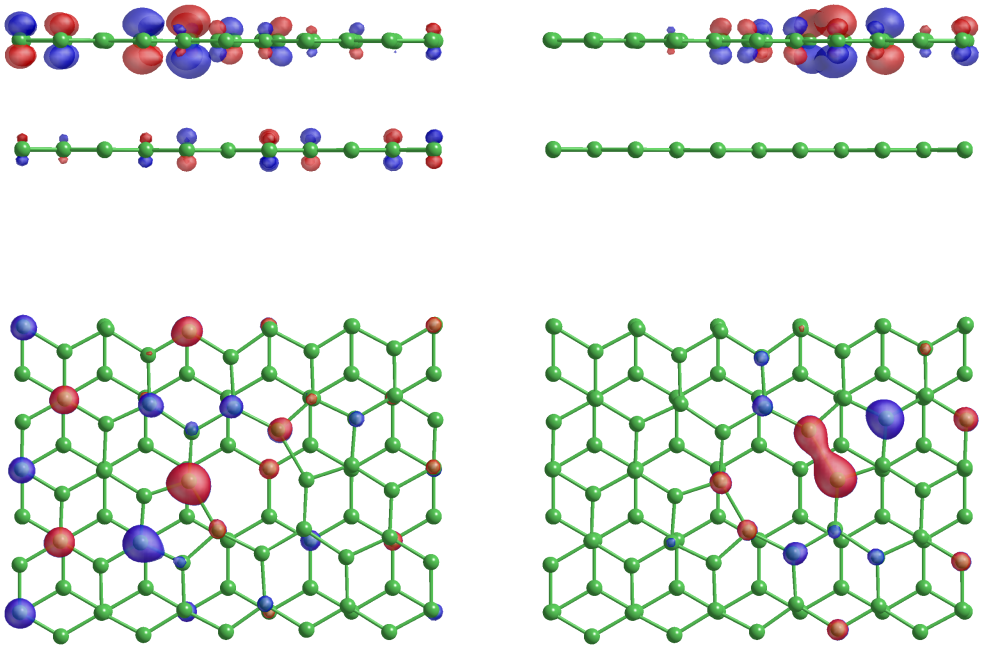

HOMO -1 HOMO

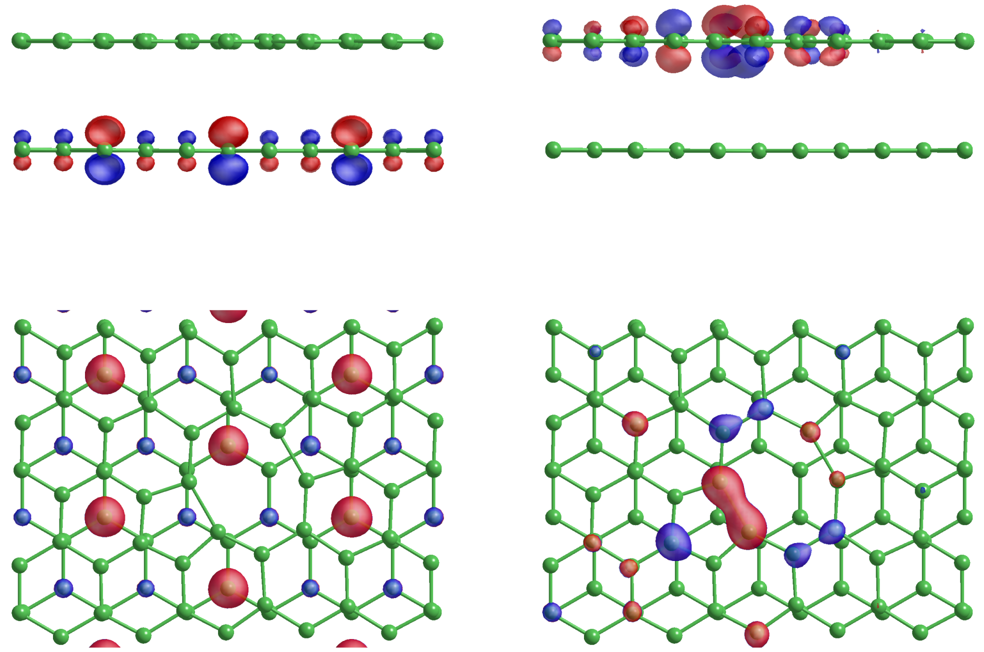

LUMO LUMO +1

Figure A.17: The frontier orbitals for the 1st neighbour di-vacancy in bi-layer graphene.

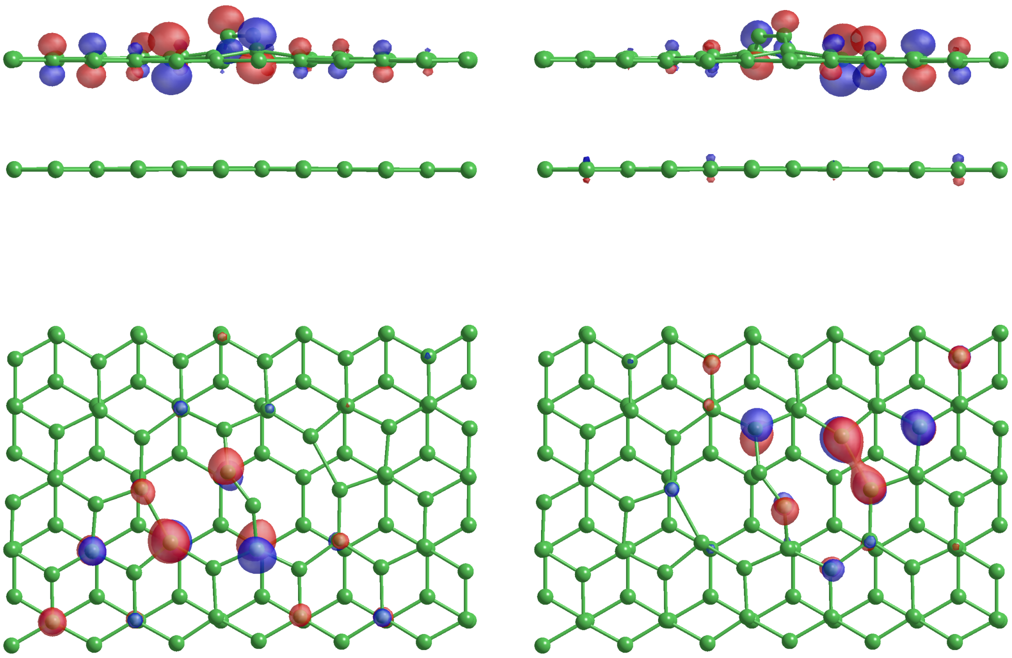

HOMO -1 HOMO

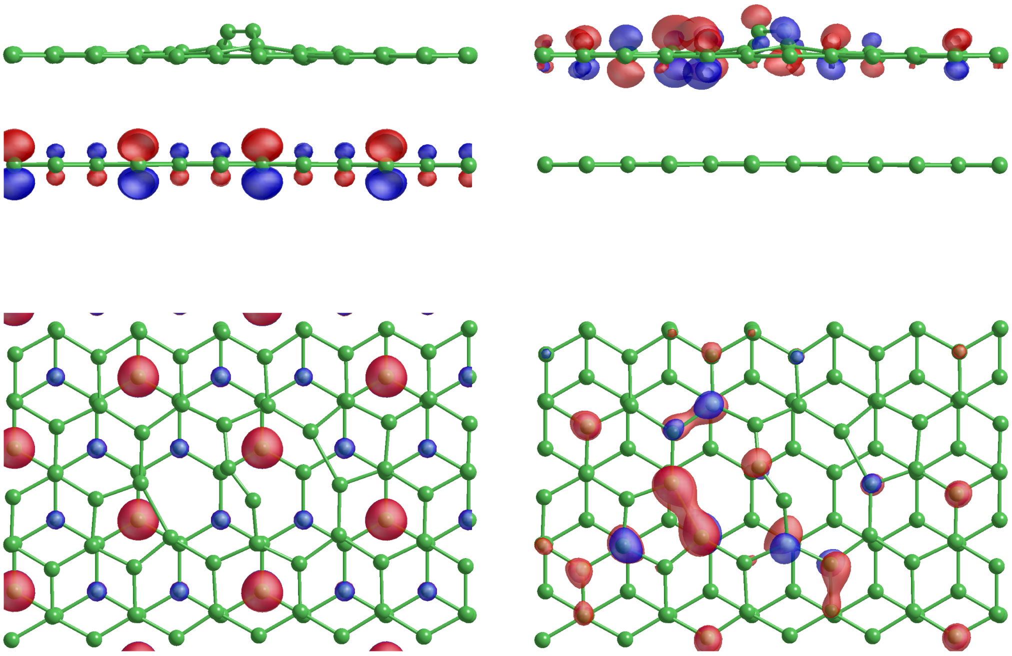

LUMO LUMO +1

Figure A.18: The frontier orbitals for the 3rd neighbour protruding di-vacancy in bi-layer graphene.

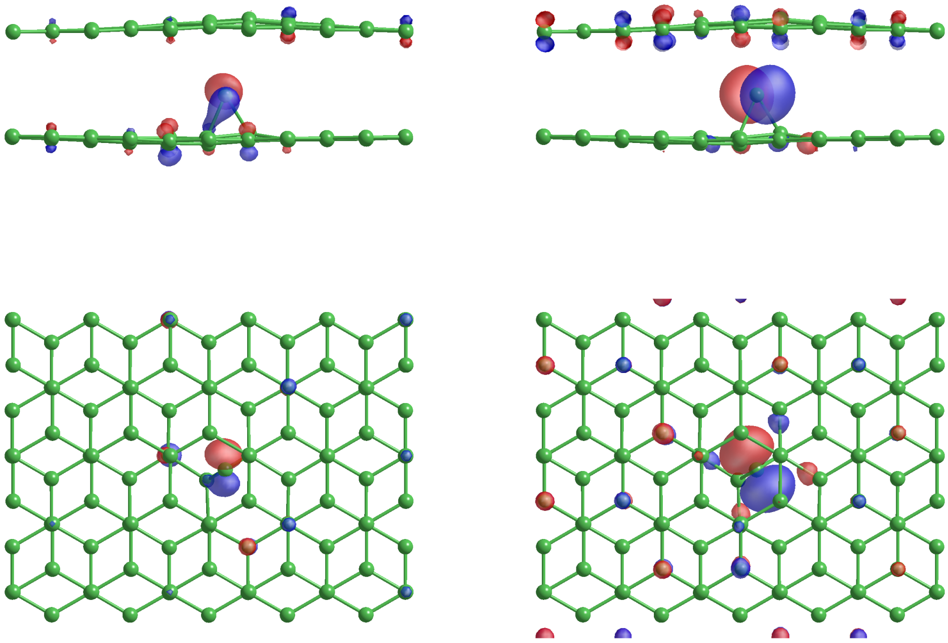

HOMO -1 HOMO

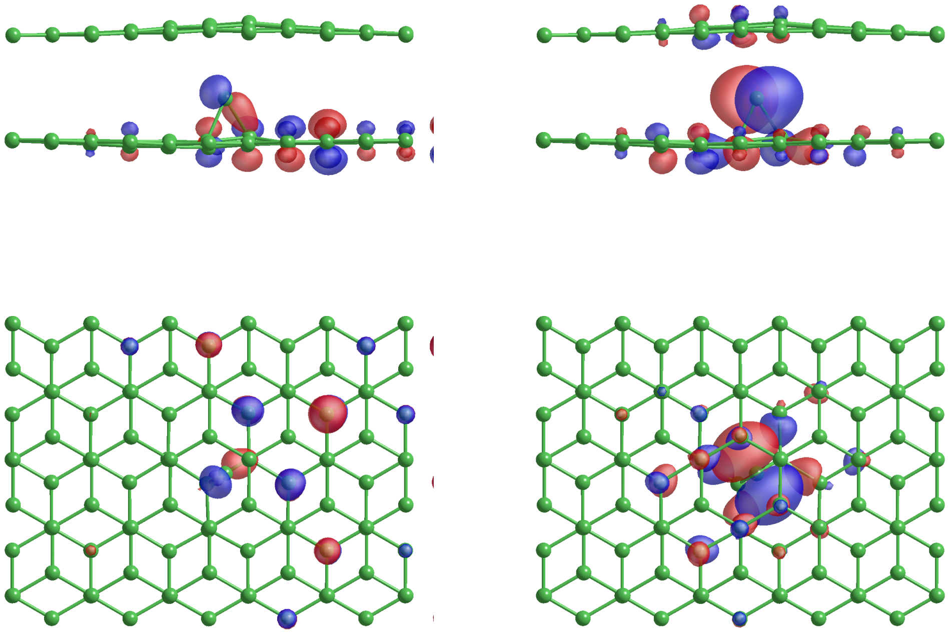

LUMO LUMO +1

Figure A.19: The frontier orbitals for the grafted interstitial in bi-layer graphene.

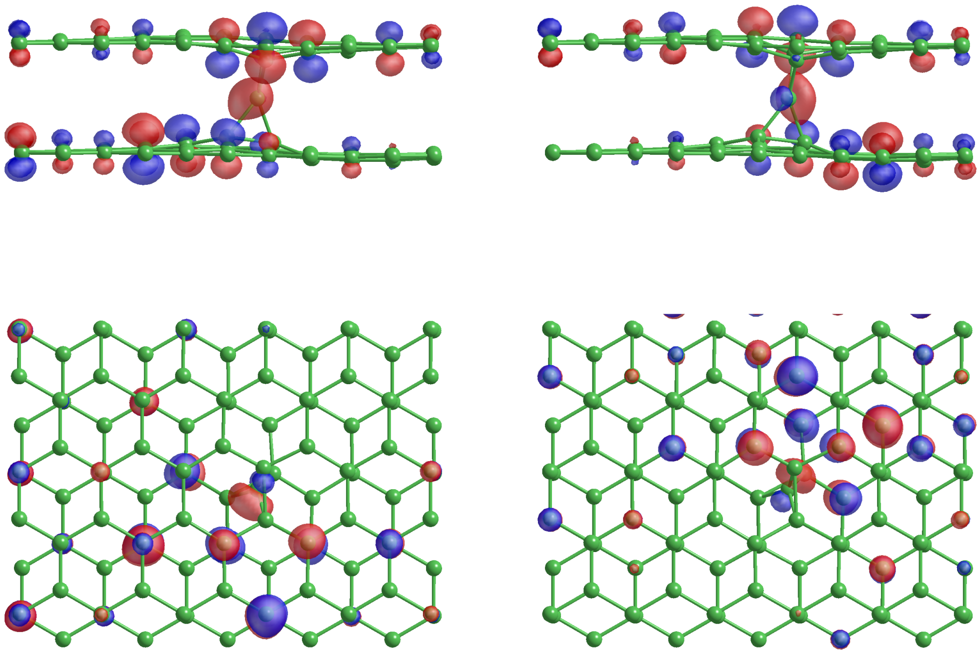

HOMO -1 HOMO

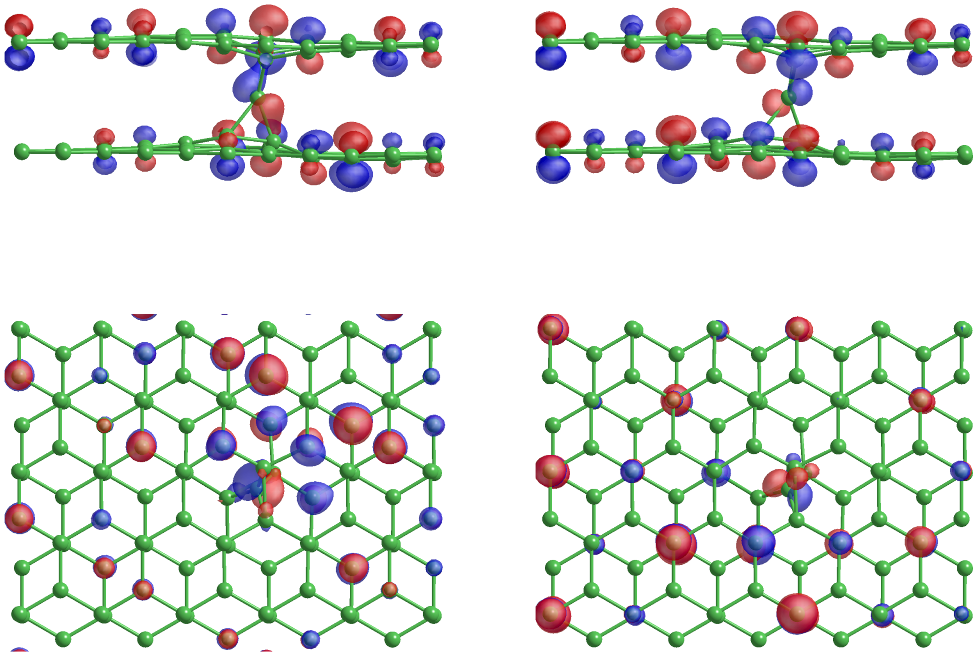

LUMO LUMO +1

Figure A.20: The frontier orbitals for the spiro-bonded interstitial in bi-layer graphene.

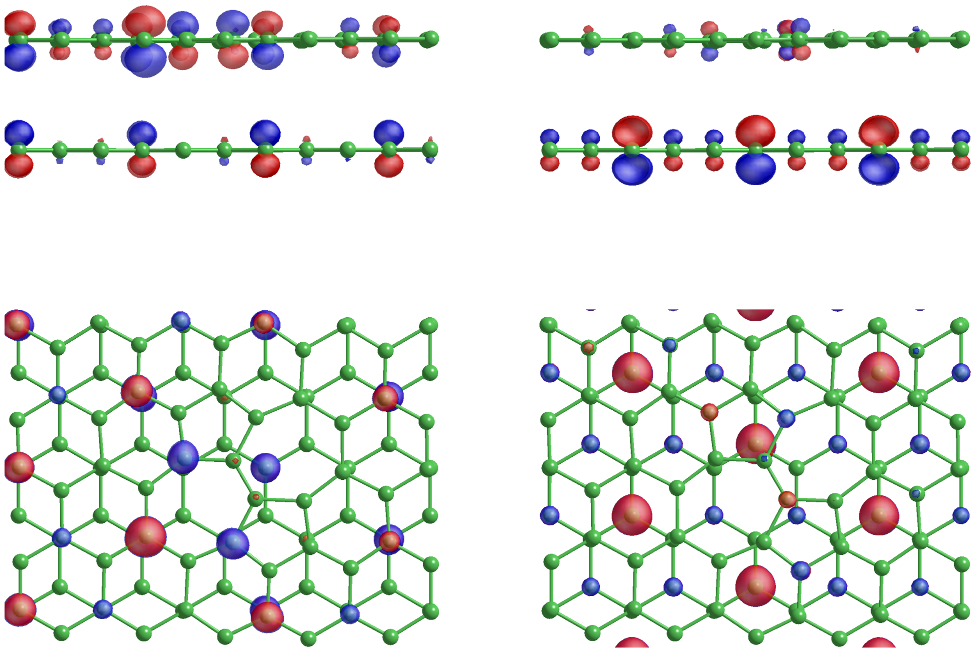

HOMO -1

HOMO

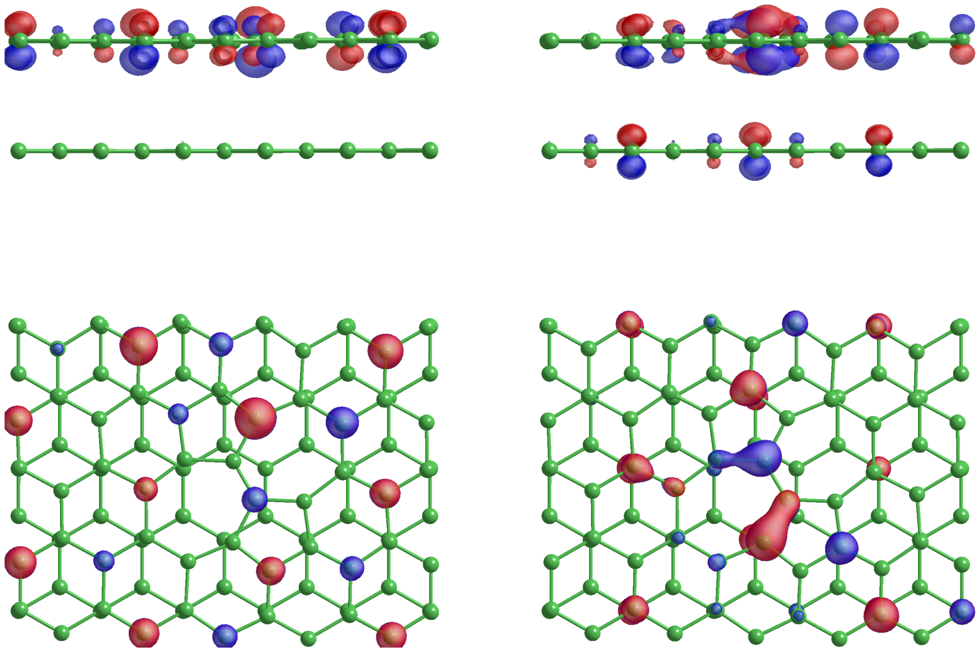

LUMO

LUMO +1

Figure A.21: The frontier orbitals for the Stone-Wales defect in bi-layer graphene.

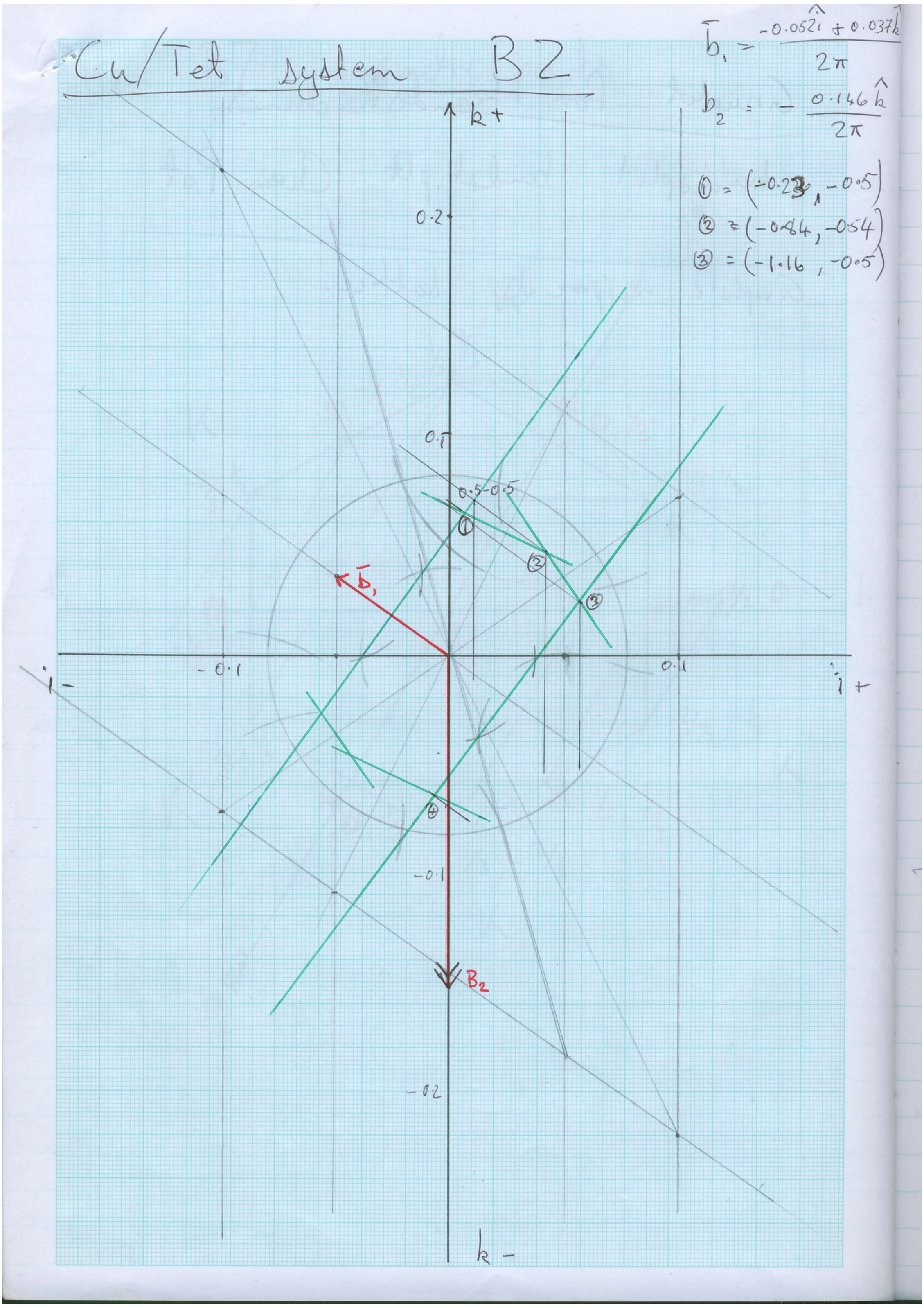

Figure A.22: Construction details for the Brillouin zone of tetracene absorbed on an oxygen-terminated Copper (110) surface, scan 1.

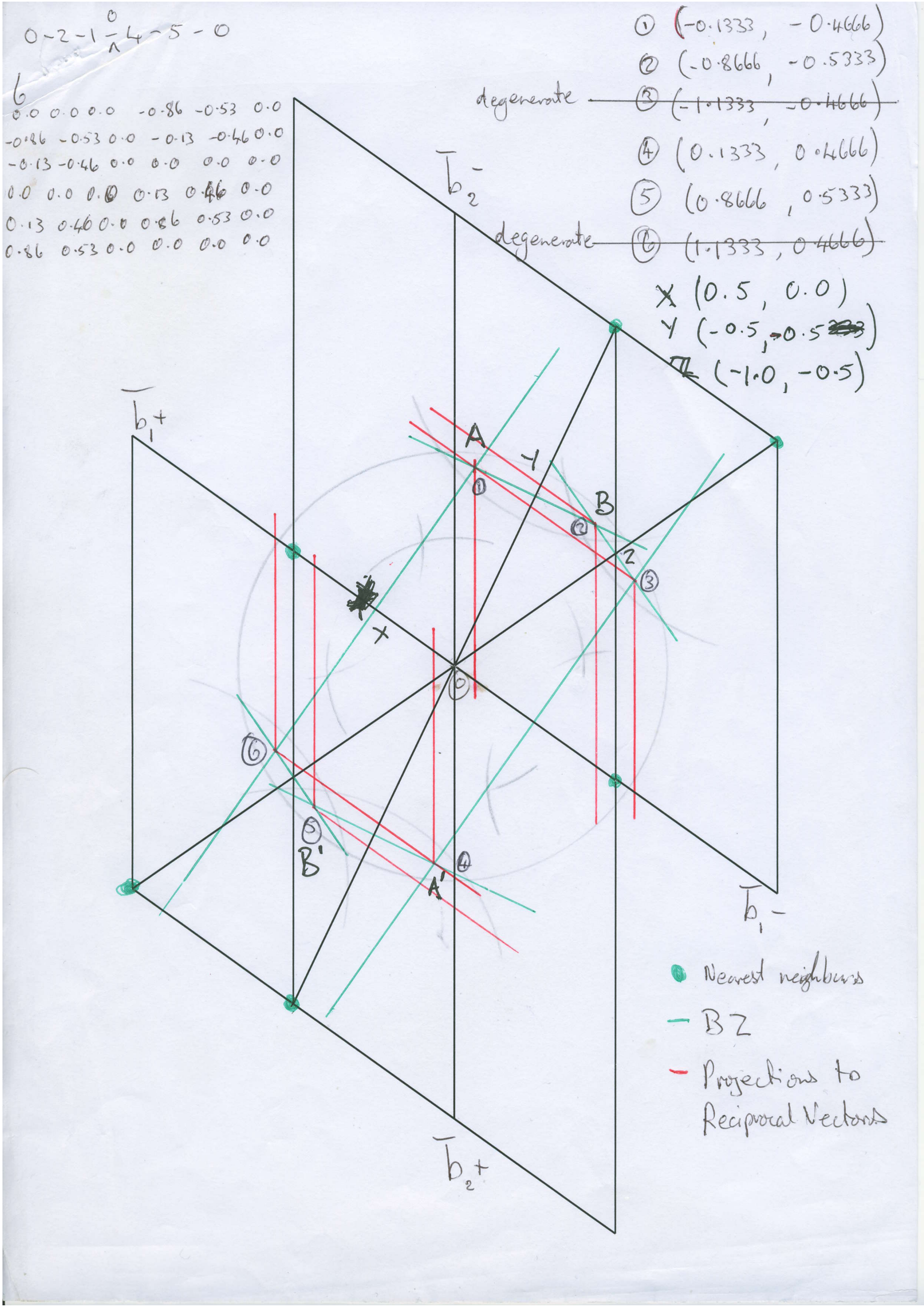

Figure A.23: Construction details for the Brillouin zone of tetracene absorbed on an oxygen-terminated Copper (110) surface, scan 2.

Appendix B

Bandstructures

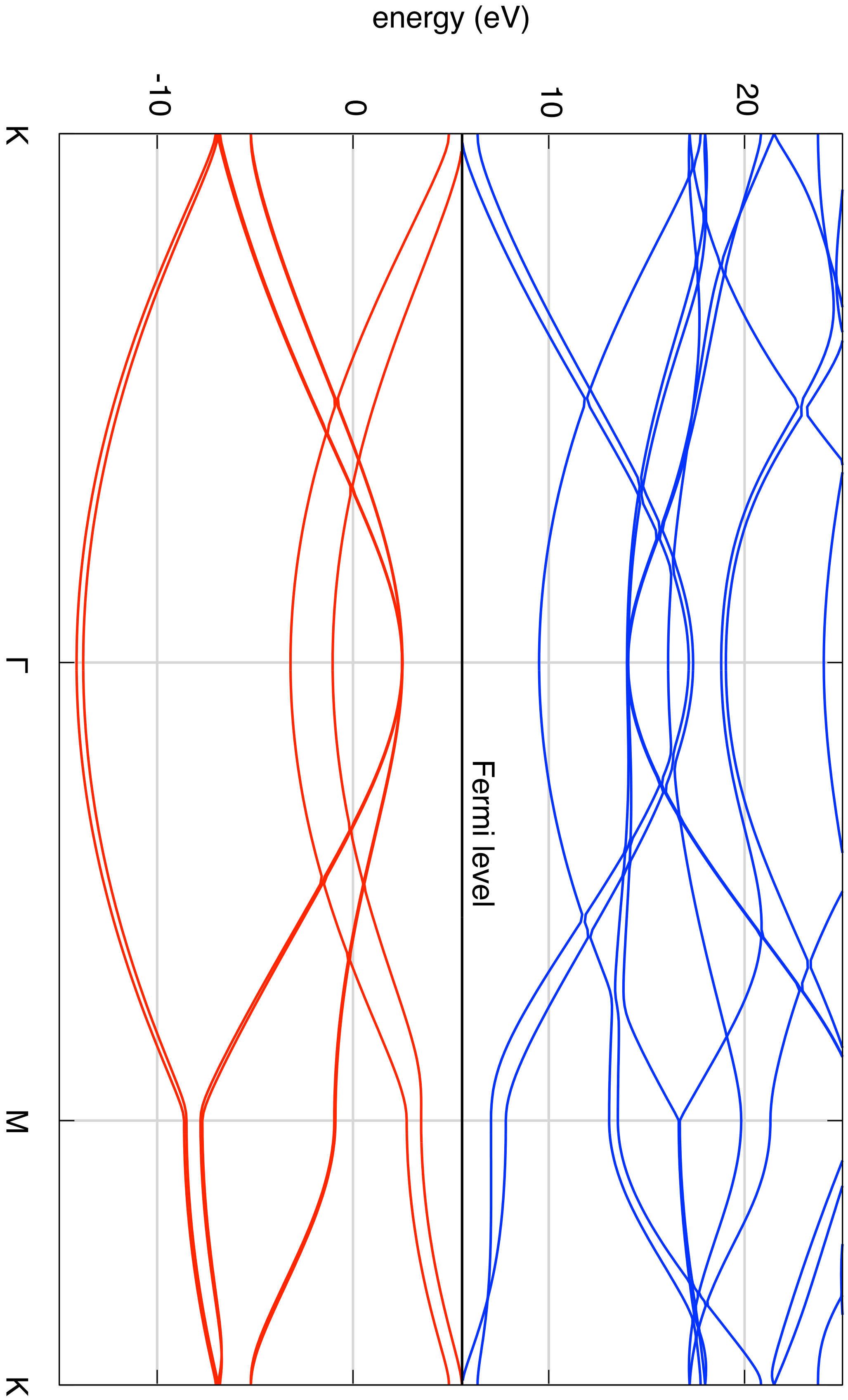

Figure B.1: The bandstructure of A-B stacked graphite.

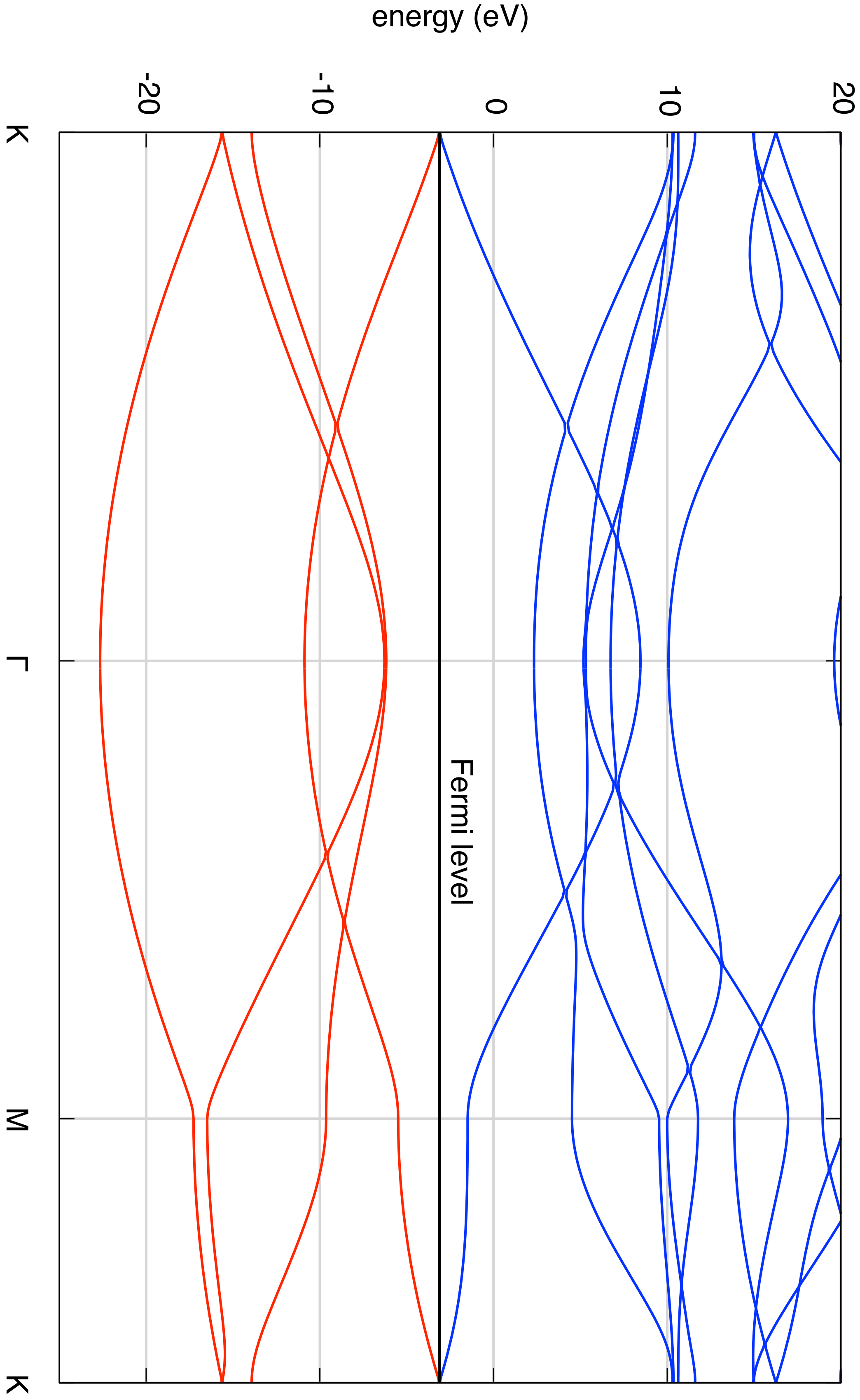

Figure B.2: The bandstructure of graphene.

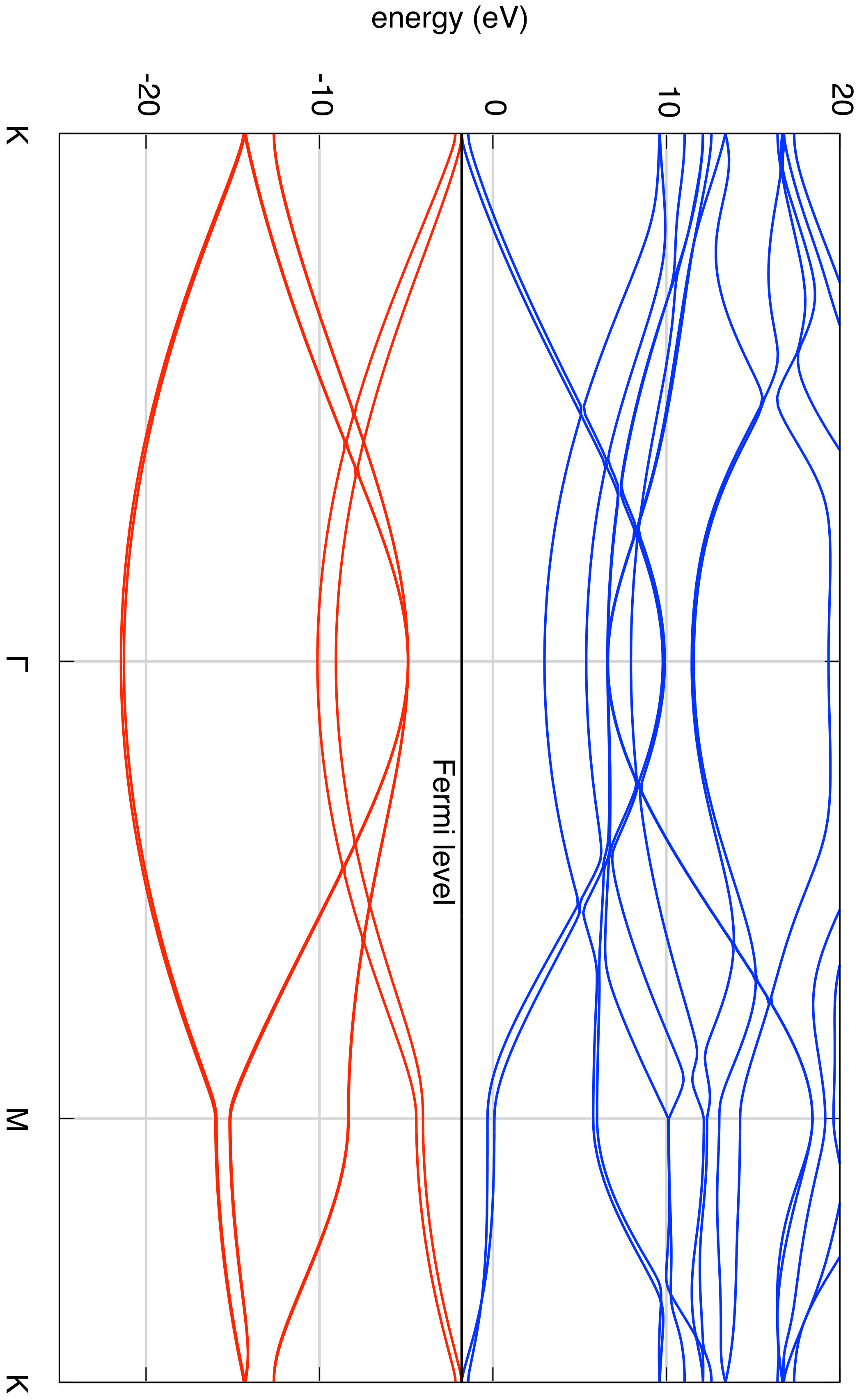

Figure B.3: The bandstructure of bi-layer graphene.

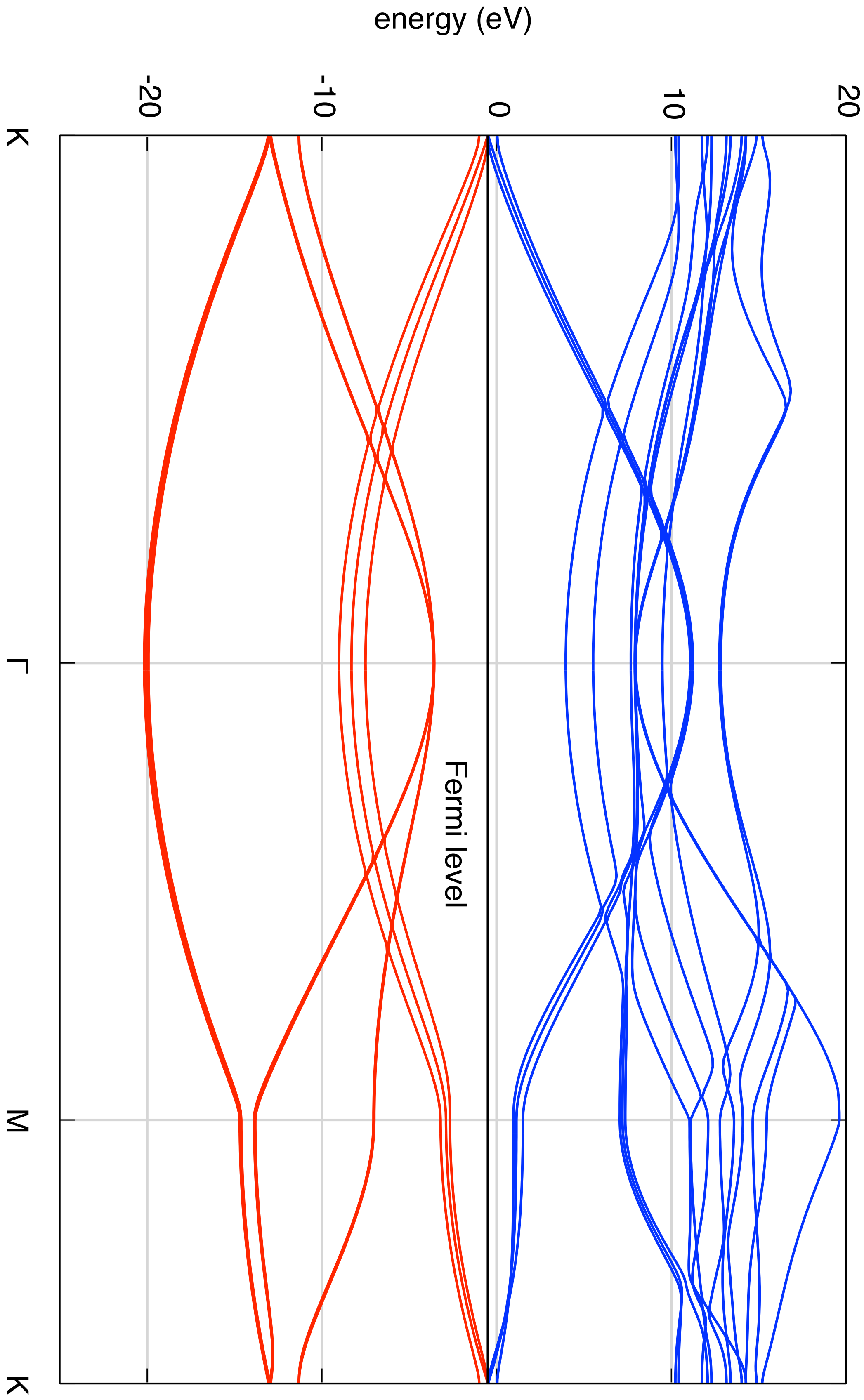

Figure B.4: The bandstructure of tri-layer graphene.

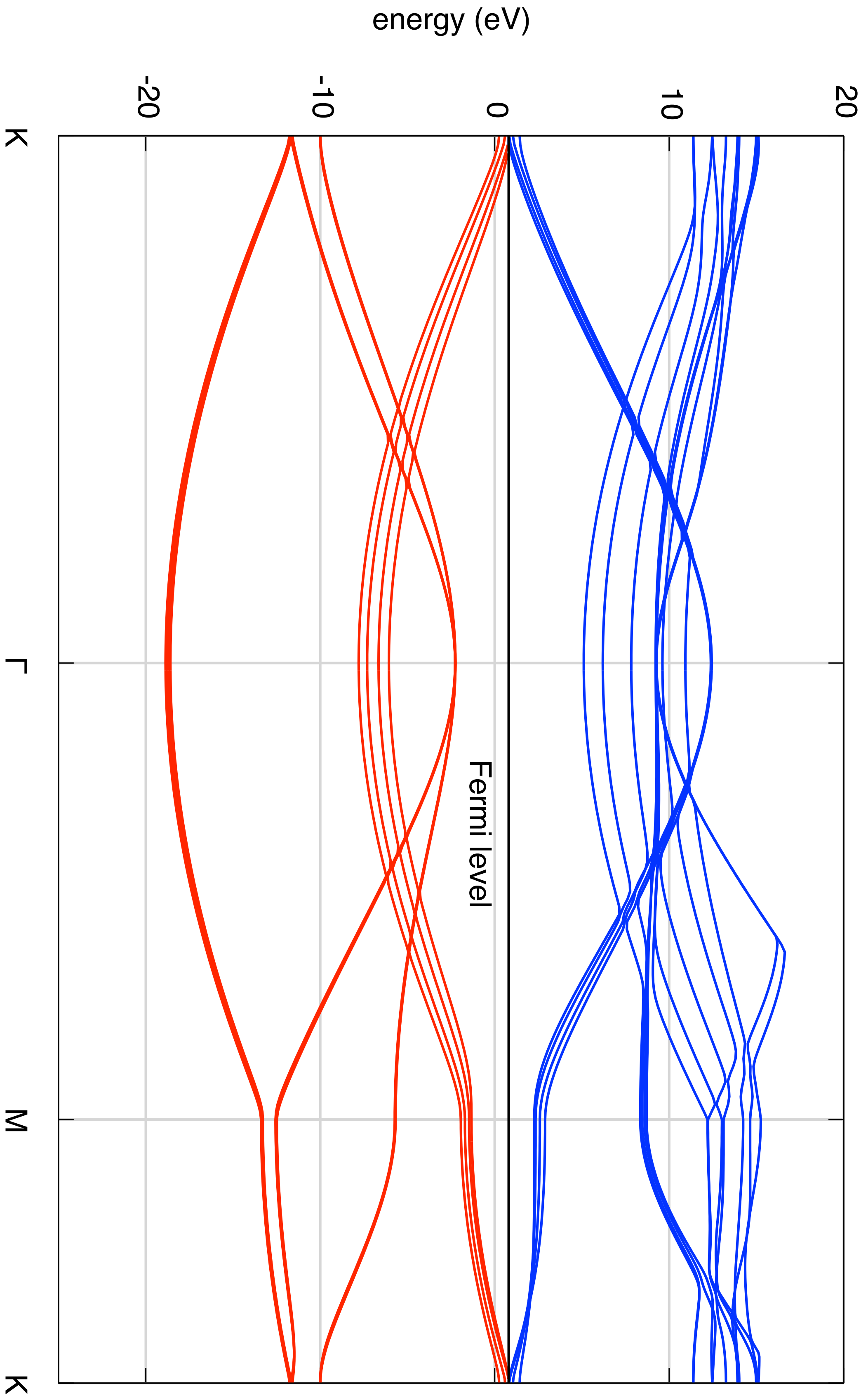

Figure B.5: The bandstructure of quad-layer graphene.

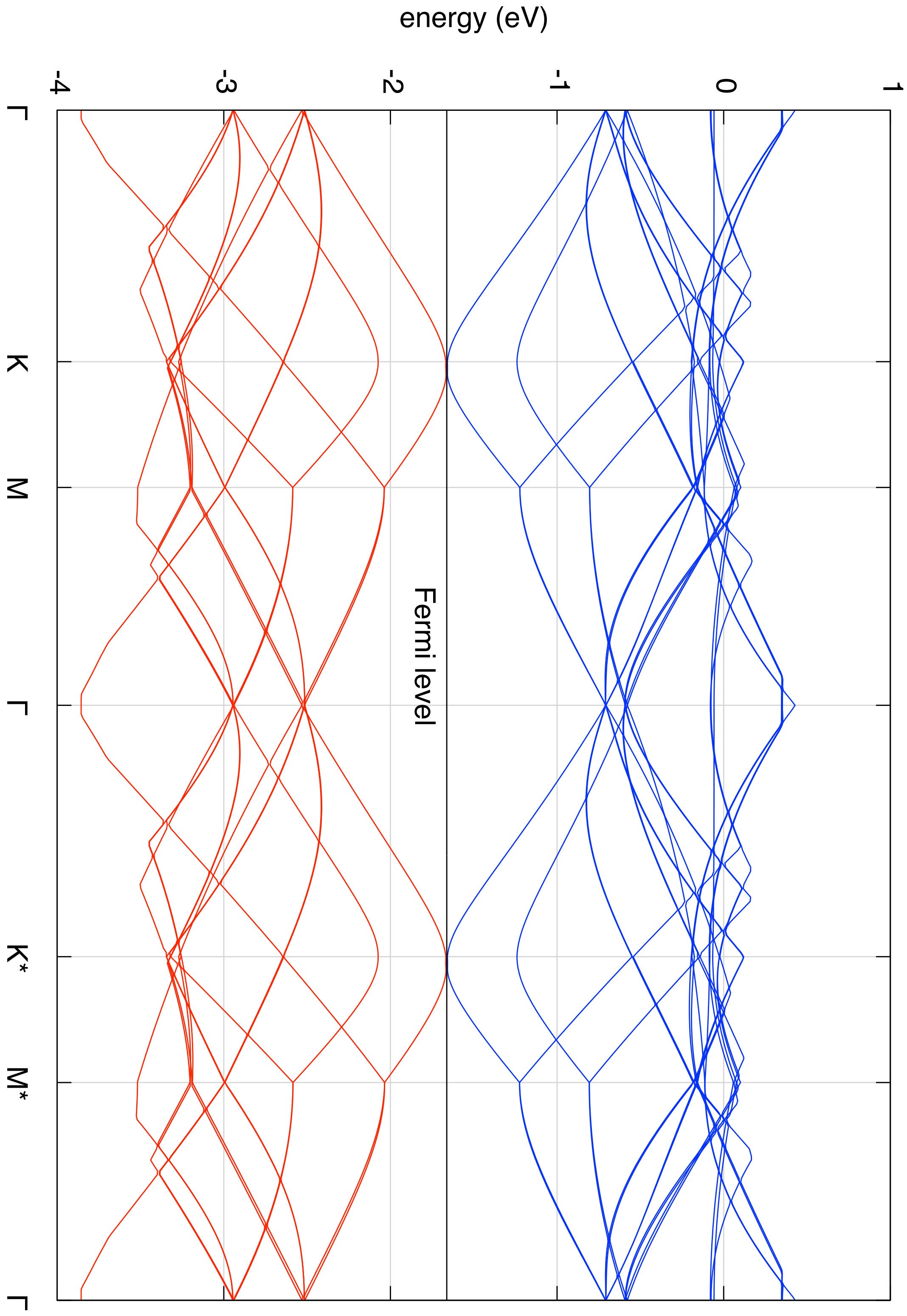

Figure B.6: The bandstructure of pristine, bi-layer graphene, levels 500-531.

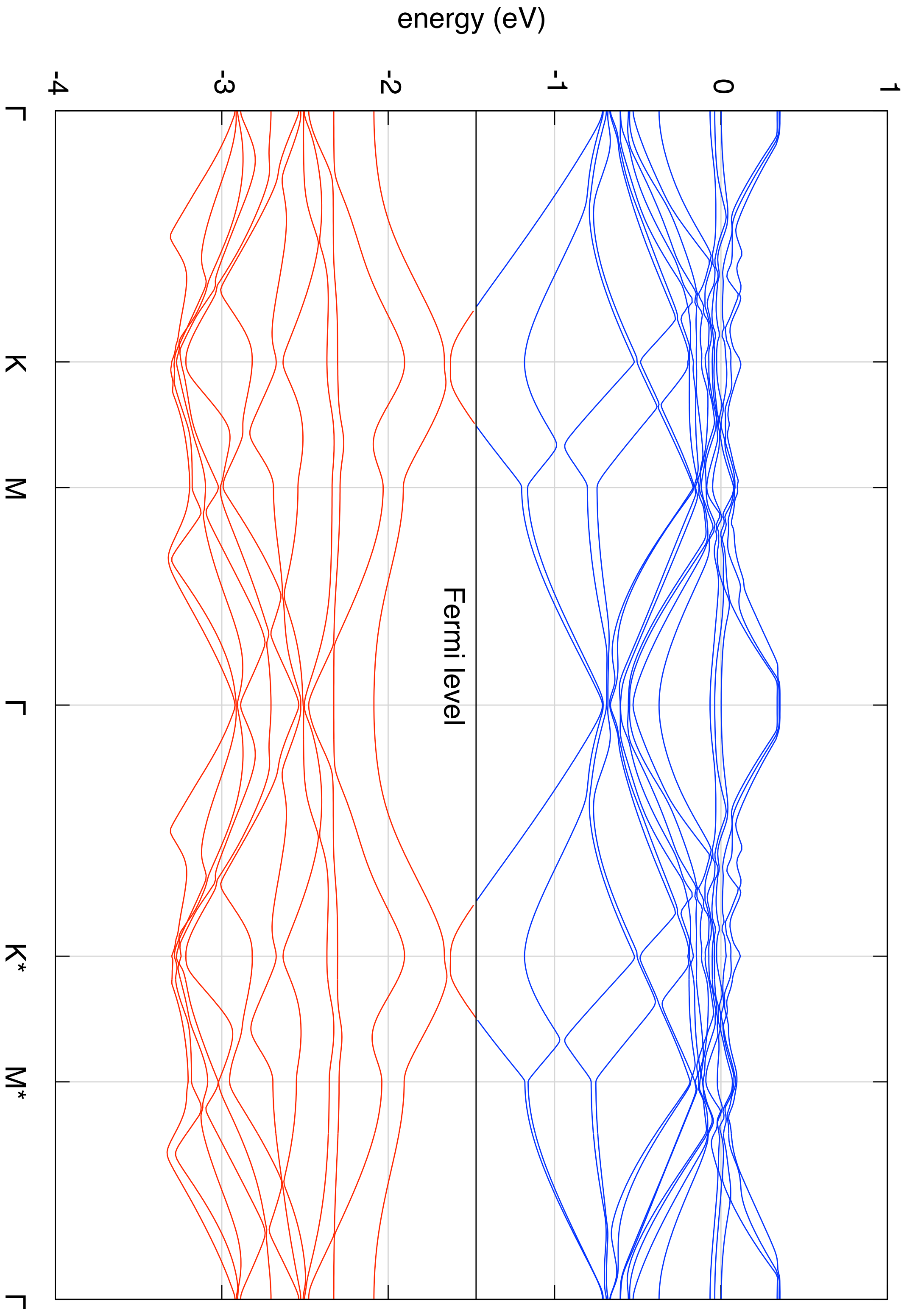

Figure B.7: The spin-up bandstructure for the mono-vacancy in bi-layer graphene, levels 500-529.

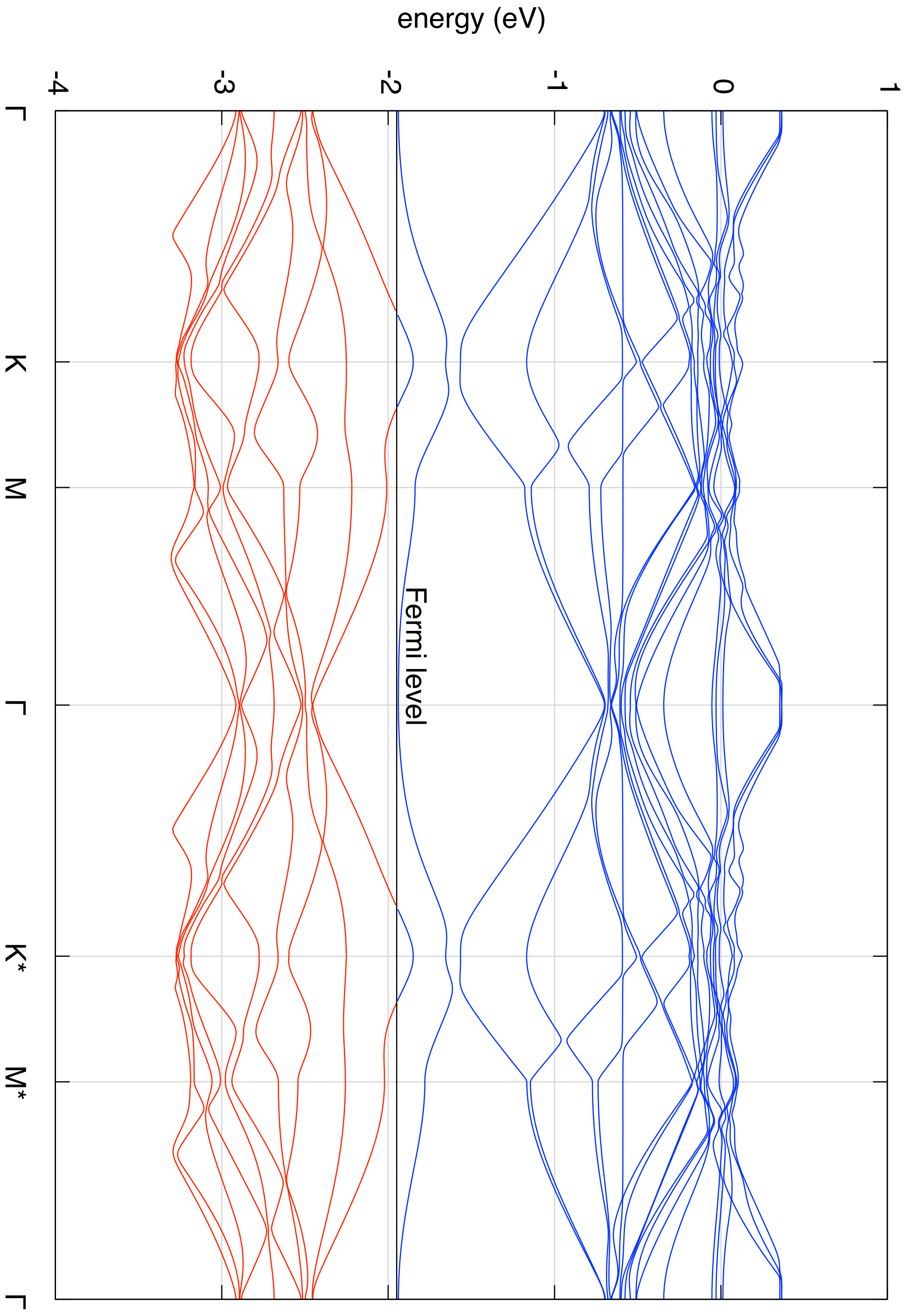

Figure B.8: The spin-down bandstructure for the mono-vacancy in bi-layer graphene, levels 500-529.

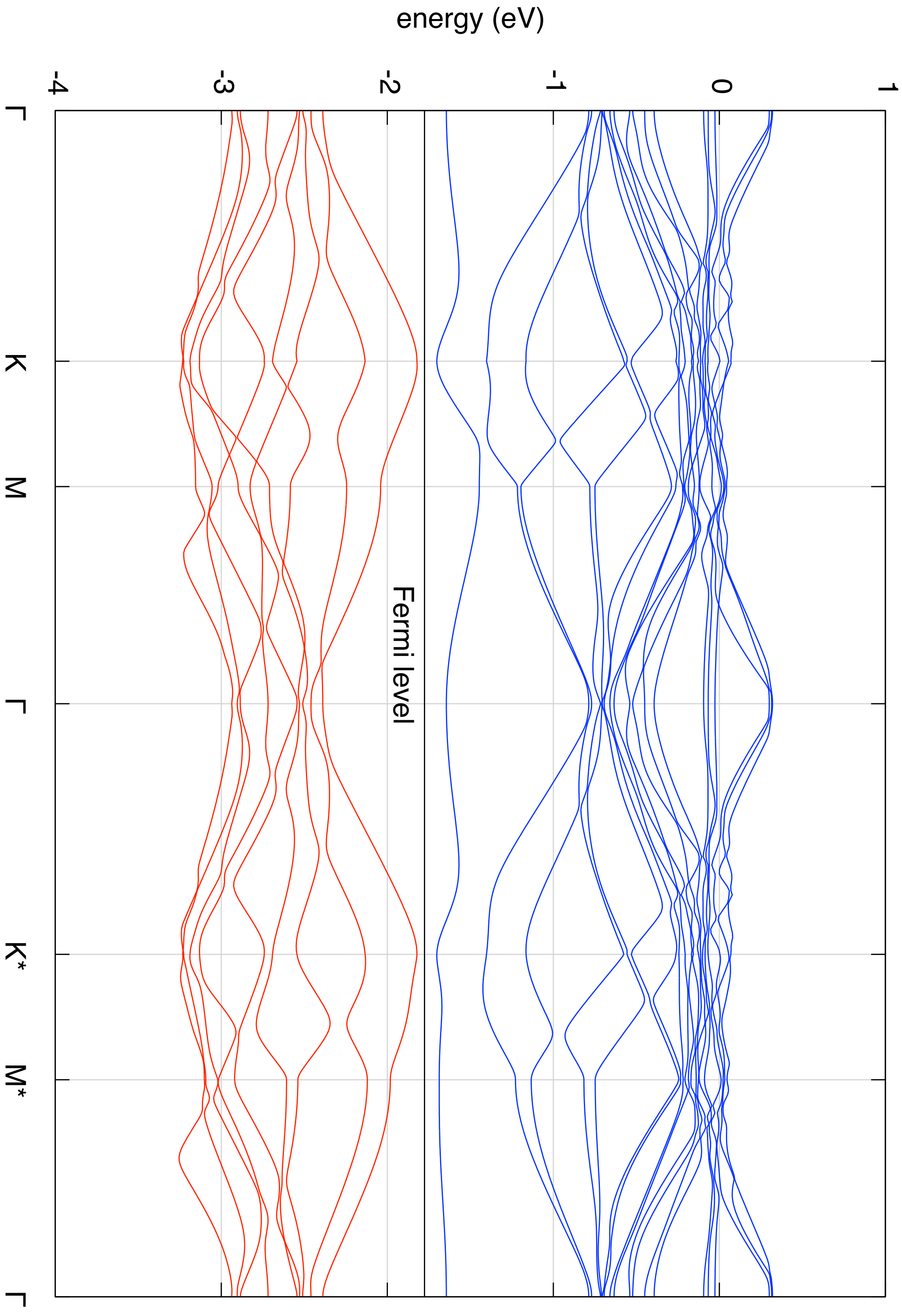

Figure B.9: The bandstructure for the 1st neighbour di-vacancy in bi-layer graphene, levels 500-527.

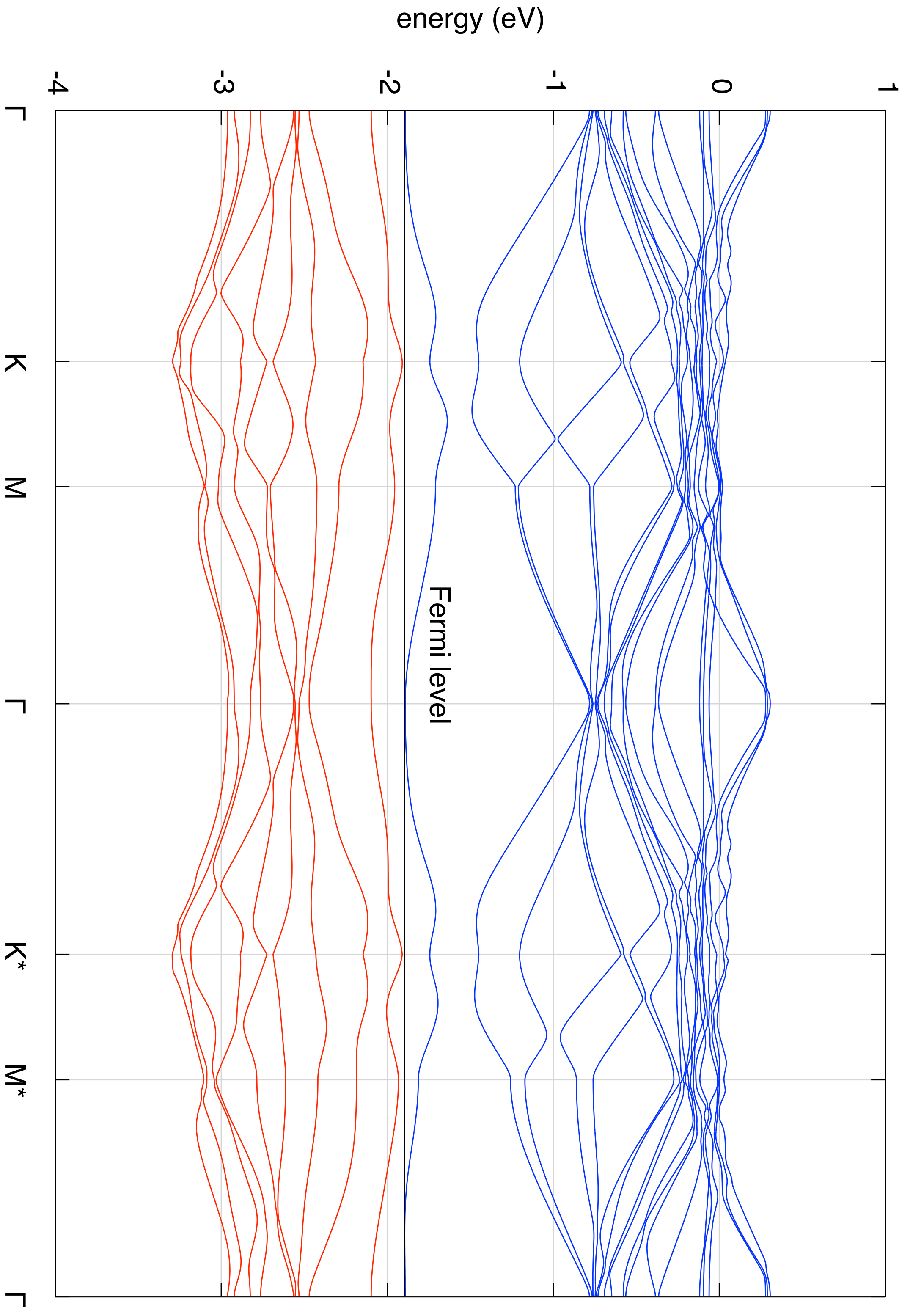

Figure B.10: The bandstructure for the 3rd neighbour protruding di-vacancy in bi-layer graphene, levels 500-527.

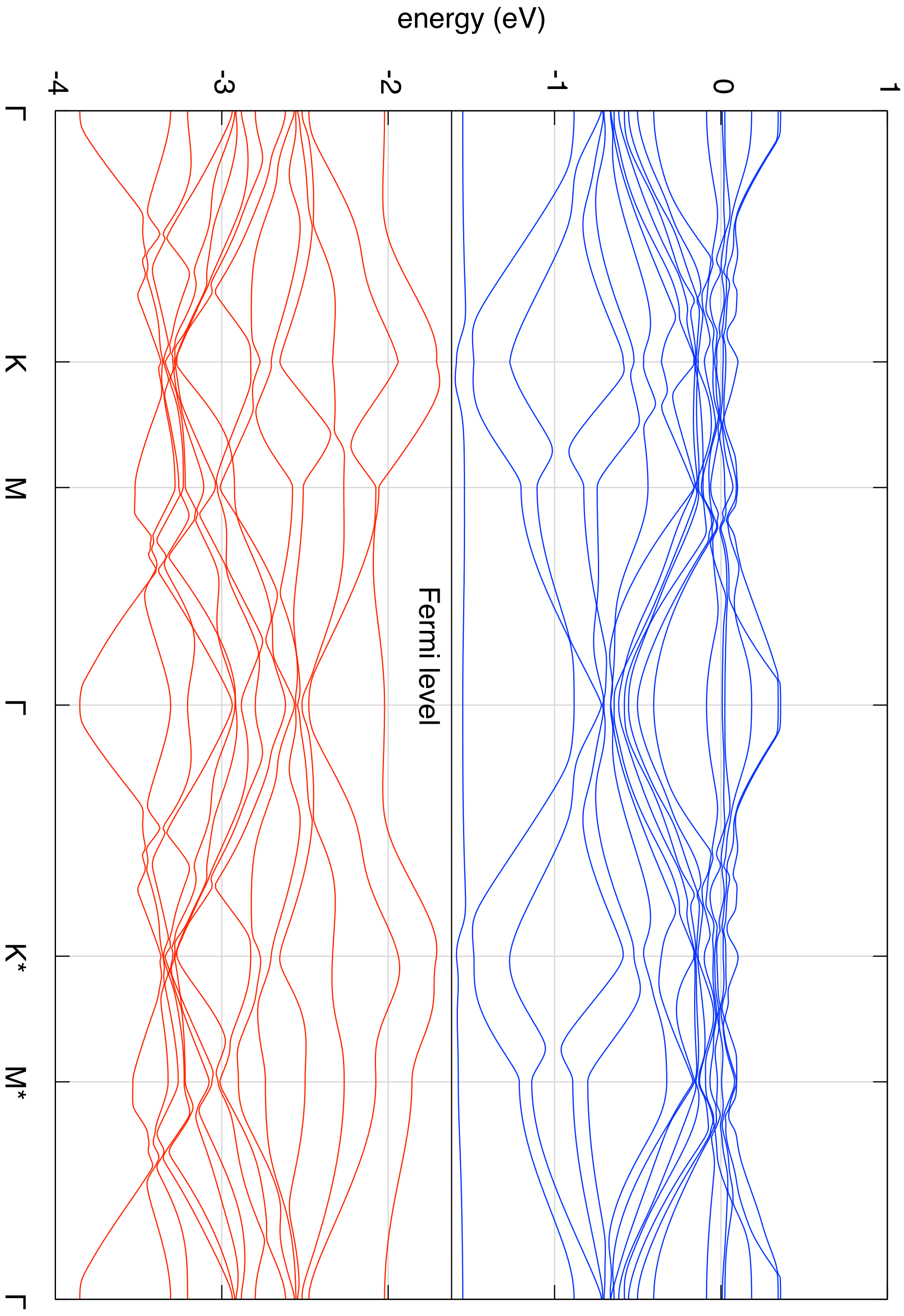

Figure B.11: The bandstructure for the grafted interstitial in bi-layer graphene, levels 500-533.

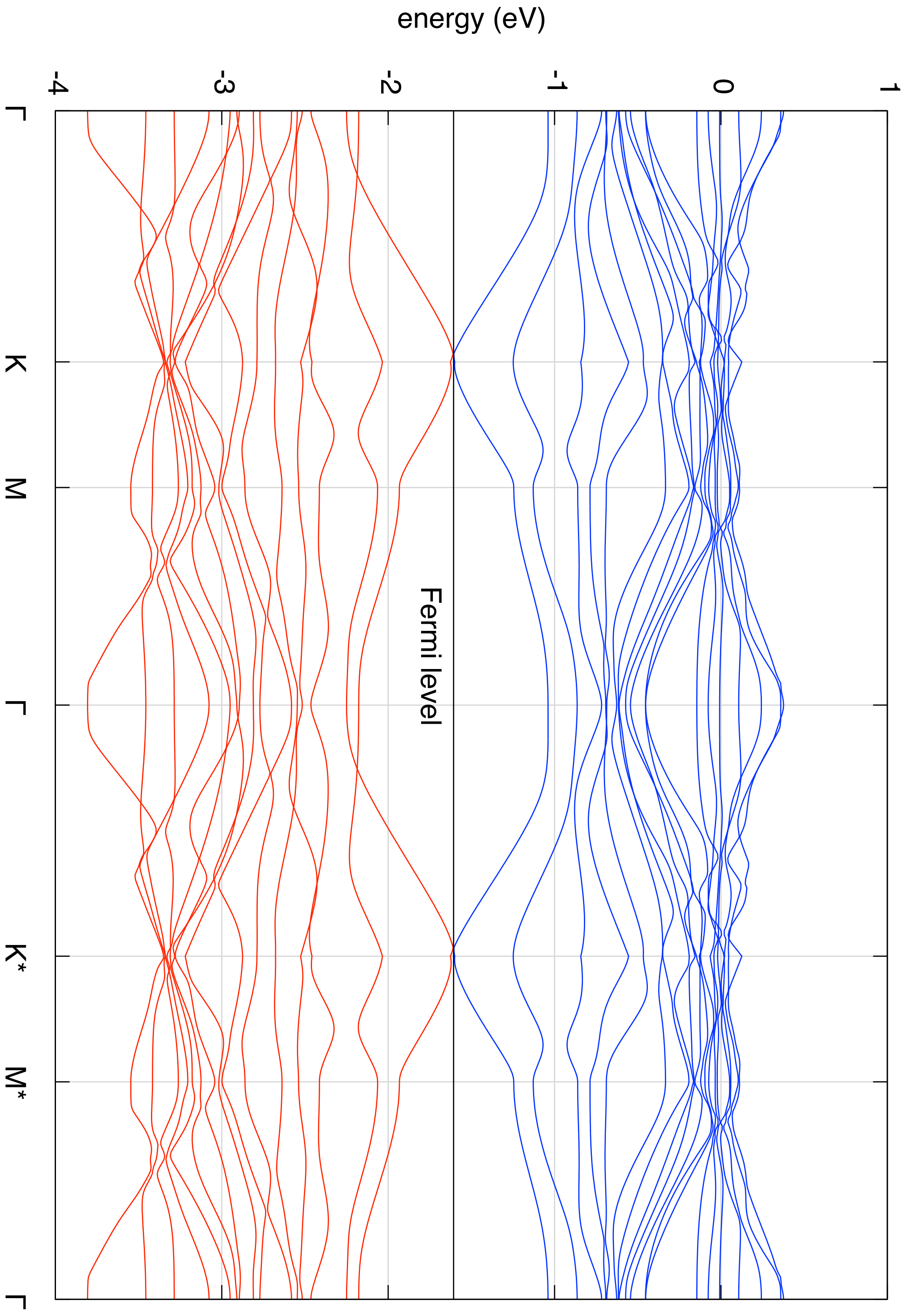

Figure B.12: The bandstructure for the spiro-bonded interstitial in bi-layer graphene, levels 500-533.

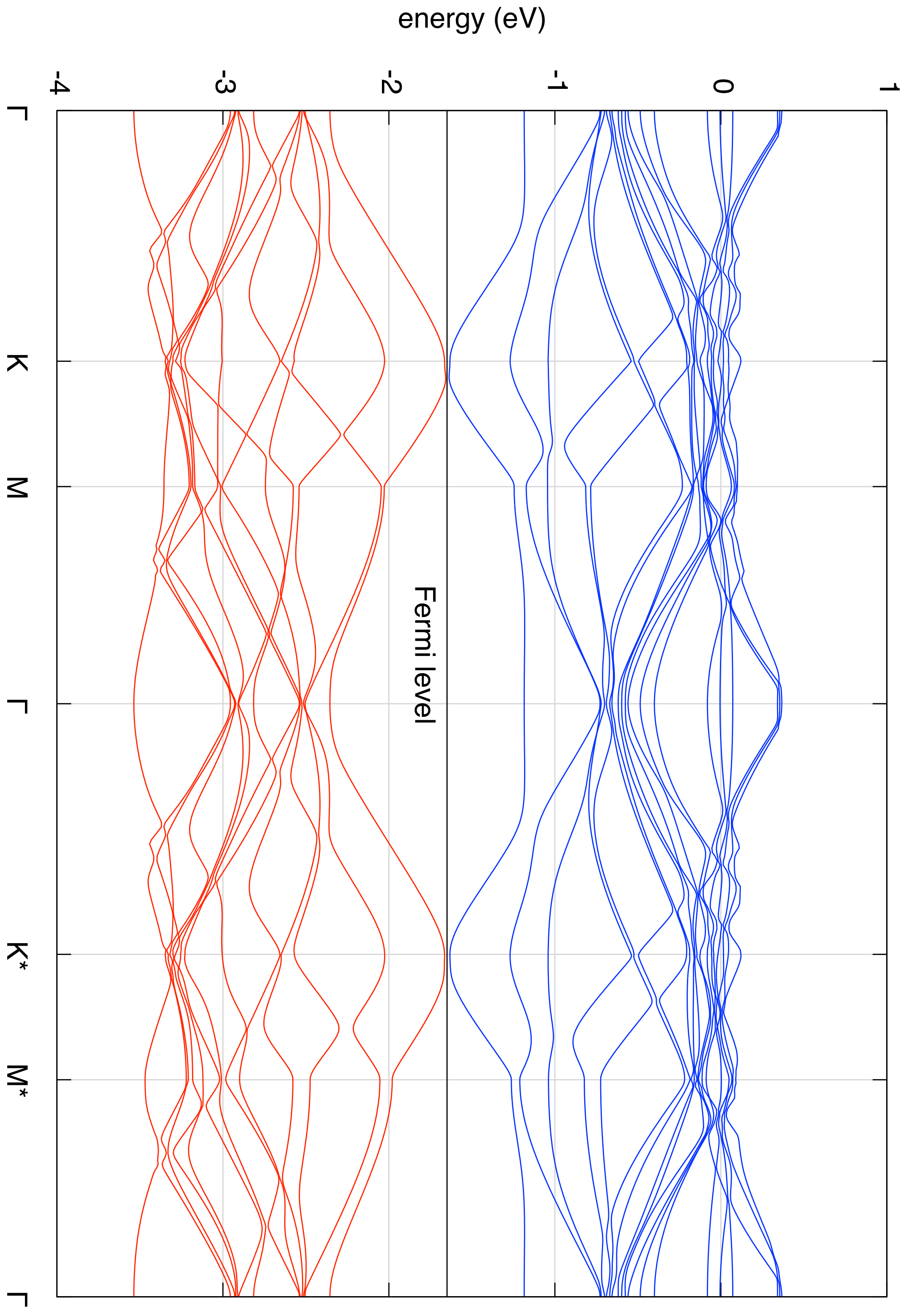

Figure B.13: The bandstructure for the Stone-Wales defect in bi-layer graphene, levels 500-531.

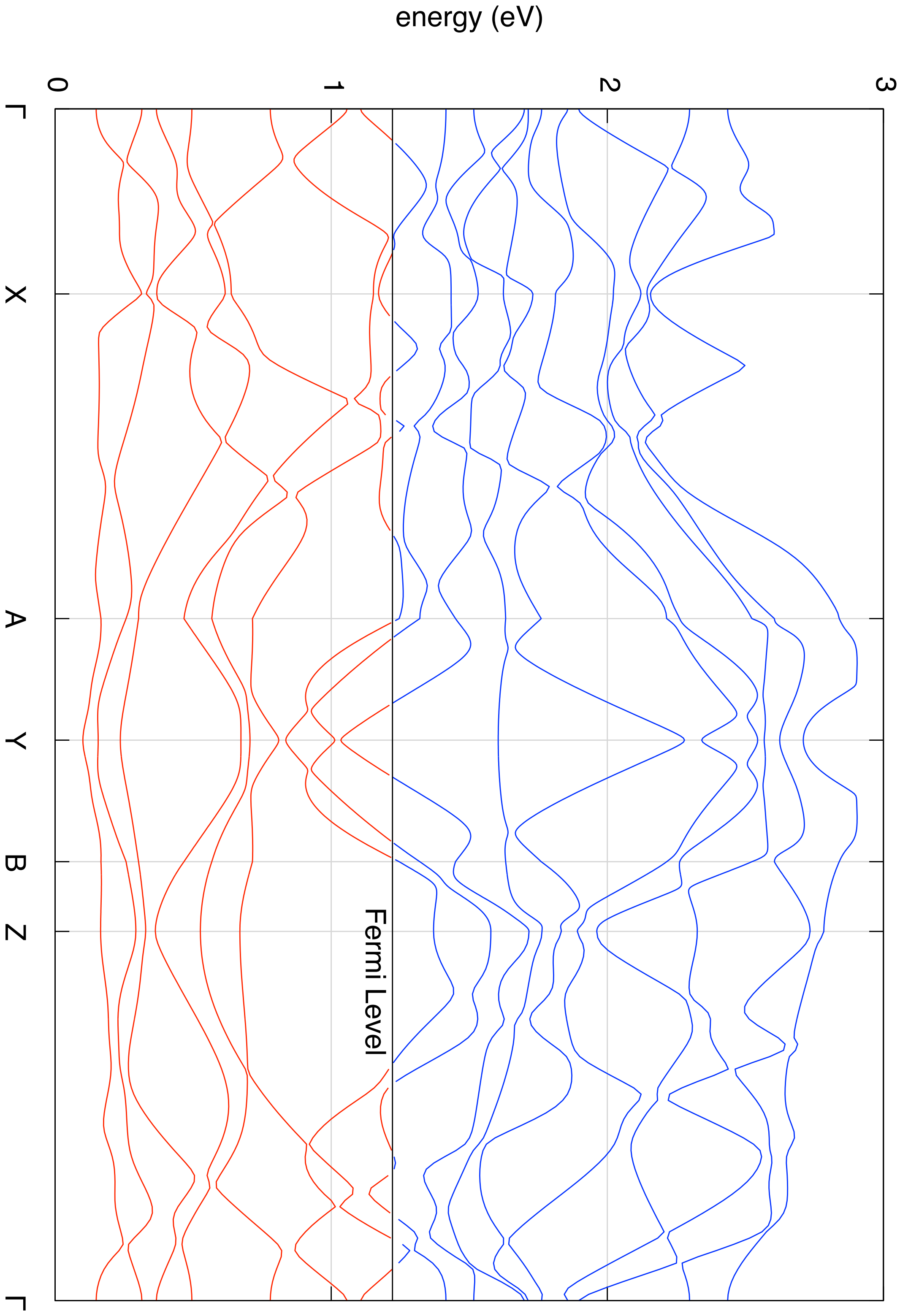

Figure B.14: The bandstructure for tetracene adsorbed on the oxygen terminated, reconstructed row Copper (110) surface, levels 246-261.

Appendix C

Simulated Scanning Tunneling Micrographs

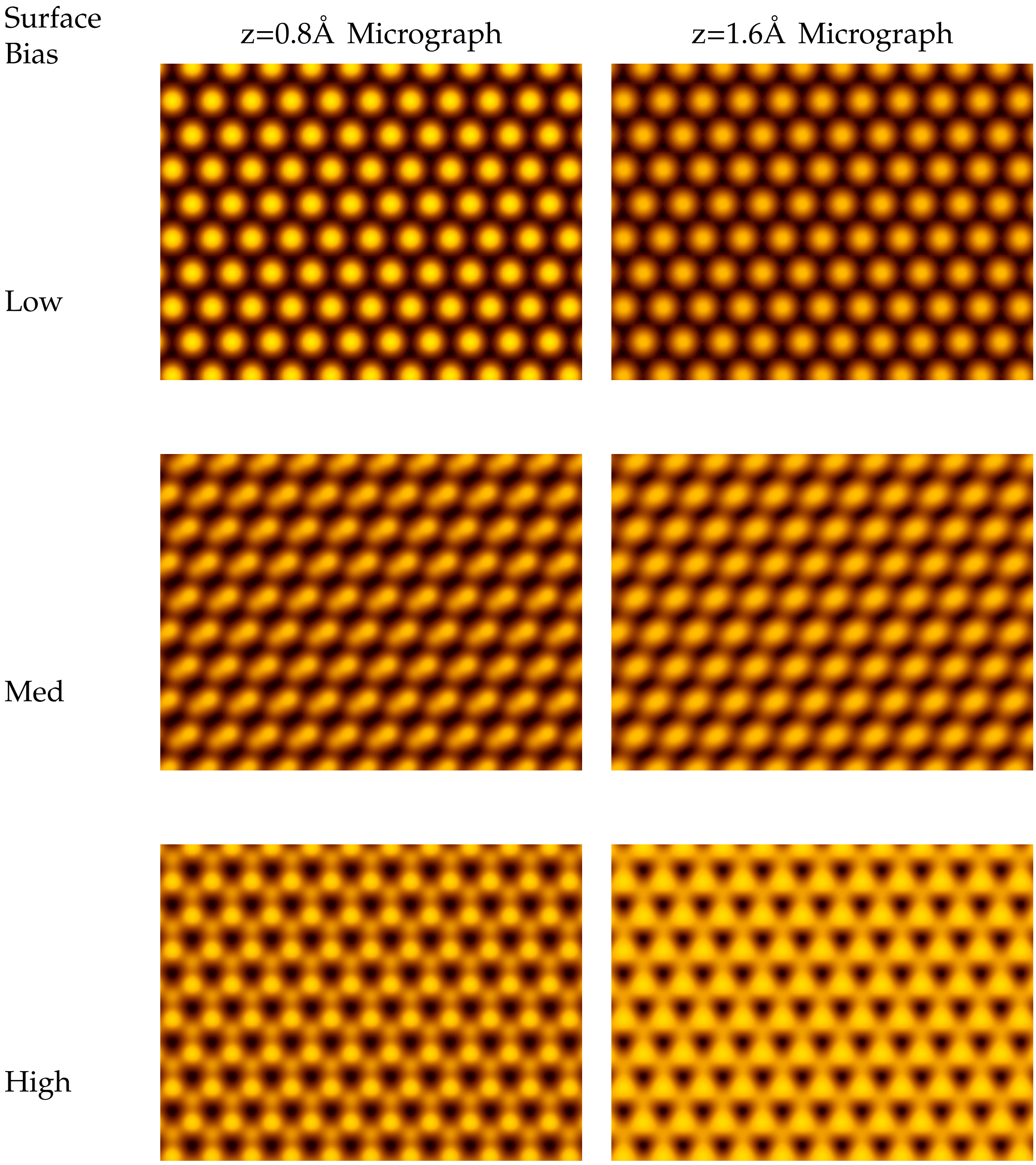

Figure C.1: The simulated scanning tunneling micrographs for the pristine bi-layer graphene surface.

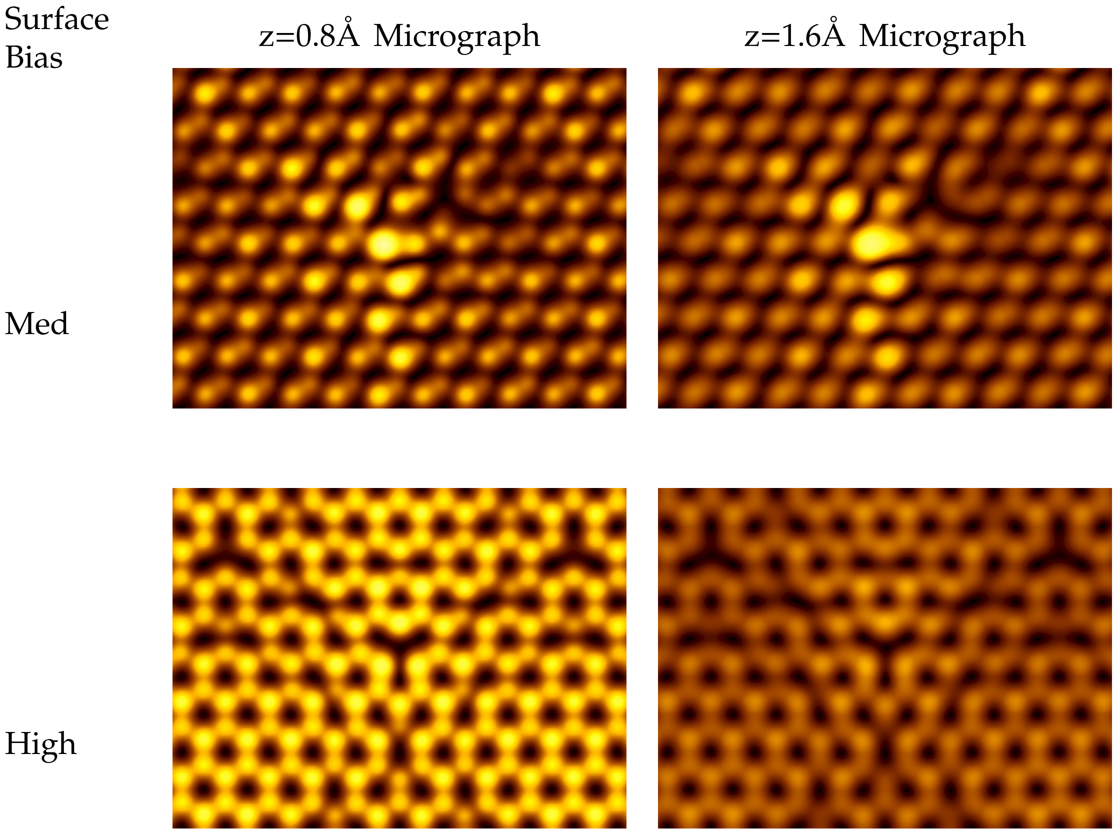

Figure C.2: The simulated scanning tunneling micrographs for the mono-vacancy in bi-layer graphene.

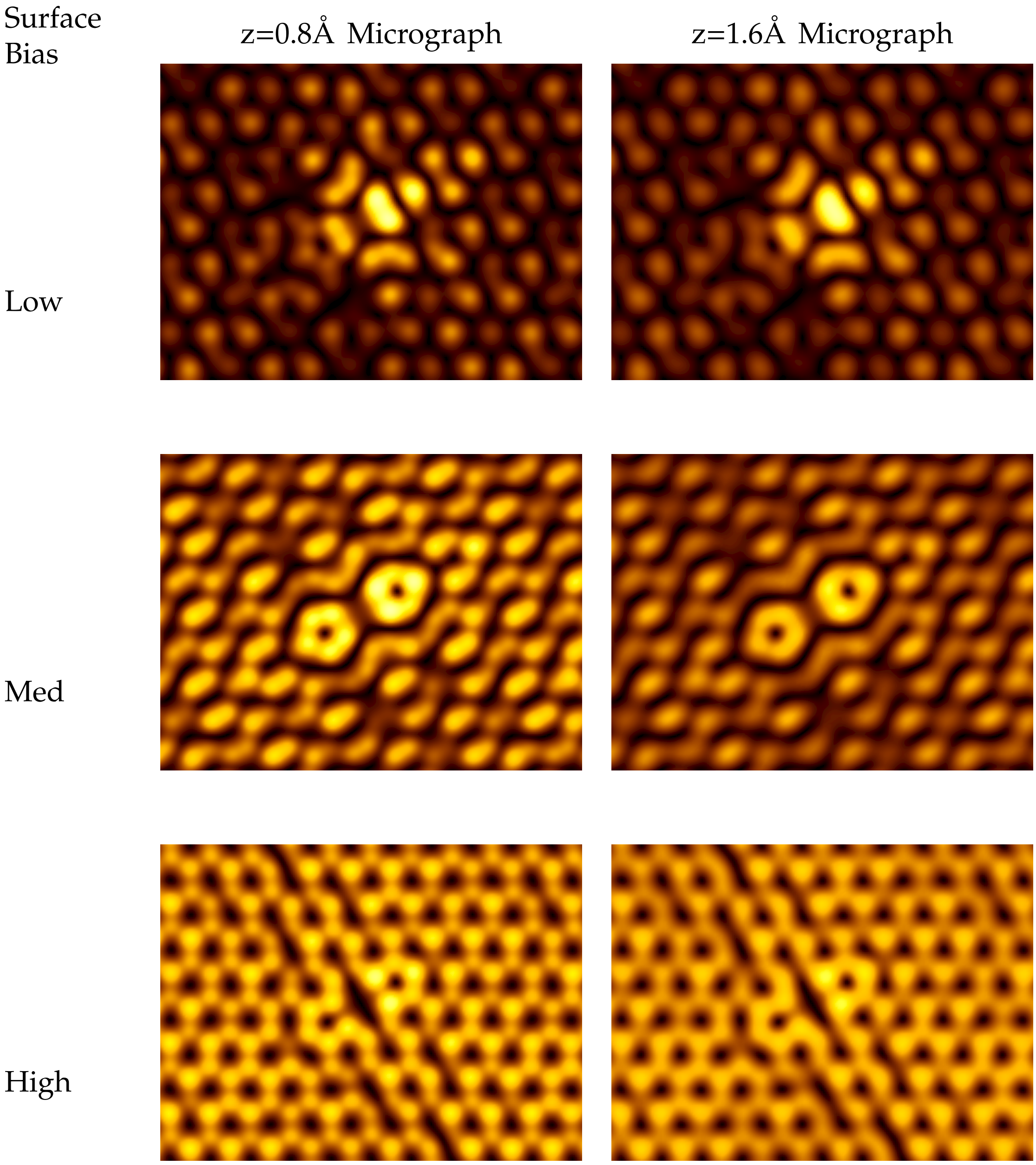

Figure C.3: The simulated scanning tunneling micrographs for the 1st neighbour di-vacancy in bi-layer graphene.

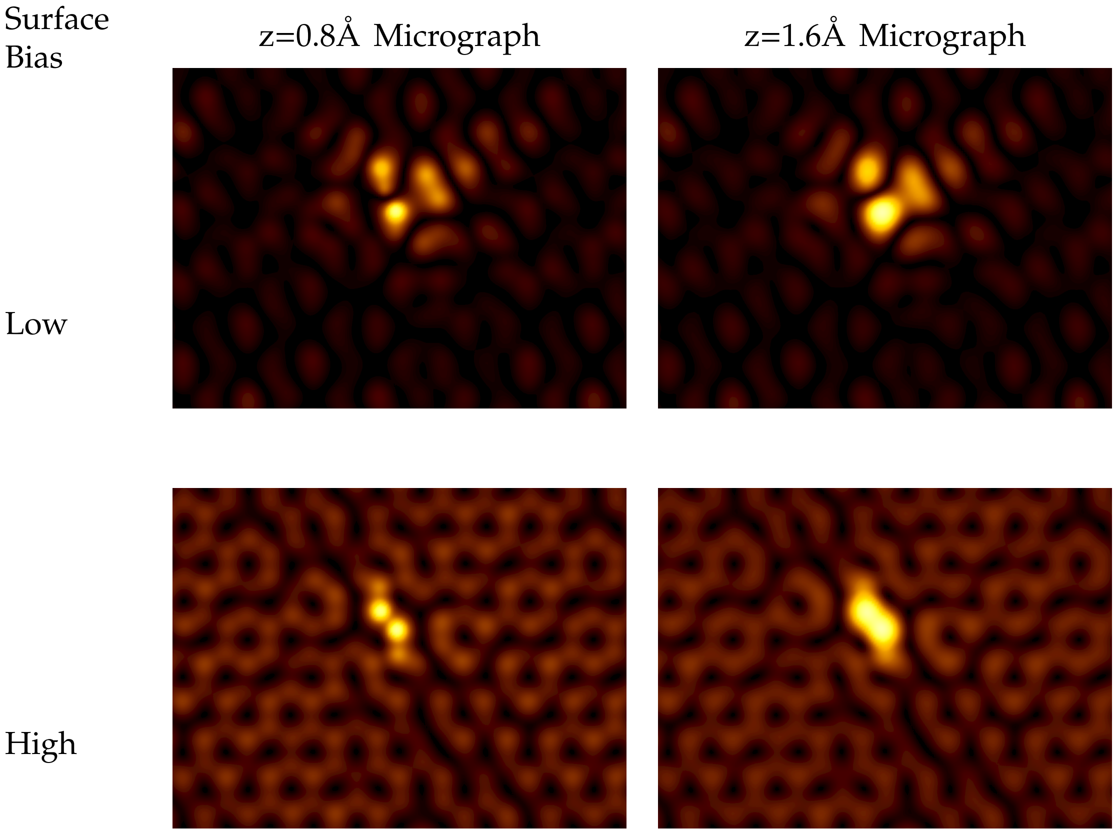

Figure C.4: The simulated scanning tunneling micrographs for the 3rd neighbour di-vacancy in bi-layer graphene.

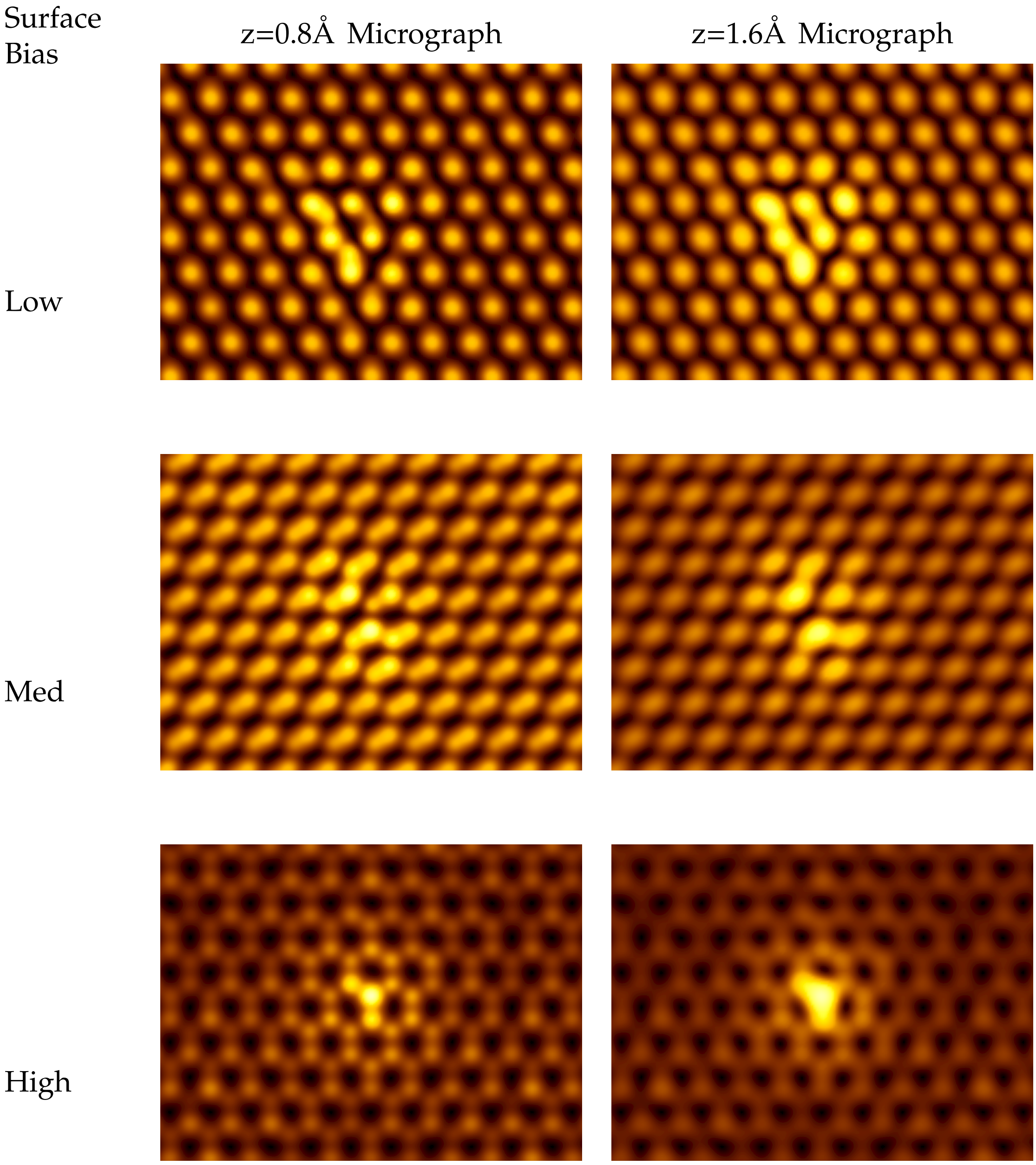

Figure C.5: The simulated scanning tunneling micrographs for the grafted interstitial in bi-layer graphene.

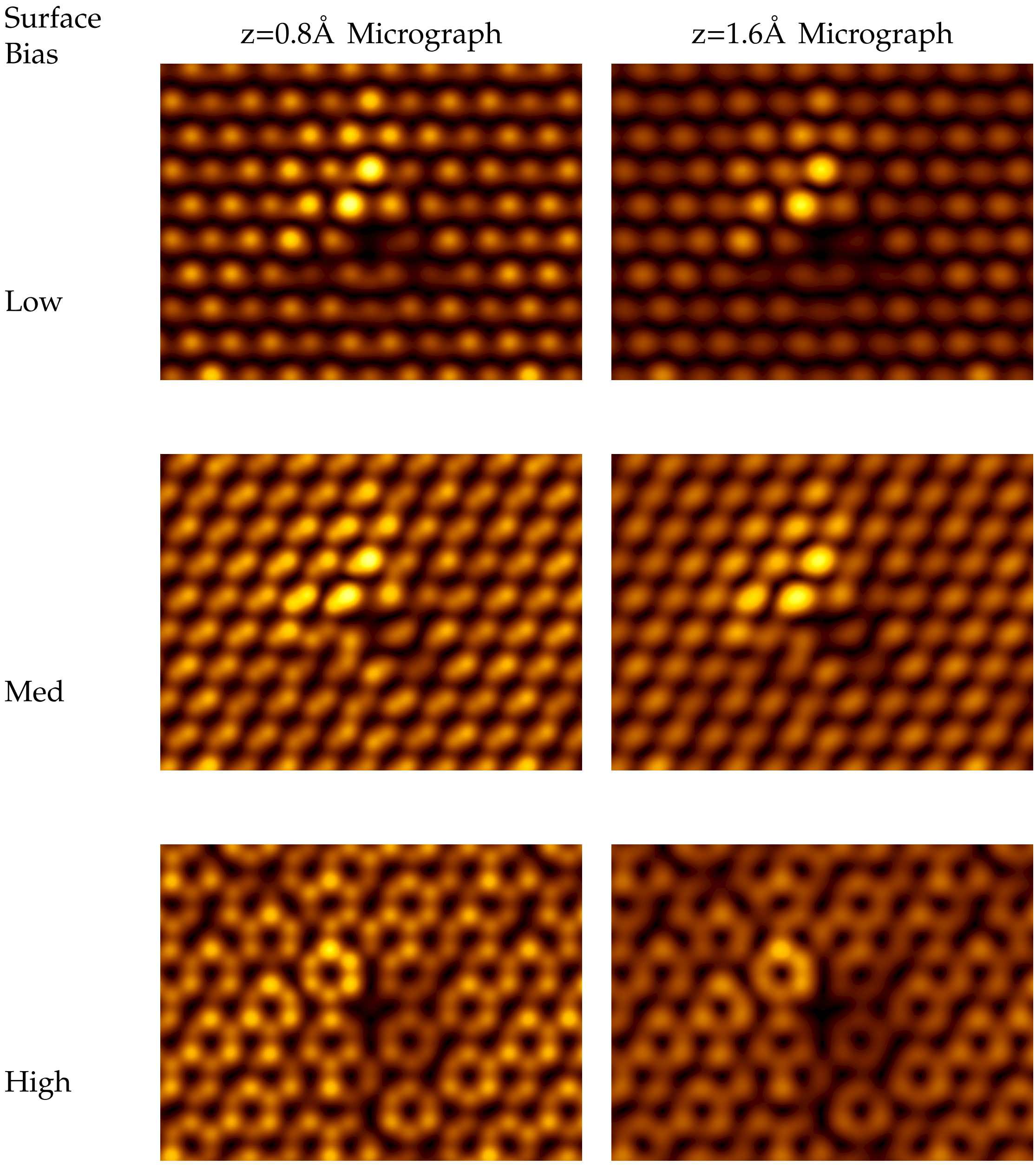

Figure C.6: The simulated scanning tunneling micrographs for the spiro-bonded interstitial in bi-layer graphene.

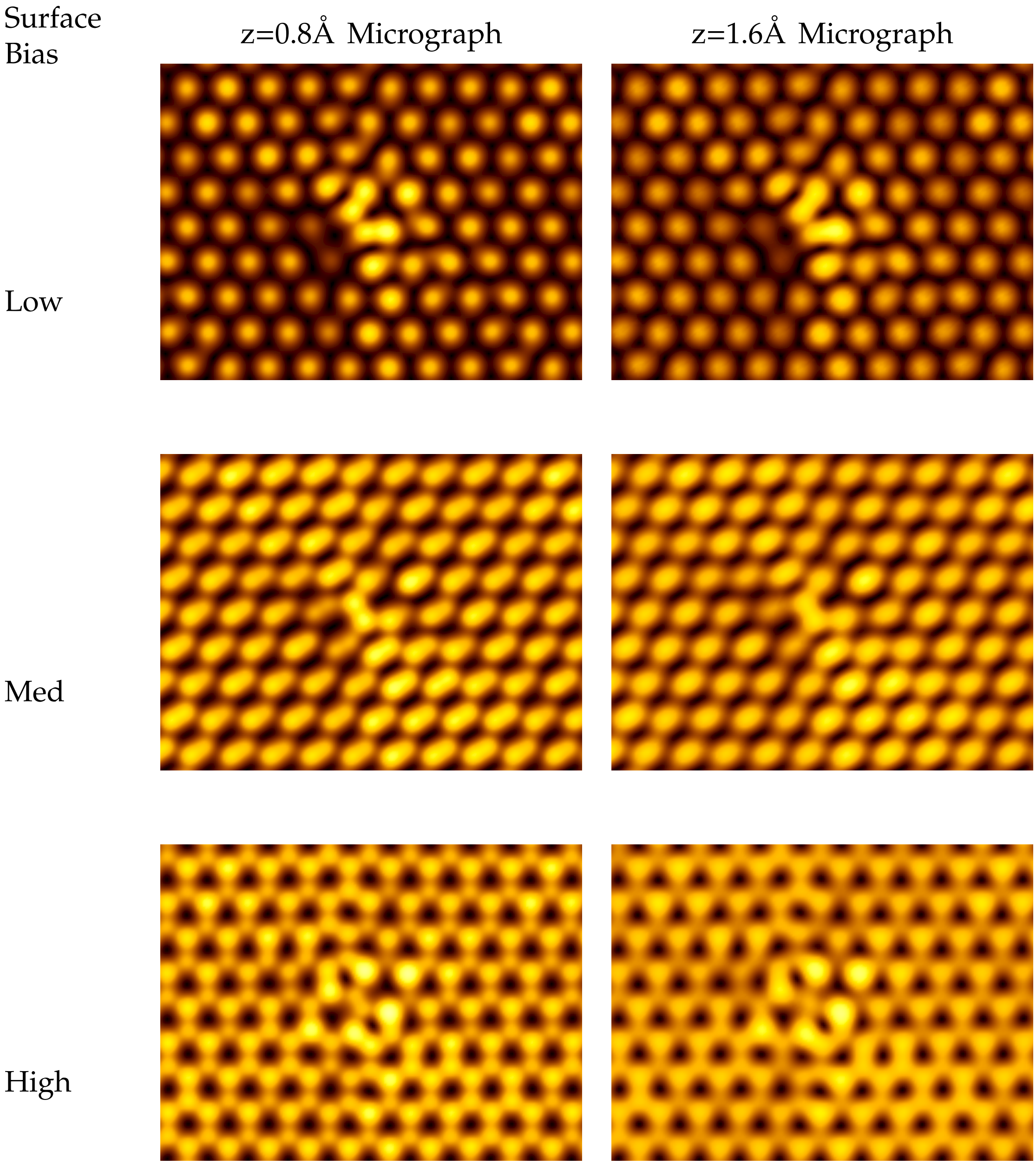

Figure C.7: The simulated scanning tunneling micrographs for the Stone-Wales defect in bi-layer graphene.

List of Figures

List of Tables